

LJUBOV JAANUSKA

Haar Wavelet Method  
for Vibration Analysis of Beams  
and Parameter Quantification





**LJUBOV JAANUSKA**

Haar Wavelet Method  
for Vibration Analysis of Beams  
and Parameter Quantification



Institute of Computer Science, Faculty of Science and Technology, University of Tartu, Estonia.

Dissertation has been accepted for the commencement of the degree of Doctor of Philosophy (PhD) in computer science on 5th of January, 2021 by the Council of the Institute of Computer Science, University of Tartu.

*Supervisor*

Assoc. Prof.     Helle Hein  
                          University of Tartu, Estonia

*Opponents*

Prof.                Eduard Petlenkov  
                          Tallinn University of Technology, Estonia

Assoc. Prof.     Jānis Šliseris  
                          Riga Technical University, Latvia

The public defense will take place on 19th of February, 2021 at 12:15 via Zoom.

The publication of this dissertation was financed by the Institute of Computer Science, University of Tartu.



Copyright © 2021 by Ljubov Jaanuska

ISSN 2613-5906

ISBN 978-9949-03-550-2 (print)

ISBN 978-9949-03-551-9 (PDF)

University of Tartu Press

<http://www.tyk.ee/>

# Abstract

A beam is a common structural element designed to resist loading. Applications of beams can be found in industrial, mechanical, aerospace and other engineering disciplines. Some examples are a doorway beam, a diving board, a snowboard, a rail and an aeroplane wing.

Underestimated loads during the design stage, looseness during the manufacturing stage, mechanical vibrations, corrosive environment, collisions may introduce some damage to beams. If no action is taken, the damage can turn into a fault or a breakdown of the whole system. Hereof, the entirety of beams is a crucial issue. Cracks, delaminations or changes of elastic parameters can be localised and assessed at a relatively early stage using non-destructive testing methods, such as the X-ray, the lamb waves, the acoustic emission. Inherently, these methods are expensive; they require arduous work to examine the entire structure and cannot always be applied to temperature-sensitive materials. Recently, modal-based methods have gained attention of many researchers. These methods are based on the idea that any damage alters physical properties of the structure (mass, stiffness) which in turn change the modal properties (natural frequencies, mode shapes, modal damping). Although several research papers have indicated that changes in the natural frequencies can follow damage severity, they are unable to provide spatial information. To overcome this limitation, advanced modern type signal processing techniques such as wavelets can be used.

This dissertation concerns non-inverse and inverse problems of beams with different boundary conditions. It is proposed to solve the forward problem of the vibration analysis using the Haar wavelets, their integration and the modal properties, such as natural frequencies and mode shapes. The numerical examples indicate that the proposed approach is fast and accurate.

The inverse problems deal with damage parameter quantification: damage with different severity in two sets of different locations can produce identical changes of the natural frequencies. In this dissertation, it is proposed to solve

the inverse problem of damage quantification with the aid of the Haar wavelets and machine learning. Two datasets and two machine learning methods are examined with the aim to highlight the most promising approach. The first dataset is based on the natural frequency parameters. For the second dataset, the mode shapes are transformed into the Haar wavelet transform coefficients. Back propagation neural networks and random forests are trained to predict the location and severity of the induced damage. The comparison of the approaches shows that the Haar wavelet transformation is more sensitive to the damage localisation, while the natural frequency parameters are more sensitive to the damage severity quantification. In most simulation cases of the damaged beams, the neural networks produce as precise predictions of the damage characteristics as the random forests; however, the random forests are easier to adjust and train.

The results presented in the dissertation can help understand behaviour of more complex structures under similar conditions, provide apparent influence on design concepts of structures, and enable new possibilities for operational and maintenance concepts.

# Contents

<b>List of Figures</b>	<b>10</b>
<b>List of Tables</b>	<b>14</b>
<b>Notation</b>	<b>17</b>
<b>Acronyms</b>	<b>19</b>
<b>1 Introduction</b>	<b>20</b>
1.1 Motivation and research background . . . . .	20
1.2 Research scope . . . . .	22
1.3 Objectives and research questions . . . . .	25
1.4 Contribution . . . . .	25
1.5 Significance of the research . . . . .	26
1.6 Thesis outline . . . . .	27
<b>PRELIMINARIES</b>	
<b>2 Methodology</b>	<b>28</b>
2.1 Related research on damage identification . . . . .	28
2.2 Wavelets . . . . .	31
2.2.1 Haar wavelets . . . . .	32
2.3 Machine learning . . . . .	35
2.3.1 Artificial neural networks . . . . .	36
2.3.2 Random forests . . . . .	39
2.4 Evaluation criteria . . . . .	42
2.5 Conclusion . . . . .	43
<b>3 Mathematical models</b>	<b>44</b>
3.1 Uniform beams . . . . .	44

3.1.1	Governing equations of Euler-Bernoulli beams . . . . .	44
3.1.2	Boundary conditions . . . . .	49
3.1.3	Euler-Bernoulli beam with a mass point . . . . .	51
3.1.4	Euler-Bernoulli beam with cracks . . . . .	52
3.1.5	Euler-Bernoulli beam with cracks and on elastic foundation	53
3.2	Non-uniform beams . . . . .	55
3.2.1	Non-uniform Euler-Bernoulli beam on elastic supports . .	55
3.2.2	Non-homogeneous Euler-Bernoulli beam with delaminations	56
3.2.3	Non-uniform axially functionally graded Euler-Bernoulli beam with elastic supports . . . . .	59
3.2.4	Conclusion . . . . .	60

## NON-INVERSE PROBLEMS

<b>4</b>	<b>Numerical solutions using Haar wavelets</b>	<b>61</b>
4.1	Literature review . . . . .	61
4.2	Haar wavelet integrals . . . . .	63
4.2.1	Haar wavelet method for solving free vibration problems	65
4.3	Numerical examples . . . . .	70
4.3.1	Uniform homogeneous beams . . . . .	70
4.3.2	Homogeneous beams with non-uniform cross-section . . .	70
4.3.3	Uniform axially functionally graded beams . . . . .	76
4.3.4	Non-uniform axially functionally graded beams . . . . .	77
4.4	Conclusions . . . . .	79

## INVERSE PROBLEMS

<b>5</b>	<b>Open cracks</b>	<b>81</b>
5.1	Related work . . . . .	81
5.2	Quantification of the crack . . . . .	87
5.2.1	Datasets . . . . .	87
5.2.2	Feed-forward neural networks with back propagation . . .	91
5.2.3	Random forest . . . . .	100
5.3	Quantification of two cracks . . . . .	103
5.4	Discussion and conclusions . . . . .	107
<b>6</b>	<b>Elastic supports</b>	<b>109</b>
6.1	Related work . . . . .	109
6.2	Quantification of the stiffness parameters . . . . .	111



6.2.1	Datasets . . . . .	111
6.2.2	Feed-forward neural networks with back propagation . . .	114
6.2.3	Random forest . . . . .	118
6.3	Discussion and conclusions . . . . .	119
<b>7</b>	<b>Point mass</b>	<b>123</b>
7.1	Related work . . . . .	123
7.2	Quantification of the point mass . . . . .	125
7.2.1	Datasets . . . . .	125
7.2.2	Feed-forward neural networks with back propagation . . .	128
7.2.3	Random forest . . . . .	131
7.2.4	Discussion and conclusions . . . . .	133
<b>8</b>	<b>Delamination</b>	<b>134</b>
8.1	Related work . . . . .	134
8.2	Quantification of the delamination . . . . .	137
8.2.1	Datasets . . . . .	137
8.2.2	Feed-forward neural network with back propagation . . .	139
8.2.3	Random forest . . . . .	143
8.3	Discussion and conclusions . . . . .	146
<b>9</b>	<b>Conclusion</b>	<b>147</b>
	<b>References</b>	<b>151</b>
	<b>Appendix A</b>	<b>179</b>
	<b>Appendix B</b>	<b>180</b>
	<b>Acknowledgements</b>	<b>181</b>
	<b>Kokkuvõte (Summary in Estonian)</b>	<b>182</b>
	<b>Curriculum vitae</b>	<b>184</b>
	<b>List of original publications</b>	<b>186</b>

# List of Figures

1.1	Some typical types of damage. From left to right, top to bottom: delamination with internal ply failures, external wrinkle, foreign object, internal and edge delaminations, internal wrinkle, distributed porosity, and debonding. . . . .	23
1.2	Hierarchy of damage identification process. . . . .	23
2.1	A classification of damage identification approaches. . . . .	29
2.2	The Haar wavelets: (a) the scaling function $h_1$ , (b) the mother wavelet $h_2$ , (c) the daughter wavelet $h_3$ ( $J = 1, m = 2, k = 0, \xi^{(1)} = 0, \xi^{(2)} = 1/4, \xi^{(3)} = 1/2$ ), (d) the daughter wavelet $h_4$ ( $J = 1, m = 2, k = 1, \xi^{(1)} = 1/2, \xi^{(2)} = 3/4, \xi^{(3)} = 1$ ). . . . .	34
3.1	An Euler-Bernoulli beam: (a) bending of the beam; (b) equilibrium for a small beam element (the bending moments $M(x, t)$ and the shear forces $V(x, t)$ are positive in the clockwise direction). . . . .	46
3.2	The first five mode shapes and natural frequencies. . . . .	49
3.3	An Euler-Bernoulli beam with a concentrated point mass. . . . .	52
3.4	A clamped beam on Pasternak foundation. . . . .	54
3.5	A linearly tapered beam with rotational and translational elastic constraints. . . . .	55
3.6	A beam with $n$ non-overlapping delaminations. . . . .	57
3.7	A beam section with a delamination. . . . .	58
4.1	The Haar wavelets: scaling function ( $i = 1$ ), the wavelets of resolution $J = 0, 1, 2$ (left), and the corresponding integrals of the wavelets (right). . . . .	64
4.2	A truncated beam with a parabolic-taper width. . . . .	74
4.3	A parabolic cantilever with parabolic thickness $h(\xi) = h_0(1 - \xi^2)$ and a circular cross-section. . . . .	75

4.4	Variation of the graded material properties. . . . .	76
4.5	Normalised first mode shapes of the AFG Euler-Bernoulli beam with varying flexural rigidity and mass density. . . . .	78
4.6	Normalised first mode shapes of the AFG Euler-Bernoulli beam with different elastic supports at the left end $k_{tl} = k_{rl}$ , at the right end $k_{tr} = k_{rr} = 1$ and flexural rigidity $D(\xi) = 0.2$ . . . . .	78
4.7	Normalised first mode shapes of the non-uniform AFG Euler-Bernoulli beam with elastic supports at the ends and a rigid intermediate support. . . . .	80
5.1	Nomographs for the first two natural frequencies ( $\omega_1$ and $\omega_2$ ) with different crack sizes ( $a/h$ ) and crack locations ( $x/L$ ). . . . .	85
5.2	Variation of the natural frequencies with different crack depths. . . . .	85
5.3	A block diagram of the experimental set-up to measure natural frequencies. . . . .	86
5.4	The first mode shape (left) and DFPs (right) in function of the crack location ( $L$ ) and the crack depth ( $D$ ). . . . .	88
5.5	Distribution of crack characteristics ( $L$ - location, $D$ - depth). . . . .	89
5.6	Correlation between crack characteristics and the DFPs or the HWTCs. . . . .	89
5.7	Distribution of the training patterns. . . . .	90
5.8	Feed-forward back propagation ANN. . . . .	91
5.9	Average MSE of quantification 50 cracks using varying number of hidden neurons and training patterns. . . . .	95
5.10	Characteristics of 50 test cracks: x - predicted depth and location; o - target values. . . . .	96
5.11	Correlation plot for the predicted characteristics of 50 cracks: (a), (b) predictions based on eight DFPs; (c), (d) predictions based on eight HWTCs. . . . .	97
5.12	Error distribution for the predicted characteristics of 50 cracks: (a), (b) predictions based on 8 DFPs; (c), (d) predictions based on 8 HWTCs. . . . .	98
5.13	The results of the complex approach: 50 ANNs trained on the DFPs to predict the depth of the cracks; 50 ANNs trained on the HWTCs to localise the cracks. . . . .	99
5.14	The results of the complex approach: 50 RF trained on the DFPs to predict the depth of the cracks; 50 RFs trained on the HWTCs to predict location of the crack. . . . .	102

5.15	A clamped-pinned beam with two cracks and on the Pasternak elastic foundation. . . . .	103
5.16	The dataset of two cracks in the beam. . . . .	103
5.17	Correlation and error distribution of the predicted cracks by the ensemble of the ANNs: (a)-(b) location from the left side of the beam; (c)-(d) distance between two cracks; (e)-(f) depth of the first crack; (g)-(h) depth of the second crack. . . . .	105
5.18	Correlation and error distribution of the predicted cracks by the ensemble of the RFs: (a)-(b) location from the left side of the beam; (c)-(d) distance between two cracks; (e)-(f) depth of the first crack; (g)-(h) depth of the second crack. . . . .	107
6.1	A uniform homogeneous Euler-Bernoulli beam with a clamped left end and an elastically supported right end. . . . .	111
6.2	The first DFP in function of the translational ( $k_t$ ) and rotational ( $k_r$ ) springs. . . . .	112
6.3	Distribution of stiffness characteristics. . . . .	112
6.4	Correlation between the stiffness parameters ( $k_t, k_r$ ) and the DFPs (left) or the HWTCs (right). . . . .	113
6.5	The results of the ANNs trained to predict stiffness parameters of the translational ( $k_t$ ) and rotational ( $k_r$ ) springs using the DFPs. . . . .	116
6.6	The results of the ANNs trained to predict stiffness parameters of the translational ( $k_t$ ) and rotational ( $k_r$ ) springs using the HWTCs. . . . .	117
6.7	The results of the RF trained to predict stiffness parameters of the translational ( $k_t$ ) and rotational ( $k_r$ ) springs using the DFPs. . . . .	120
6.8	The results of the RF trained to predict stiffness parameters of the translational ( $k_t$ ) and rotational ( $k_r$ ) springs using the HWTCs. . . . .	121
7.1	The dataset of the point masses. . . . .	126
7.2	The scaled first mode shapes (left) and the first DFPs (right) of the dataset. . . . .	126
7.3	Correlation between point mass parameters ( $L, M$ ) and the first eight DFPs (left) or 16 HWTCs (right). . . . .	127
7.4	Results of two ANNs trained to predict mass ratios and locations of the concentrated point masses using the DFP and the HWTCs. . . . .	130
7.5	The results of two ensembles of the RFs trained to predict mass ratios and locations using the DFP and the HWTCs. . . . .	132

8.1	Randomly generated delamination properties: $L_1$ - delamination location from the left side of the beam; $L_2$ - delamination length.	138
8.2	Correlation between the delamination status and the NFPs (left) or the HWTCs (right).	139
8.3	Correlation and error distribution of the predicted delamination statuses by the ANNs: (a)-(b) axial location; (c)-(d) delamination length; (e)-(f) ordinate location; (g)-(h) delamination ordinate location predicted with the additional input feature $L_2$ ; (i)-(j) delamination ordinate location predicted with the additional input feature $L_1$ .	142
8.4	Correlation and error distribution of the predicted delamination statuses by the RFs: (a)-(b) axial location; (c)-(d) delamination length; (e)-(f) ordinate location; (g)-(h) delamination ordinate location predicted with the additional input feature $L_2$ ; (i)-(j) delamination ordinate location predicted with the additional input feature $L_1$ .	145

# List of Tables

2.1	Training functions of the ANNs. . . . .	39
3.1	Beam properties. . . . .	46
3.2	Classical boundary conditions at the left and right ends of the beam. . . . .	50
3.3	Non-classical boundary conditions at the left end of the beam. . . . .	51
4.1	The first five $k_n$ for the uniform cantilever. . . . .	70
4.2	The first two $k_n^2$ for the wedge cantilever ( $\beta_b = 1, \beta_h = \beta$ ). . . . .	72
4.3	The first two $k_n^2$ for the cone cantilever ( $\beta_b = \beta_h = \beta$ ). . . . .	72
4.4	The first two $k_n$ for the cone ( $\beta_b = \beta_h = 1.4$ ) with equally varying translational spring constraints on the left and right ends ( $k_{tl} = k_{tr}$ ), whereas $k_{rl} = k_{rr} = 0$ ; $J = 5$ . . . . .	73
4.5	The third DFPs ( $k_3$ ) for the cone ( $\beta_b = \beta_h = 1.4$ ) with varying translational spring constraints on the left and right ends ( $k_{tl} = k_{tr}$ ), whereas $k_{rl} = k_{rr} = 0$ ; $J = 5, 6, 7$ . . . . .	73
4.6	The first three $k_n^2$ for the tapered cantilever with a parabolic-taper width, a linear-taper height and truncate factor $\eta$ . . . . .	74
4.7	The first two $k_n^2$ of the cantilever with a circular cross-section and parabolic thickness $h(\xi) = h_0(1 - \xi^2)$ versus the dimensionless coordinate of the fixed end. . . . .	75
4.8	The first $k_1^2$ of the axially functionally graded beam (aluminium-zirconia) versus the material gradient parameter $\beta$ ; $J = 5$ . . . . .	77
4.9	The first $k_1^2$ for the beams with varying left-side elastic constraints ( $k_{tl} = k_{rl}$ ); the supports at the right end are fixed ( $k_{tr} = k_{rr} = 1$ ); the beam properties are $\alpha = \beta$ ; $J = 6$ . . . . .	77
4.10	The first $k_1^2$ of the beam with varying flexural rigidity and location of the intermediate rigid support; the elastic end constraints are fixed to the values $k_{rr} = k_{tr} = k_{rl} = k_{tl} = 1$ ; $J = 6$ . . . . .	79

5.1	Correlation between the DFPs and the crack characteristics. . . .	90
5.2	Correlation between the HWTCs and the crack characteristics. . .	90
5.3	Average results of the predicted 50 cracks using different training functions, ANN configurations and DFPs. . . . .	93
5.4	Average results of the predicted 50 cracks using different training functions, ANN configurations and HWTCs. . . . .	93
5.5	The most accurate results of 50 crack quantifications using the RFs and DFPs ( $L$ - location, $D$ - depth of the crack). . . . .	100
5.6	The most accurate results of 50 crack quantifications using the RFs and the HWTCs ( $L$ - location, $D$ - depth of the crack). . . . .	101
6.1	Configurations of the datasets for stiffness parameter prediction. .	113
6.2	The lowest MSE of the five-fold cross-validation using a particular training function and dataset to predict the stiffness parameter of the translational spring $k_t$ . . . . .	114
6.3	The lowest MSE of the five-fold cross-validation using a particular training function and dataset to predict the stiffness parameter of the rotational spring $k_r$ . . . . .	114
6.4	The lowest MSE and the configuration of the corresponding RF provided with a particular dataset to predict the stiffness parameters of the translational and rotational springs. . . . .	118
7.1	Influence of each DFP on the point mass quantification ( $M$ - mass ratio, $L$ - location). . . . .	127
7.2	Influence of each HWTC on the point mass quantification ( $M$ - mass ratio, $L$ - location). . . . .	127
7.3	Configurations of the datasets for the point mass prediction. . . .	128
7.4	The lowest MSE of five-fold cross-validation using a particular training function, the number of hidden neurons and the dataset features to predict the mass ratio. . . . .	129
7.5	The lowest MSE of five-fold cross-validation using a particular training function, the number of hidden neurons and the dataset features to predict the location. . . . .	129
7.6	The lowest MSE of five-fold cross-validation to quantify point mass using the RFs and a particular dataset. . . . .	131
8.1	Primary frequencies of the composite cantilever. . . . .	138

8.2	MSE of five-fold cross-validation to predict the axial location ( $L_1$ ), the ordinate location ( $H_1$ ) and the extend of the delamination ( $L_2$ ) using various datasets by ANNs. . . . .	140
8.3	The lowest MSE of five-fold cross-validation to predict delamination status by RFs. . . . .	143
A1	First 25 patterns used for predicting the depth and location of the crack in the free vibrating Euler-Bernoulli cantilever ( $k_n$ is a frequency parameter). . . . .	179
B1	A summary table of parameter quantifications. . . . .	180



# Notation

$A$	cross-sectional area of the beam
$a$	depth of the crack
$b$	width of the beam
$C_i$	arbitrary constants of integration
$D$	bending stiffness ( $D = EI$ )
$E$	Young's modulus
$f_{cnf}$	circular frequency of vibration
$G$	shear modulus
$G_1$	Winkler foundation modulus
$G_2$	foundation modulus of rigidity in the Pasternak model
$h$	height of the beam
$I$	moment of inertia of a cross-sectional area of the beam or second moment of area about the neutral axis
$K_T$	stiffness coefficient of the translational spring
$K_R$	stiffness coefficient of the rotational spring
$k$	natural frequency parameter
$L$	length of the beam
$M$	concentrated mass
$m$	mass per unit length
$M(x, t)$	internal bending moment
$p$	number of features used at each node without replacement (ran- dom forest)
$p(x, t)$	load density (force per unit length of the beam)

$\rho$	mass density
$t$	time
$V(x, t)$	shear force acting on the cross-section
$W(x)$	mode shape
$x$	axial coordinate along neutral axis
$y(x, t)$	vertical displacement of beam
$\omega$	natural frequency of vibration

# Acronyms

<i>AFG</i>	axially functionally graded
<i>ANN</i>	artificial neural network
<i>BPANN</i>	back propagation artificial neural network
<i>BR</i>	Bayesian regularisation
<i>DFP</i>	dimensionless natural frequency parameter
<i>FEM</i>	finite element method
<i>FBPANN</i>	feed-forward back propagation artificial neural network
<i>HW</i>	Haar wavelet
<i>HWTC</i>	Haar wavelet transform coefficient
<i>HWTI</i>	Haar wavelet transform and integration
<i>LM</i>	Levenberg–Marquardt training function
<i>MSE</i>	mean square error
<i>NFP</i>	natural frequency parameter
<i>RF</i>	random forest

# Chapter 1

## Introduction

### 1.1 Motivation and research background

A beam is one of the oldest structural elements [Timo 83]. It is capable of withstanding loading actions, such as biaxial bending, transverse shears, axial stretching or compression and possibly torsion primarily by resisting bending [Das 11, Xuan 14, Niga 20]. The simplicity of the governing equations makes the static and dynamic behaviour of the beams easy to analyse and manipulate. The manufacturing process of beams is facilitated by their simple geometries. Therefore, beam type structures are widely used in steel construction and machinery industries [Orha 07]. Some examples of beams are turbine rotor blades, railway lines, flexible satellites, aeroplane wings, gun barrels, robot arms and long-span bridges.

The application of beams in contemporary manifold structures requires smart design and multi-purpose simulation tools. Such tools help improve structure properties and determine internal forces, stresses, deformations of structures under various loading effects.

In practical terms, beams may exhibit different types of damage, such as cracks, delaminations or changes of stiffness coefficients. The cause of damage is diverse: a design flaw, poor manufacture and severe environmental conditions. In order to identify and assess damage, engineers are in demand for handy tools. For instance, aircraft engineers need to assess turbine blades for the presence of cracks or delaminations; agricultural engineers need to consider vibrations and pressure in cutting tools; flat bridges have to be periodically checked for load-bearing capacities.

A literature study has shown that periodic visual inspections are often non-efficient, costly and require the components to be visually accessible [Ooij 14]. The inspections based on acoustics, magnetic field, eddy current, radiographs and thermal fields are time-consuming and complicated if a structural component is tightly fixed deep in the system or made of cold-work material.

A promising alternative to the existing damage identification methods can be found in the modal analysis. It is based on the principle that a reduction in the structural stiffness produces changes in the dynamic characteristics of the structure, such as natural frequencies, mode shapes, and damping ratios [Haki 14]. Constant monitoring for the changes in the dynamic response with a small number of sensors helps early indicate, localise and estimate damage severity [Hadj 05b, Rosa 09, Kona 11]. However, it is noted that the natural frequencies can only follow the damage severity, but damage locations do not influence the frequencies much; the modal assurance criterion is, in contrast, less sensitive to damage compared with the natural frequencies; the coordinate modal assurance criterion can localise damage in the beams but cannot follow severity [Ndam 02]. Therefore, it is recommended to incorporate the structural properties with modern statistical methods for accurate damage identification [Wang 18].

The statistical methods, such as correlation functions and coefficients, autoregressive models, machine learning methods properly address the modern-type vibration-based methods. The description of each method can be found in a great number of articles, for example, [Wu 09, Osta 13, Jaya 15, Uber 16]; therefore, the explanation of each method lies beyond the scope of the present thesis. At large, the statistical methods overcome the drawbacks of common non-destructive testing techniques and traditional methods by the ability to extract information from raw data. On the other hand, an optimal feature vector selection for the data-driven methods can be challenging. The vector is frequently dependent on the structure, the damage type, the goal of the investigation, advantages and disadvantages of the classifier. Yet, the choice of a proper statistical method for the damage quantification is complicated: no systematic comprehensive overview or comparison between the performances of different methods have been made thus far. The present thesis slightly fills the gap and compares the performance of two machine learning methods (the supervised neural networks and the random forests) on beams with various types of induced damage.

Merging data-driven machine learning with the modal analysis and signal processing, the present thesis proposes a new theoretical approach to the damage quantification problem. Namely, to overcome the limitations of the modal data and increase the accuracy of predictive models, a search for an informative fea-

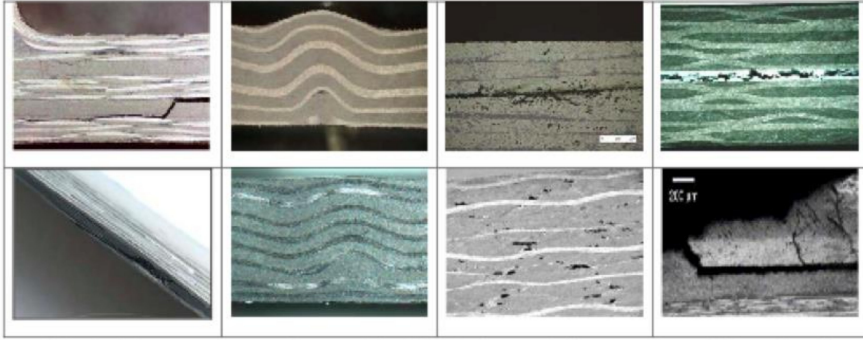
ture vector is conducted in the field of wavelets. The wavelet analysis represents a modern-type windowing technique for signal decomposition into logarithmically scaled regions [Misi 13]. A different view of data (signal) reveals aspects of data that other signal analysis techniques miss [Misi 96]. The application of the wavelets in engineering is on the rise and still requires additional research. Hereof, one of the main questions of the present thesis is whether the mode shape decomposition by the wavelets produces informative data and it may be successful applied to the machine learning techniques.

## 1.2 Research scope

The purpose of the present thesis is to describe a theoretical framework for the vibration analysis and damage parameter quantification with the aid of wavelets and machine learning with a general aim to contribute to the safety of beam type elements. Since the topic is broad, the main concepts and scope of the research have to be established.

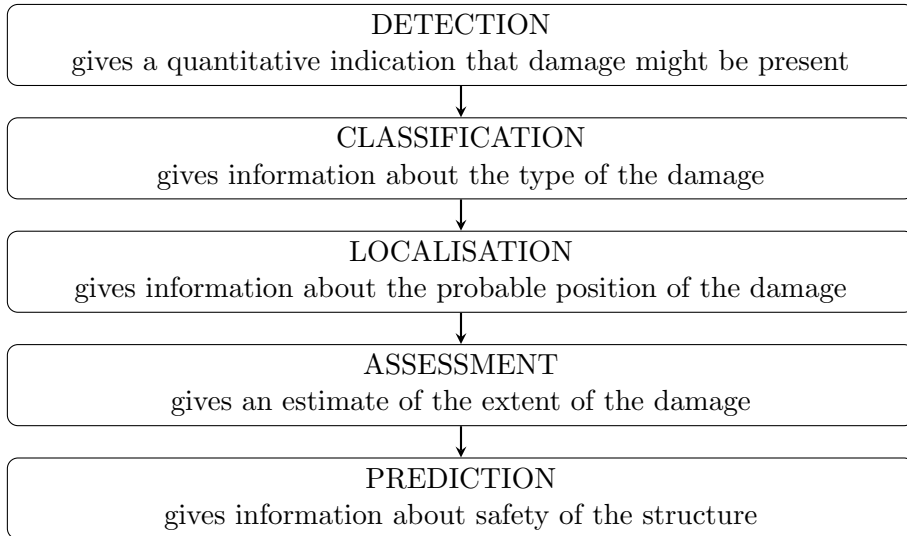
Damage in structural engineering is defined as a deviation in normal behaviour of the structure. The deviation is measured on the basis of two different states, one of which is assumed to represent the initial state of the structure. The fluctuation in structural behaviour is usually accounted by the changes in material or geometric properties. These changes alter stiffness, mass, energy dissipation properties and redistribute internal forces. A reduction in the structural stiffness produces changes in dynamic characteristics. If no action is taken, damage can lead to a fault - a situation when the structure does not operate. The present thesis addresses only damage and its parameter quantification; the study on faults is considered as a different discipline of research which is beyond the scope of this thesis.

The most typical types of damage that may appear in structural elements are cracks, delaminations, wrinkles, foreign objects, dents, scratches, buckles, gouges, nicks, erosion, debonding [Brah 15, Guem 20] (Figure 1.1 [Guem 20]). The present thesis investigates the most common or dangerous ones: cracks, delaminations and concentrated point masses (research on buckling is not included into the thesis; however, some results can be found in [Hein 12a]). Most boundary conditions and beam properties in the simulation cases presented in the thesis are chosen according to the ones given in the literature to compare the results obtained by alternative numerical methods.



**Figure 1.1:** Some typical types of damage. From left to right, top to bottom: delamination with internal ply failures, external wrinkle, foreign object, internal and edge delaminations, internal wrinkle, distributed porosity, and debonding.

Ideally, small damage can be automatically detected, described and classified at an early stage of its development with a major aim to predict the life cycle of the whole constructions. The corresponding protocol of the damage identification process is shown in Figure 1.2 [Fan 11]. Considerably, no single existing approach can solve all the damage identification problems straightforwardly in virtue of various damage types, an abundance of physical models and complexity of mathematical models [Marw 00, Fan 11]. Therefore, each milestone of the damage identification process is investigated separately.



**Figure 1.2:** Hierarchy of damage identification process.

The present thesis focuses on Levels 1, 3 and 4. Formerly, Level 1 of damage detection is treated as a non-inverse problem. The wavelet integration is a novel approach adopted towards the calculation of natural frequencies. In case of discrepancy in the calculated and measured values, the presence of damage can be detected. Here, it has to be noted that the present thesis does not discuss the problems arising from measuring and cleansing the modal data (for example, filtering noise, spike removal, removal of outliers, treatment of missing data).

Level 3 and 4 in Figure 1.2 are considered the most difficult tasks in the vibration-based damage identification process since they do not have an explicit analytical solution [Wang 18]. Highly non-linear relationship between the vibration responses and the damage parameters requires adoption of soft optimisation algorithms, such as genetic algorithm, simulation annealing, support vector machine [Fan 11]. In the present thesis, the inverse problems are tackled with supervised machine learning (the artificial neural networks and the random forests) since it is a frequently used and accurate tool for finding relationships between non-linear data [Aydi 14]. The research on the support vector machines [Hein 11c] for damage quantification has not shown promising results, and it is not included into the thesis.

Apparently, supervised machine learning requires some amount of training, validation and testing data. The two possible sources of the vibration-based data are the model-based methods and response-based methods. The model-based methods assume the availability of a detailed numerical model of the damaged structure; while the response-based methods depend only on experimental response data from the structure [Fan 11]. To accumulate enough data for machine learning via an experiment means to make copies of the system of interest and damage it in all the ways that might occur naturally. This is out of the scope of the present thesis. The data for machine learning are obtained using the model-based methods; the dynamic response measurement, environmental effects and excitation/sensing problems are not taken into account in the present thesis.

The model-based methods require a proper mathematical model. In mechanics, several theories are associated with beam deformation/displacement and stresses. Some of them are the Euler-Bernoulli beam theory, the Timoshenko beam theory and the two-dimensional elastic theory. In the present thesis, the Euler-Bernoulli beam theory underlies the research since it is the simplest model widely applicable to long slender beams. Following the Euler-Bernoulli beam theory, the modal properties (the natural frequencies and modal shapes) are drawn. Pilot research on the other types of beams, such as the Timoshenko beams and nano-beams, can be found in [Hein 12a, Hein 12b, Fekl 15, Hein 19b].



Once the modal data are obtained numerically, the mode shapes are decomposed into the Haar wavelet transform coefficients to form a feature vector for machine learning. The artificial neural networks and the random forest are trained on these data. In line, the machine learning methods are trained on the natural frequency parameters. The performances of the methods are compared to each other with the aim to highlight the most promising technique and features. No relevant framework for the damage quantification (modal properties coupled with the Haar wavelets and machine learning) has been found in the literature.

### 1.3 Objectives and research questions

Broadly, the dissertation aims at the development of a theoretical framework for vibration analysis and modal-based damage quantification in beams with the aid of the Haar wavelets and supervised machine learning with a general goal to contribute to the safety of beam type elements. In detail, the present thesis addresses the following research questions.

- Can the free vibration of beams be systematically studied with the aid of the Haar wavelet integration?
- Which method produces more accurate predictions of the damage parameters: the feed-forward back propagation neural networks or the random forests?
- Which features produce more accurate results on the damage parameter quantification using the supervised machine learning methods: the natural frequency parameter based features or the mode shape decomposition into the Haar wavelet transform coefficients?

To answer these questions, multiple simulation studies are conducted (see Chapter 4-8).

### 1.4 Contribution

The author's main contribution consists of:

- providing an overview on solving the differential equation of the free vibration of beams with the aid of the Haar wavelets;

- calculating the dimensionless natural frequency parameters of uniform or non-uniform homogeneous or non-homogeneous intact Euler-Bernoulli beams with classical or elastic boundary conditions with the aid of the Haar wavelets and their integration;
- calculating multiple datasets (the natural frequency parameter based and the Haar wavelet transform coefficient based), which describe different types of damage;
- adapting the feed-forward neural networks with back propagation training algorithms for damage parameter quantification in Euler-Bernoulli beams or supports;
- adapting the random forests for damage parameter quantification in Euler-Bernoulli beams or supports;
- comparing the results of the machine learning methods proceeding from the nature of the feature vector.

At large, the main contribution of the thesis lies in the development of the guidelines for the characterisation of vibrating beams and different types of damage in them. The framework is based on the changes in the dynamic behaviour of beams coupled with the Haar wavelets and the machine learning methods. The conducted research can serve as a reference in future numerical studies on (non-)inverse problems. Also, the highlighted approaches can be used in the design of beam-like structures and contribute to the development of a tool for structural health monitoring.

## 1.5 Significance of the research

Structure failure and costly repairs due to different damage causes can be prevented if appropriate retrofitting is carried in time [Wang 18]. Although many parameter identification methods have been described in the literature, there are still numerous difficulties in their practical application (see Section 2.1). Nevertheless, engineers are in a constant need for a simple, effective and reliable non-destructive procedure that allows to diagnose and quantify damage in various structures. Hereof, the present thesis contributes to developing a technique for modal-based damage identification. Multiple simulation cases conducted in the thesis demonstrate that the proposed methods of the Haar wavelets and machine learning are capable of dealing with a range of structural damage scenarios even when the damage is very small or large.

## 1.6 Thesis outline

The present thesis explains the transverse vibration of uniform and non-uniform homogeneous and non-homogeneous intact and damaged Euler-Bernoulli beams on classical and elastic supports and demonstrates the integration of the Haar wavelets and the machine learning methods for solving non-inverse and inverse problems in dynamic systems. Nine chapters of the thesis are grouped into four parts.

Chapter 2 and 3 provide an overview of the methodology and mathematical models used in the thesis. These chapters explain fundamental concepts of the Euler-Bernoulli beam theory, lateral vibration, damage quantification, wavelets and machine learning. The chapters are supposed to help the reader go through the rest of the thesis.

Chapter 4 describes the Haar wavelet integration for solving non-inverse problems of intact beam vibrations. The procedure is illustrated through multiple simulation studies conducted on various mathematical models of the beams.

Chapter 5, 6, 7 and 8 belong to the third part of the thesis. Based on the analytical computational simulations of beam-like structures, a comprehensive study on several damage quantification algorithms is provided to illustrate the validity and effectiveness of the Haar wavelets and supervised machine learning in different scenarios (quantification of cracks, delaminations, point masses and changes of the stiffness coefficients in elastic supports).

Concluding remarks and directions for future research are given in Chapter 9.

# Chapter 2

## Methodology

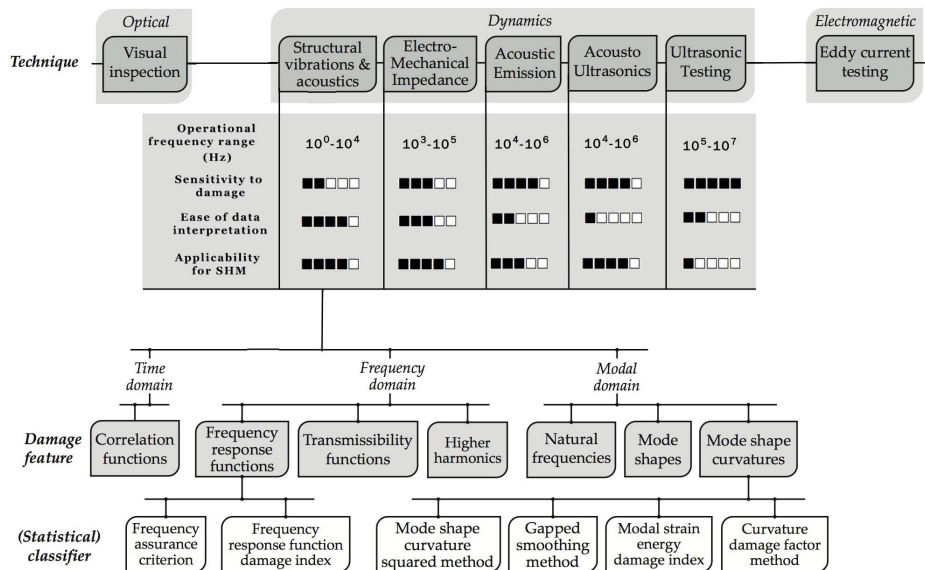
This chapter highlights conceptual approaches used in the vibration analysis and damage parameter identification. Particular emphasis is placed on the Haar wavelets and machine learning in a volume required for solving (non-)inverse problems described in the thesis.

### 2.1 Related research on damage identification

To ensure the reliability of structures and prevent damage transition into a fault, a broad range of damage identification techniques have been developed. A classification of the most commonly used methods is shown in Figure 2.1 [Ooij 14].

Visual approaches focus on the inspection of accessible surfaces. The approaches are often highly subjective; the reports and analysis lack an adequate evidential basis for making decisions [Haki 15]. Digital image processing facilitates a standard visual inspection for damage detection but does not reveal inner damage [Ruck 06b]. Therefore, visual approaches are often used for rough estimations and critical damage detections.

The electromagnetic approaches are based on the response of electric currents, magnetic fields, or both. In civil structures, damage is most often assessed by X-ray. This implies that the damaged region is easily accessible. A novel active infrared thermography method is based on the eddy current pulsed thermography and potentially effective to detect multiple hidden cracks on corroded metal surfaces [Xu 16]. However, the application of the method is limited by the shape of the structure and material sustainability to heating [Guem 20].



**Figure 2.1:** A classification of damage identification approaches.

The present thesis addresses changes in the dynamic responses as an alternative and promising approach for damage identification. The structural vibrations and electro-mechanical impedance techniques operate at a relatively low-frequency range ( $10^0 - 10^4$  and  $10^3 - 10^5$  Hz, respectively). The methods can be applied to complex and large structures; the results of measurements are relatively easy to interpret [Ooij 14]; however, to increase the sensitivity and accuracy of the methods, additional manipulations on the modal data have to be performed. The high frequency methods ( $10^4 - 10^7$  Hz) use acoustic emission, acousto-ultrasonics and ultrasonic testing techniques. These methods are more sensitive to damage detection than low frequency methods. However, the most significant disadvantages of the high-frequency techniques are localised time-consuming scanning process and problematic interpretation of wave forms, particularly in the case of non-flat or composite structures. A comprehensive review of the structural vibration-based damage detection methods can be found in multiple papers, for example, [Doeb 98, Zou 00, Samu 05, Word 08, Word 09, Fan 11, Hoss 17, Chen 18, Gome 19]. This thesis uses the vibration-based structural damage detection methods as a starting point for further soft optimisation procedures.

In case of vibration-based damage identification, a structure is equipped with an array of actuators and sensors which excite and record the dynamic response [Aydi 14]. The measured response signal is then processed in the time, frequency

or modal domains and compared to the model values. Notably, the modal domain methods have attracted the attention of researchers. Such methods are cost-effective and are relatively easy to operate [Zou 00]. They can provide global and local damage information since insignificant changes in the physical properties of a structure (natural frequencies, mode shapes and modal damping) result in detectable variations in modal parameters [Wei 04].

The modal-based methods that use the natural frequency change as a primary feature for damage detection is attractive to many researchers. This is due to the fact that the natural frequencies can be measured from a few accessible points on the structure and are generally less contaminated by experimental noise [Fan 11, Aydi 14]. However, the frequency-based methods have several limitations. According to Fan and Qiao [Fan 11], the damage identification methods based on frequency change can be successfully applied to simple structures (typically, a slender beam-type structure with an artificially induced crack) in a controlled laboratory condition such as for quality control in manufacturing. The application of the methods to real structures is limited by complex mathematical models; the frequency-based methods do not account for small or multiple damages since the frequency change is insignificant and may be buried in the changes caused by environmental or operational conditions. Furthermore, the changes in the lower modal frequencies are unable to provide spatial information about damage [Farr 01, Karb 09]. An exception to this limitation occurs if a sufficient number of frequencies with significant enough changes are used to determine the location of the damage [Doeb 98]. Wang [Wang 18] proposes to solve the damage localisation problem by incorporating the frequencies with other structural properties and/or data correlation techniques.

A second group of the modal-based damage identification methods uses the mode shapes - a dynamic property of the structure which represents the pattern (mode) of an object at a particular natural frequency. According to Yan et al. [Yan 07] and Kim et al. [Kim 03], the mode shapes contain local information that enables to identify damage location even in case of multiple damages. Hu et al. [Hu 06] and Liu et al. [Liu 05] state that the first five mode shapes are the most sensitive and informative for damage identification. Furthermore, compared to the natural frequencies, the mode shapes are less affected by environmental changes such as temperature. Nevertheless, a few problems also exist with the mode shape based damage identification methods. Firstly, a series of sensors are required to measure the mode shapes. Secondly, the measured mode shapes are more affected by noise than the natural frequencies. Thirdly, the mode shapes are only sensitive to damage in the particular area of a structures (for instance, in the mid-span of a

clamped-clamped beam), and without further signal processing or pattern recognition techniques they can only be adopted for preliminary damage localisation rather than accurate localisation or quantification of damage [Wang 18]. As an effort to enhance the sensitivity of vibration-based damage detection, methods that use both natural frequencies and mode shapes are proposed in [Aydi 14, Tan 17] as promising techniques for damage identification.

The third group of the modal-based methods relies on the mode shape derivatives, such as mode shape curvatures, modal strain energy and modal flexibility. It is noted that for beams, plates, and shells there is a direct relationship between curvature and bending strain [Raza 06]. Some researchers discuss practical issues of measuring strain directly or computing it from the displacements or accelerations [Doeb 98]. Chance et al. [Chan 94] points out that numerical calculation of the curvatures from the mode shapes results in unacceptable errors. Pandey et al. [Pand 91] state that the absolute changes in the mode shape curvature are a good indicator of damage for the beam structures modelled using the finite element method (FEM). Nevertheless, the difference in the modal curvature for higher modes shows several peaks at the damage location and also at other positions, which may lead to a false indication of damage [Waha 99]. To reduce the possibility of a false alarm, it is suggested to use only the first few low curvature mode shapes for damage identification.

This thesis proposes to address the damage quantification problem using the natural frequencies and mode shapes. The limitations of the modal data are overcome by wavelets and machine learning.

## 2.2 Wavelets

In 2000, Quek et al. [Quek 01] conducted a sensitivity analysis of crack detection in simply supported and clamped beams under a static load. The authors found that the wavelets were sensitive to the curvature of the deflection profile calculated with the aid of the FEM. Using the vibration data and the Haar/Gabor wavelets, multiple cracks were detected. Notably, the Haar wavelets exhibited superior performance for detecting discrete cracks whose length ratio to the depth of the beam was as low as 1/150. The observation of the wavelet sensitivity to the non-linear structure changes was confirmed experimentally by Rucka and Wilde in [Ruck 06a, Ruck 06b]. Inspired by these articles, the wavelets were applied to the vibration and damage parameter quantification in this thesis.

A wavelet is a mathematical function that can be presented as a wave-like oscillation with an amplitude that begins at zero, increases, and then decreases back to zero [Farr 17]. Such a function is used to decompose a given function or continuous-time signal into different scale components. Each scale component can be assigned a frequency range and then be studied with a resolution that matches its scale. The most popular wavelet families are Daubechies, Coiflet, Symlet; however, these wavelets do not have an analytical expression. The Haar wavelets are mathematically the simplest wavelets which have an analytical expression [Lepi 14].

A wavelet transform is the representation of a function by wavelets. The transform can be classified into discrete (DWT) and continuous wavelet transform (CWT). Both can be used to represent continuous-time (analogue) signals. CWTs operate over every possible scale and translation whereas DWTs use a subset of scale and translation values or a representation grid [Farr 17].

The wavelet transform has advantages over the traditional Fourier transform in terms of representing functions that have discontinuities and sharp peaks as well as accurately deconstructing and reconstructing finite, non-periodic and/or non-stationary signals [Farr 17]. Furthermore, the wavelet-based methods do not require the analysis of complete structure. Due to the time-frequency localisation, the wavelet transform can reveal some hidden parts of data that other signal analysis techniques fail to detect [Yan 07].

The wavelet transform has been applied in many fields, including vibration-based damage detection ([Liew 98, Wang 99a, Quek 01, Hong 02, Gent 03, Yam 03, Douk 03, Yan 04, Han 05a, Ruck 06a, Zhu 06, Umes 09, Zhen 09, Srin 10, Cao 11]). In this thesis, the Haar wavelets and their integration are used to calculate the natural frequencies of various (non-)uniform and (non-)homogeneous beams or decompose mode shapes into a set of the Haar wavelet transform coefficients to form a feature vector for machine learning methods. The idea originates from Hein [Hein 07] who has successfully combined the Haar wavelets and the neural networks for solving the inverse problem of elastic foundation parameter identification in vibrating delaminated beams.

### 2.2.1 Haar wavelets

The present thesis focuses on the discontinuous Haar wavelet functions, which are mathematically the simplest wavelets [Lepi 14]. Chen and Hsiao [Chen 97, Hsia 99] demonstrated that these wavelets could successfully approximate the



derivatives of functions for solving differential equations. This approach was developed further by Lepik [Lepi 05].

The Haar wavelet is the first known and yet the simplest wavelet introduced in 1909 by Alfred Haar. This wavelet is also known as the length-2 Daubechies filter [Aziz 13]. The main properties of the Haar wavelet are orthogonality and compact support. The scaling function for the family of the Haar wavelets is symmetric and discontinuous (Figure 2.2a). It resembles a step function which is defined as [Aziz 13]:

$$h_1(\xi) = \begin{cases} 1, & \text{for } \xi \in [0, 1), \\ 0, & \text{elsewhere.} \end{cases} \quad (2.1)$$

The mother wavelet for the Haar wavelet family is anti-symmetric (Figure 2.2b), and it is defined as:

$$h_2(\xi) = \begin{cases} 1, & \text{for } \xi \in [0, \frac{1}{2}), \\ -1, & \text{for } \xi \in [\frac{1}{2}, 1), \\ 0, & \text{elsewhere.} \end{cases} \quad (2.2)$$

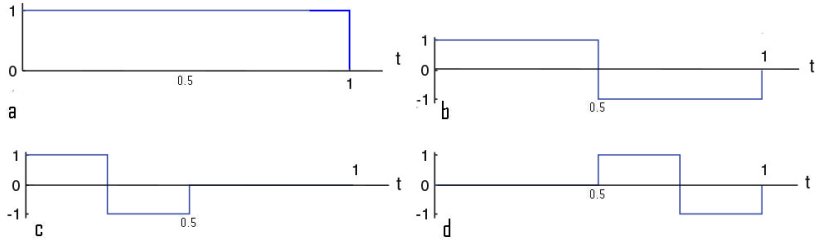
All the other functions in the Haar wavelet family are defined on the subintervals of  $[0, 1]$ . The daughter functions are generated from the mother wavelet  $h_2(\xi)$  by scaling and shifting it along the abscissa [Lepi 14]:

$$h_i(\xi) = \begin{cases} 1, & \text{for } \xi \in [\xi^{(1)}, \xi^{(2)}), \\ -1, & \text{for } \xi \in [\xi^{(2)}, \xi^{(3)}), \\ 0, & \text{elsewhere,} \end{cases} \quad (2.3)$$

where

$$\xi^{(1)} = \frac{k}{m}, \xi^{(2)} = \frac{k+0.5}{m}, \xi^{(3)} = \frac{k+1}{m}. \quad (2.4)$$

Integer  $k$  is the translational parameter or the shifting factor ( $k = 0, 1, \dots, m-1$ ),  $m$  is the dilatation parameter or the factor of scale ( $m = 2^j$  and  $j = 0, 1, \dots, J$ ),  $j$  indicates the level of the wavelet. Integer  $J$  is the maximal level of resolution and  $M$  is the resolution coefficient ( $M = 2^J$ ). The relation between  $i$ ,  $m$  and  $k$  is expressed as  $i = m + k + 1$ . Two of the daughter wavelets  $h_3$  and  $h_4$  are shown in Figure 2.2 c and d.



**Figure 2.2:** The Haar wavelets: (a) the scaling function  $h_1$ , (b) the mother wavelet  $h_2$ , (c) the daughter wavelet  $h_3$  ( $J = 1$ ,  $m = 2$ ,  $k = 0$ ,  $\xi^{(1)} = 0$ ,  $\xi^{(2)} = 1/4$ ,  $\xi^{(3)} = 1/2$ ), (d) the daughter wavelet  $h_4$  ( $J = 1$ ,  $m = 2$ ,  $k = 1$ ,  $\xi^{(1)} = 1/2$ ,  $\xi^{(2)} = 3/4$ ,  $\xi^{(3)} = 1$ ).

The Haar wavelets can also be used to present any function in the discrete form. Several techniques are described in [Addi 02, Lepi 14]. In this thesis, the collocation points method [Lepi 14] is used since it is applicable for the mode shape representation in the form of a limited feature matrix vector. The values of the collocation points are defined by [Lepi 14]:

$$\xi_l = \frac{l - 0.5}{2^{J+1}} = \frac{l - 0.5}{2M}, \quad (2.5)$$

where  $l = 1, 2, \dots, 2M$ . The collocation points divide the interval  $\xi \in [0, 1)$  into  $2M$  parts; each part is of length  $\Delta\xi = 1/(2M)$ .

The wavelet function values of (2.3) in the collocation points are presented in the Haar matrix  $H$ , whose dimensions are  $2M \times 2M$ . The elements of the matrix are  $H_{2M \times 2M}(i, l) = h_i(\xi_l)$ . An example of the Haar matrix for  $M = 2$  is presented below:

$$H_{4 \times 4} = \begin{matrix} & \frac{1}{8} & \frac{3}{8} & \frac{5}{8} & \frac{7}{8} \\ \begin{matrix} h_1 \\ h_2 \\ h_3 \\ h_4 \end{matrix} & \begin{pmatrix} 1 & 1 & 1 & 1 \\ 1 & 1 & -1 & -1 \\ 1 & -1 & 0 & 0 \\ 0 & 0 & 1 & -1 \end{pmatrix} \end{matrix}. \quad (2.6)$$

Any function  $y(\xi)$ , which is integrable in the interval  $[0, 1)$ , can be expanded into the Haar series [Lepi 14]:

$$y(\xi) = \sum_{i=1}^{\infty} c_i h_i(\xi), \quad (2.7)$$

where  $c_i$  are the wavelet coefficients, which can be calculated by minimizing the integral square error (see [Hsia 99]). In the present thesis, the sum is limited with  $2M$  terms. The discrete form of (2.7) with  $2M$  is

$$y(\xi_l) = \sum_{i=1}^{2M} c_i h_i(\xi_l), \quad (2.8)$$

where  $\xi_l$  ( $l = 1, 2, \dots, 2M$ ) are the collocation points. The matrix form of (2.8) is

$$y = cH, \quad (2.9)$$

where  $H$  is the Haar matrix,  $c = (c_i)$  and  $y = (y_l)$  are  $2M$  dimensional row vectors. The Haar wavelet coefficients can be found by:

$$c = yH^{-1}, \quad (2.10)$$

where  $H^{-1}$  is the inverse of the Haar matrix. Replacing  $c$  into (2.7) with  $i = 1, \dots, 2M$ , the wavelet approximation of function  $y$  with the level of resolution  $J$  can be obtained. The accuracy of the approximation is discussed in several articles ([Lepi 14, Maja 15, Maja 18]). Equation (2.10) is called the forward discrete transform, and (2.9) is called the inversed discrete transform. Since  $H_{2M \times 2M}$  and  $H_{2M \times 2M}^{-1}$  contain many zeros, the Haar transform is much faster than the Fourier transform [Hsia 99].

## 2.3 Machine learning

Damage quantification on the basis of the modal data is an inverse problem. That means, damage of different severity in two different locations can produce identical changes in the modal parameters. Since the problem cannot be solved directly, function fitting methods are needed. The present thesis addresses the damage quantification problem via machine learning.

The Statistical Analysis System Institute defines machine learning as follows: “it is a method of data analysis that automates analytical model building. Using algorithms that iteratively learn from data, machine learning allows computers to find hidden insights without being explicitly programmed where to look” [SAS]. Such properties fit particularly well to the present thesis on the parameter quantification in dynamic systems. In the context of damage identification, machine learning means that a model can learn to detect and assign a damage status to a given feature vector from the structure. In the present thesis, the feature vector is

formed using the natural frequency parameters and/or the Haar wavelet transform coefficient derived from the mode shapes with a general aim to highlight sensitive features for damage assessment and localisation.

Once features are determined, the map between the features and the damage parameters can be constructed. Many algorithms are available for this purpose. Two the most popular types of machine learning algorithms are [Word 11]:

- unsupervised learning algorithms: the algorithms are not provided with the correct values during the training process; opposite, these algorithms look for the features in the data themselves. According to Worden [Word 09], this mode of learning only applies to damage detection (Figure 1.2).
- supervised learning algorithms: in these algorithms, the target values are known and are given to the algorithm; during training, the machine learning system tunes itself so that the calculated outputs closely match to the target values; once the system is tuned, it is able to predict outputs to the unknown data.

In the present thesis, the supervised learning algorithms are used since both, the inputs and outputs, are available - the datasets are calculated numerically using the models described in Chapter 3. Furthermore, the supervised learning algorithms perform well on the following types of tasks:

- regression: assigning real floating-point value to the feature vector;
- classification: assigning labels to the feature vector.

Prediction of damage parameters (location and severity) is a regression task. In the present thesis, the damage status is predicted using a supervised function approximation in terms of the artificial neural networks and the random forests. The techniques are described in the next subsections.

### **2.3.1 Artificial neural networks**

The artificial neural network (ANN) is defined by the inventor of a neurocomputer Hecht-Nielsen as “a computing system made up of a number of simple, highly interconnected processing elements, which process information by their dynamic state response to external inputs” [Caud 88]. Specifically, a basic component of any ANN is an artificial neuron (node or processing unit). A neuron receives

signals from other neurons:

$$X = \begin{pmatrix} x_1 \\ \dots \\ x_n \end{pmatrix}. \quad (2.11)$$

On the way to the neuron, the signal passes through synapses. A synapse denotes the strength of the connection between two nodes. Mathematically, it is represented as a floating-point value, which is positive or negative. The synaptic weights of a neuron can be presented as a vector:

$$W = \begin{pmatrix} w_1 & \dots & w_n \end{pmatrix}. \quad (2.12)$$

The “learning” part of an ANN means continuous adjustment of these weight values.

In the present thesis, a sum net function is used to sum all the input signals weighted by the corresponding synaptic weights and the bias  $b$ :

$$NET = WX + b = \begin{pmatrix} w_1 & \dots & w_n \end{pmatrix} \begin{pmatrix} x_1 \\ \dots \\ x_n \end{pmatrix} + b = w_1x_1 + \dots + w_nx_n + b. \quad (2.13)$$

The output of the sum net function is a positive or negative floating-point value which is passed to the activation function. ANNs can learn the non-linear relationship between input and output vectors if the activation function is non-linear. ANNs support various non-linear activation functions. The most popular activation functions are sigmoidal and hyperbolic tangent [Word 11]. In this thesis, the Elliot symmetric sigmoid activation function is used. It works approximately four times faster than the symmetric sigmoid since it does not use exponents [Beal 16].

How many neurons are needed to train an ANN to make reliable predictions and not to memorise patterns? This is one of the most challenging questions. An optimum number of neurons can be ascertained after conducting empirical analysis. Some general guidelines on choosing the number of neurons can be found in [Sing 03, Beal 16].

Different distribution of neurons among the input-hidden-output layers, the number of layers and the input-output procedures influence the architecture and the scope of an application [Hoss 17]. In the present thesis, the multilayer feed-forward network (MLFFNN) is used. According to [Shar 13], the MLFFNN is

a universal approximator which can be used when little prior knowledge of the relationship between inputs and targets is available. The MLFFNN with one hidden layer generally produces excellent results [Sing 03, Beal 16]. If the results are not adequate, more layers might be added; notably, more training data are needed in such case.

Broadly, to train an MLFFNN is not an easy process since it has hidden layers. The optimal values of the hidden neuron outputs are not known. Hence, the weight of each hidden neuron cannot be adjusted appropriately knowing only the overall error value in the output layer of the network. According to several authors [Hayk 99, Word 11, Niel 15], the most appropriate technique for training the MLFFNN is back propagation learning, or simply propagation of error. It is a supervised learning algorithm introduced by Bryson and Ho in 1969 and rediscovered by Werbos in 1974 [Hayk 99]. The process consists of two passes through the network: the forward propagation and the backwards propagation. The input vector is fed into the network during the forward propagation and then transmitted to the output layer through the hidden layers. The output of the network is then compared to the desired output and an error value is calculated for each of the neurons in the output layer. The error values are then propagated backwards.

The loss (also cost or error) function shows the effectiveness of the training process (correction of weights): how far the computed values of the output neurons are away from the target values. Mathematically, the desired value of the cost function is a global minimum as it is the point where the error of the training is the lowest. To reach the global minimum by minimising the cost function is not easy as the process is tangled by local minima. Furthermore, the presentation of the training set to the system only once rarely gives the desired result. That means, the system has to go through the same training set once again and discover more relevant associations between the input and output values by adjusting the weights. This leads to the error-performance surface or simply the error surface. The true error surface is averaged over all possible input-output examples. For the network to improve the training performance, the operating point has to move down towards the global minimum on the error surface.

The procedure used to carry out the learning process in the ANN is called an optimisation algorithm. The algorithm finds a set of weights and biases which makes the cost as small as possible. Some optimisation algorithms are the gradient descent, the conjugate gradient, the Newton method, the Quasi-Newton method and the Levenberg-Marquardt algorithm [Hayk 99]. The algorithms have different characteristics and performance in terms of memory requirements, processing

speed, and numerical precision. The description of each technique is out of the scope of the present thesis (detailed information about the optimisation algorithms can be found in various resources, for example, [Hayk 99, Niel 15]).

A list of the optimisation algorithms implemented in the MATLAB Neural Network Toolbox training functions can be found in [Beal 16] (the choice of the computational environment was motivated by the availability and popularity of machine learning libraries at the beginning of the PhD studies). According to Lahiri and Ghanta [Lahi 09], no algorithm is cross-functional to suit to all problems; therefore, a quantitative analysis has to be performed in order to find a suitable optimisation algorithm for the damage parameter quantification problem. Table 2.1 [Beal 16] summarises the Matlab training functions used in the present thesis having regard to the optimisation algorithms implemented in them.

**Table 2.1:** Training functions of the ANNs.

Training function	Abbr.	Description
<i>trainrp</i>	RP	Resilient back propagation is a network training function that updates weight and bias values according to the resilient back propagation algorithm. It is a simple batch mode training algorithm with fast convergence and minimal storage requirements.
<i>trainscg</i>	SCG	Scaled conjugate gradient back propagation is a network training function that updates weight and bias values according to the scaled conjugate gradient method. The method performs well particularly for networks with a large number of weights.
<i>trainbfg</i>	BFG	Broyden-Fletcher-Goldfarb-Shanno back propagation is a network training function that updates weight and bias values according to the quasi-Newton method. It requires more storage and has more computation in each iteration than the conjugate gradient method, but usually converges in fewer iterations.
<i>trainlm</i>	LM	Levenberg-Marquardt back propagation is a network training function that updates weight and bias values according to Levenberg-Marquardt optimization. It is the fastest training algorithm for networks of moderate size, but slower than the gradient methods.
<i>trainbr</i>	BR	Bayesian regularisation back propagation is a network training function that updates the weight and bias values according to Levenberg-Marquardt optimization. It minimises the combination of squared errors and weights penalising large weights, and then determines the correct combination to produce a network that generalises well. The method performs well even on small noisy datasets since it does not require the validation dataset to be separated from the training dataset.

### 2.3.2 Random forests

This subsection is partially based on the article [Jaan 16].

The random forest (RF) is a classifier defined by Breiman for classification and regression problems. The statistical method is based on a large set of un-

pruned decision trees known as classifiers. The unpruned decision trees, or the full trees, arrange information in a tree-like structure: leaves represent classifications which are referred to as labels, non-leaf nodes are features, and branches represent conjunctions of features that lead to the classifications. This structure is used to predict potential values of data attributes. A collection of the unpruned trees forms an ensemble or a forest.

The idea of combining multiple decision trees originated with Williams in 1987 [Will 87]. Ho [Ho 95] developed it further: for constructing each tree, he used a fixed portion of randomly selected features or a subspace. The method is known as the random decision forest. A bit later, Dietterich [Diet 00] proposed an idea of the random subspaces for constructing each node of the tree; in other words, to use a fixed portion of randomly selected features at each split of the node. Finally, in 2001 Breiman [Brei 01] formulated the whole RF algorithm as follows.

1. Generate  $n$  random sets (bootstrap replicate sets) of the original dataset, where  $n$  denotes the number of trees in the ensemble. The size of each random set is the same as the size of the original set of the data; however, in the bootstrap replicate set, the patterns are random: some patterns are chosen several times from the original set, some are not present in the replicate set at all. Each bootstrap replicate set does not contain approximately one-third of the original observations; these are called the “out-of-bag” patterns.
2. Grow the forest of the unpruned classification or regression trees with as a small subset of observations at each leaf as possible. For each tree, use the corresponding bootstrap set and recursively apply the following sub-algorithm to construct each tree:
  - (a) choose a random sample of predictors  $p$  without replacement (if  $p$  is equal to the size of the original set, the case is called bagging);
  - (b) choose a predictor out of  $p$  which produces the best split;
  - (c) split the set into two subsets at the node;
  - (d) repeat the procedure for each subsequent split until the tree is as large as desired.

Importantly, pruning is not allowed at this stage [Rio 14].

3. Evaluate each observation using all the trees using the out-of-bag set.
4. Predict new observations by aggregating the predictions of each tree of the forest (that means, the majority votes for the classification tasks or an average result for the regression tasks).



Proceeding from the description of the algorithm, the RF has three parameters at most to adjust:

- $n$  - the number of trees (the generalisation error converges as the number of trees in the forest becomes larger),
- $p$  - the number of random features to be used at each node (the smaller is number  $p$ , the more reduced the correlation is);
- the number of observations that the terminal nodes may contain (the smaller the number, the more sensitive to noise the tree is).

The other parameters (the variables in the bootstrap sets and nodes) are random. The detailed guidance on adjusting these parameters can be found in [Liaw 02]. Some of them are listed below.

- The best way to determine how many trees are necessary is to compare the predictions made by a forest to the predictions made by a subset of the forest. When the subsets work as well as the full forest, the number of trees is enough.
- For selecting  $p$ , Breiman suggests trying the default number, a half of the default, and doubled of the default, and pick the best (for the regression tasks, the default  $p$  is  $1/3$  of the number of the features in the patterns ( $P$ ); in case of the classification task, the default  $p$  is  $\sqrt{P}$ ).

The double randomness (at the generation of the bootstrap sets via bagging and the random subspaces at the nodes) decorrelates the trees in the ensemble allowing highly correlated variables to play almost equivalent roles. The decision based on the output from all the classifiers increases the accuracy of the prediction made by one tree-structured classifier and makes the RF more stable and less prone to overfitting. This explains the efficiency and popularity of the RFs in relation to other classification and regression algorithms, such as discriminant analysis, support vector machines and ANNs. Furthermore, the RF is simple, fast (can be easily parallelised) and robust to the outliers and noise [Brei 01].

Due to the numerous advantages, the RF has been adopted towards data mining, image analysis and applied statistics. Wu et al. [Wu 14] successfully applied the RFs to the study on imbalanced text categorisation. Calderoni et al. [Cald 15] developed a complex method for indoor localisation using the RF classifiers. Tüselmann et al. [Tuse 15] described a new method based on the RF for determining journal rankings. In the field of structural engineering, only a few papers on the application of the RFs can be found. For example, Sainlez and

Heyen [Sain 10] conducted performance monitoring of an industrial boiler in 2010. Tooke et al. [Took 14] used the RFs to predict the age of buildings. Zhou et al. [Zhou 14] applied the RFs for damage detection in a four-storey steel building model. Nevertheless, a larger number of articles addressed the inverse problems of structural mechanics by applying the predecessors of the RF, for example, CART and C4.5 methods in [Yang 05, Sun 07, Karb 14].

## 2.4 Evaluation criteria

A predictive model building with the aid of the machine learning methods refers to selecting the “optimal” architecture, data representation, training algorithm, training parameters, and terminating criteria such that some desired level of performance is achieved. With this, validation is a critical aspect of any model construction and evaluation. Verification helps measure and compare the performance of different models as well as evaluate the superiority of model architecture, learning algorithm, or application of the model.

Although no single well-formulated theoretical methodology exists for the machine learning model verification, the verification process is usually based upon some specified network performance measure on the data that have not been used in the model construction - a testing set (this implies that the initial data set is split into the training, validation and test sets). The evaluation criterion quantifies the prediction error. In the present thesis, the mean square error (MSE) is used since it is widely used in most articles on computational mechanics:

$$MSE = \frac{1}{N} \sum_{i=1}^N (y_i - t_i)^2, \quad (2.14)$$

where  $N$  is the number of patterns in the set,  $y_i$  and  $t_i$  denote the predicted output and the target value, respectively. The criterion estimates the distance between the original outputs and the estimated outputs avoiding the error sign by squaring and shows the average magnitude of the forecast error.

In order to compare the results of multiple tests and machine learning techniques, all the programs were written in the Matlab environment. The programs were run on a MacBook Pro laptop with a 2.5 GHz Intel Core i5 processor and 8GB 1600 MHz RAM.

## 2.5 Conclusion

In this chapter, a classification of damage identification approaches was given schematically. Particular emphasis was placed on the Haar wavelets and some machine learning methods since these would be the main tools for solving non-inverse and inverse problems described in the thesis.

# Chapter 3

## Mathematical models

In the vibration analysis, the model-based methods require mathematical modelling, derivation of the governing equations, solution of the equations, and interpretation of the results [Rao 05]. However, it is impossible to consider all the details in the mathematical analysis if the vibrating system is very complex. In such cases, the overall behaviour of the complex system can be determined by considering a simple model. To a vast extent, several theories are associated with beam deformations/displacements and stresses, such as Rayleigh, Euler-Bernoulli, Timoshenko. To come up with a suitable mathematical model for a vibrating system, some judgement has to be made. Linear models permit quick solutions and are simple to handle; however, non-linear models sometimes reveal specific characteristics of the system that cannot be predicted using the linear models. In the present thesis, the Euler-Bernoulli beam theory underlies the research since it is the simplest beam model and yet widely used in engineering. Proceeding from the beam theory, various mathematical models of (non-)homogeneous (non-)uniform beams with (non-)classical boundary conditions and the corresponding equations of motion are presented in detail. The derived analytical models are used in the pertinent (non-)inverse problems of the thesis.

### 3.1 Uniform beams

#### 3.1.1 Governing equations of Euler-Bernoulli beams

The Euler-Bernoulli beam theory is the oldest beam model, yet it is commonly used in civil engineering. The Euler-Bernoulli beam theory is a simplified theory of deformation of a thin elastic beam. Due to the bending moment and the transverse

displacements, the theory comprises the strain energy and kinetic energy. The key kinematic assumptions of the Euler-Bernoulli beam theory are:

- the cross-sections of the beam are rigid;
- the cross-sections remain planar and normal to the deformed axis of the beam.

The Euler-Bernoulli beam theory provides a reasonable approximation for many problems, including the calculation of load-carrying capacity, deflections and internal forces of beams. Based on the Euler-Bernoulli beam theory, the following assumptions are used in the present thesis:

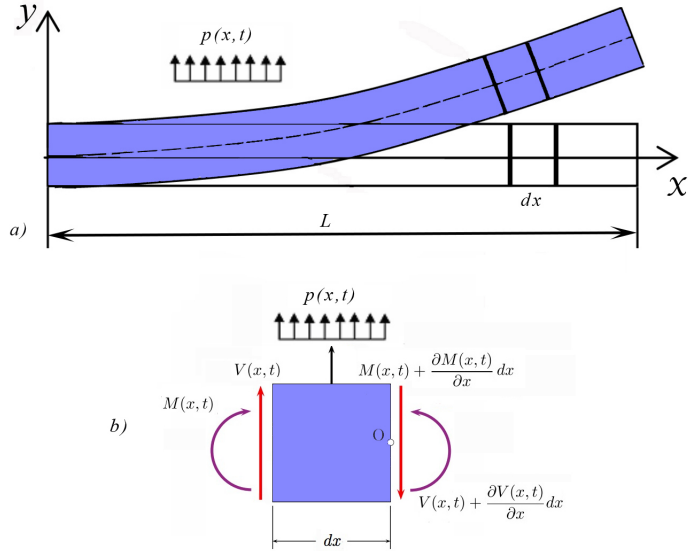
1. *geometry*: the thickness and width of the beam are significantly smaller compared with the length;
2. *stresses*: the load distribution is lateral; the stresses perpendicular to the beam length are much smaller than parallel and can be neglected;
3. *neutral axis*: the neutral axis undergoes no extension;
4. *deformation*: the beam deformations are dominated by pure bending and considerably small compared with the thickness of the beam;
5. *normality*: the plane sections that are perpendicular to the neutral axis remain so at bending; each fibre in the cross-section changes length proportional to its distance from the neutral axis;
6. *linearisation*: the angular distortion due to the shear force is negligible compared with the bending deformation.

A sample uniform homogeneous beam and its properties are shown in Figure 3.1 and Table 3.1. In the uniform beam, the material density  $\rho$ , the cross-section  $A$  and the bending stiffness  $EI$  are constants. The combination of the tensile and compressive stresses in the fibres of the beam produces the internal bending moment. According to the Euler-Bernoulli beam theory, the bending moment  $M$  is proportional to the curvature of the bending [Bala 04]:

$$M(x, t) = EI \frac{\partial^2 y(x, t)}{\partial x^2}. \quad (3.1)$$

In Figure 3.1, the balance of the forces in  $y$  direction is

$$V(x, t) + p(x, t)dx - \left( V(x, t) + \frac{\partial V(x, t)}{\partial x} dx \right) = 0. \quad (3.2)$$



**Figure 3.1:** An Euler-Bernoulli beam: (a) bending of the beam; (b) equilibrium for a small beam element (the bending moments  $M(x, t)$  and the shear forces  $V(x, t)$  are positive in the clockwise direction).

**Table 3.1:** Beam properties.

$L$	length of the beam
$b$	width of the beam
$h$	thickness of the beam
$A$	cross-sectional area of the beam
$\rho$	linear mass density per unit length
$E$	elasticity modulus
$I$	second moment of area or moment of inertia (in case of a rectangular beam: $I = \frac{bh^3}{12}$ [Bala 04])
$x$	axial coordinate along the neutral axis
$t$	time
$y(x, t)$	vertical displacement of the beam
$M(x, t)$	internal bending moment
$V(x, t)$	shear force
$p(x, t)$	load density (force per unit length of the beam)
$W(x)$	mode shape
$\omega$	natural frequency of vibration
$f_{cnf}$	circular frequency of vibration

Rearranging (3.2), the load-deflection equation is as follows:

$$p(x, t) = \frac{\partial V(x, t)}{\partial x}. \quad (3.3)$$

Thus, the loading per unit length of the beam relates to the change of the shear force along the beam.

The balance of moments at the rightmost edge point  $x + dx$  (Figure 3.1) of the beam element is

$$M(x, t) + V(x, t)dx + p(x, t)dx \frac{dx}{2} - \left( M(x, t) + \frac{\partial M(x, t)}{\partial x} dx \right) = 0. \quad (3.4)$$

Neglecting the second-order term  $p(x, t)dx \frac{dx}{2}$ , the shear-deflection equation is obtained

$$V(x, t) = \frac{\partial M(x, t)}{\partial x}. \quad (3.5)$$

Thus, the shear force relates to the change of the bending moment along the beam.

Substituting (3.1) and (3.5) into (3.3), the following relation is obtained

$$p(x, t) = \frac{\partial^2}{\partial x^2} \left( EI \frac{\partial^2 y(x, t)}{\partial x^2} \right) = EI \frac{\partial^4 y(x, t)}{\partial x^4}. \quad (3.6)$$

For a beam subjected to the free vibration (no external forces are applied) about its own static equilibrium position under the weight of the beam, the load per unit length is equal to the inertia force due to the internal load times acceleration [Pras 11]:

$$p(x, t) = -m \frac{\partial^2 y(x, t)}{\partial t^2}. \quad (3.7)$$

Taking into account (3.6) and (3.7), expressing the mass of the beam via its density and volume ( $m = \rho A$ ), the governing differential equation associated with the free transverse vibration of the Euler-Bernoulli beam is

$$EI \left( \frac{\partial^4 y(x, t)}{\partial x^4} \right) + \rho A \frac{\partial^2 y(x, t)}{\partial t^2} = 0. \quad (3.8)$$

The equation (3.8) involves a fourth order derivative with respect to the axial coordinate and a second order derivative with respect to time. The solution of (3.8) is sought using the method of separation of variables [Karn 01]:

$$y(x, t) = W(x)T(t), \quad (3.9)$$

where  $W$  is independent of time and  $T$  is independent of coordinate. Substituting (3.9) into (3.8), dividing it by  $\rho AW(x)T(t)$  and rearranging the terms, the following equation is obtained [Bala 04]

$$\frac{EI}{\rho AW(x)} \frac{d^4 W(x)}{dx^4} = -\frac{1}{T(t)} \frac{d^2 T(t)}{dt^2}. \quad (3.10)$$

The left term of (3.10) does not convert if  $t$  changes, and vice versa, the right term of (3.10) does not convert if  $x$  changes; therefore, the ratio on each side must be a constant; that is

$$\frac{EI}{\rho AW(x)} \frac{d^4 W(x)}{dx^4} = -\frac{1}{T(t)} \frac{d^2 T(t)}{dt^2} = \omega_*^2, \quad (3.11)$$

where  $\omega_*^2$  is a positive constant (this requirement can be verified due to the nature of the particular vibration problem), and  $\omega_*$  is the natural frequency of free vibrations. Introducing the natural frequency parameter  $k_*$ :

$$k_*^4 = \frac{\omega_*^2 \rho A}{EI}, \quad (3.12)$$

(3.10) takes the form of two differential equations:

$$\frac{d^4 W(x)}{dx^4} - k_*^4 W(x) = 0. \quad (3.13)$$

$$\frac{d^2 T(t)}{dt^2} + \omega_*^2 T(t) = 0. \quad (3.14)$$

A general solution of (3.13) for a mode shape (eigenfunction) is given by [Cocs 11]

$$W(x) = C_1 \sin(k_* x) + C_2 \cos(k_* x) + C_3 \sinh(k_* x) + C_4 \cosh(k_* x), \quad (3.15)$$

where  $C_i$  ( $i = 1, \dots, 4$ ) are the arbitrary constants of the integration to be determined later from the boundary conditions and  $W(x)$  is the mode shape of the beam. Since the beam vibrates periodically with no damping (free vibration), it has an infinite number of mode shapes and natural frequencies derived from the trigonometric general solution (Figure 3.2 [Kova 10]). The natural frequency of vibration associated with a particular mode shape can be found from (3.12):

$$\omega_* = k_*^2 \sqrt{\frac{EI}{\rho A}}, \quad (3.16)$$



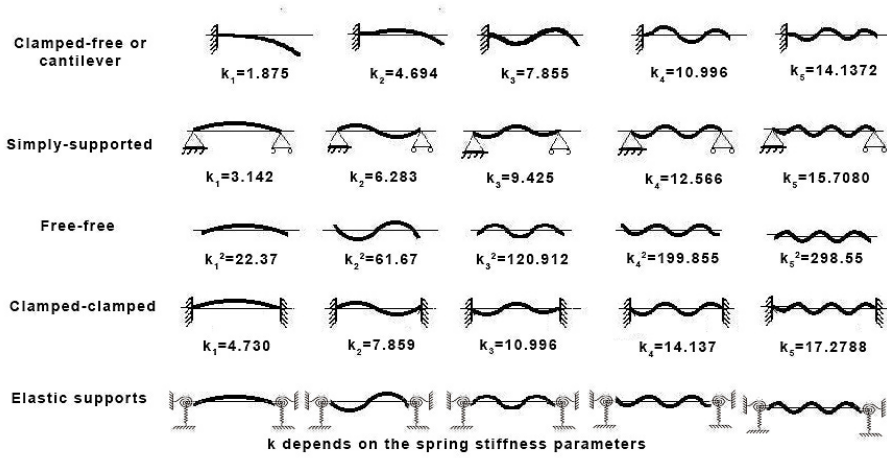


Figure 3.2: The first five mode shapes and natural frequencies.

which is related to the circular natural frequency as follows:

$$f_{cnf} = 2\pi\omega_*. \quad (3.17)$$

For the convenience of further calculations, the first, second and third derivatives of the general solution  $W(x)$  are calculated and presented as follows:





$$\begin{aligned} \frac{dW}{dx} &= C_1 k_* \cos(k_* x) - C_2 k_* \sin(k_* x) + C_3 k_* \cosh(k_* x) + C_4 k_* \sinh(k_* x), \\ \frac{d^2 W}{dx^2} &= -C_1 k_*^2 \sin(k_* x) - C_2 k_*^2 \cos(k_* x) + C_3 k_*^2 \sinh(k_* x) + C_4 k_*^2 \cosh(k_* x), \\ \frac{d^3 W}{dx^3} &= -C_1 k_*^3 \cos(k_* x) + C_2 k_*^3 \sin(k_* x) + C_3 k_*^3 \cosh(k_* x) + C_4 k_*^3 \sinh(k_* x). \end{aligned} \quad (3.18)$$

The unknown constants  $C_i$  and the natural frequency parameter  $k_*$  can be determined from the boundary conditions of the beam.

### 3.1.2 Boundary conditions

Various boundaries restrict lateral or rotational movements so as to satisfy stability conditions and limit the deformations to a certain allowance. Classical boundary conditions of the beam are tabulated in Table 3.2 [Bala 04]. A simply supported beam is supported by a pin (hinged) at one end and a roller at the other end

**Table 3.2:** Classical boundary conditions at the left and right ends of the beam.

<p>free ends</p> 	<p><math>bending\ moment = 0</math></p> <p><math>shear\ force = 0</math></p>	<p>Left end: <math>EI \frac{\partial^2 y(0, t)}{\partial x^2} = 0, EI \frac{\partial^3 y(0, t)}{\partial x^3} = 0</math></p> <p>Right end: <math>EI \frac{\partial^2 y(L, t)}{\partial x^2} = 0, EI \frac{\partial^3 y(L, t)}{\partial x^3} = 0</math></p>
<p>pinned (hinged) ends</p> 	<p><math>deflection = 0</math></p> <p><math>bending\ moment = 0</math></p>	<p>Left end: <math>y(0, t) = 0, EI \frac{\partial^2 y(0, t)}{\partial x^2} = 0</math></p> <p>Right end: <math>y(L, t) = 0, EI \frac{\partial^2 y(L, t)}{\partial x^2} = 0</math></p>
<p>guided (sliding) ends</p> 	<p><math>slope = 0</math></p> <p><math>shear\ force = 0</math></p>	<p>Left end: <math>\frac{\partial y(0, t)}{\partial x} = 0, EI \frac{\partial^3 y(0, t)}{\partial x^3} = 0</math></p> <p>Right end: <math>\frac{\partial y(L, t)}{\partial x} = 0, EI \frac{\partial^3 y(L, t)}{\partial x^3} = 0</math></p>
<p>clamped (fixed) ends</p> 	<p><math>deflection = 0</math></p> <p><math>slope = 0</math></p>	<p>Left end: <math>y(0, t) = 0, \frac{\partial y(0, t)}{\partial x} = 0</math></p> <p>Right end: <math>y(L, t) = 0, \frac{\partial y(L, t)}{\partial x} = 0</math></p>

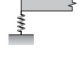

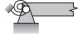
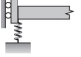
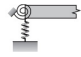
(sliding end). A beam with a fixed (clamped) support at one end with no support (free) at the other end is called a cantilever.

In many practical applications, it is needed to store or deposit mechanical energy emerging during the vibration. Unlike the classical boundary conditions, the elastic boundaries fulfil these tasks particularly well. The elastic boundaries are usually made of springs (such as an extension spring, a compression spring, a torsion spring, or a flexure spring). In most applications, it is assumed that the springs have negligible mass and damping. The boundary conditions in the presence of the translational or rotational springs at  $x = 0$  can be presented as follows:

$$\begin{aligned}
 EI \frac{\partial^3 y(0, t)}{\partial x^3} + K_T y(0, t) &= 0, \\
 EI \frac{\partial^2 y(0, t)}{\partial x^2} - K_R \frac{\partial y(0, t)}{\partial x} &= 0.
 \end{aligned} \tag{3.19}$$

Some non-classical boundary conditions at the left end of the beam are tabulated in Table 3.3 [Bala 04]. The multipliers  $K_T$  and  $K_R$  are the stiffness coefficients of the translational and rotational springs, respectively. The boundary conditions at the right end of the beam can be formulated analogically [Bala 04]. The first

**Table 3.3:** Non-classical boundary conditions at the left end of the beam.

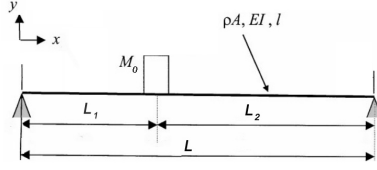
<p>free end with a translational spring</p> 	$EI \frac{\partial^2 y(0, t)}{\partial x^2} = 0$ $EI \frac{\partial^3 y(0, t)}{\partial x^3} + K_T y(0, t) = 0$
<p>free end with a rotational spring</p> 	$EI \frac{\partial^2 y(0, t)}{\partial x^2} - K_R \frac{\partial y(0, t)}{\partial x} = 0$ $EI \frac{\partial^3 y(0, t)}{\partial x^3} = 0$
<p>pinned end with a rotational spring</p> 	$y(0, t) = 0$ $EI \frac{\partial^2 y(0, t)}{\partial x^2} - K_R \frac{\partial y(0, t)}{\partial x} = 0$
<p>sliding end with a translational spring</p> 	$\frac{\partial y(0, t)}{\partial x} = 0$ $EI \frac{\partial^3 y(0, t)}{\partial x^3} + K_T y(0, t) = 0$
<p>free end with a rotational and a translational springs</p> 	$EI \frac{\partial^2 y(0, t)}{\partial x^2} - K_R \frac{\partial y(0, t)}{\partial x} = 0$ $EI \frac{\partial^3 y(0, t)}{\partial x^3} + K_T y(0, t) = 0$

few calculated natural frequencies, mode shapes and node points of intact Euler-Bernoulli beams with different boundary conditions subjected to free vibration can be found in [Bala 04].

### 3.1.3 Euler-Bernoulli beam with a mass point

The present subsection of the thesis is based on the article [Hein 09]. The section provides an analytical solution to the free vibrations of Euler-Bernoulli beams of length  $L$  with a concentrated point mass  $M_0$  located at  $x = L_1$  (Figure 3.3).

The governing equation of motion of the Euler-Bernoulli beam and its solution are shown in (3.8) and (3.15). According to de Rosa [Rosa 96], the mode shape of a vibrating beam with a discrepancy can be presented as a system of two mode



**Figure 3.3:** An Euler-Bernoulli beam with a concentrated point mass.

shapes  $W_1(x)$  and  $W_2(x)$  (the approach is used in all solutions of this thesis):

$$\begin{cases} W_1(x) = C_1 \sin(k_* x) + C_2 \cos(k_* x) + C_3 \sinh(k_* x) + C_4 \cosh(k_* x), x \in [0, L_1] \\ W_2(x) = C_5 \sin(k_* x) + C_6 \cos(k_* x) + C_7 \sinh(k_* x) + C_8 \cosh(k_* x), x \in [L_1, L]. \end{cases} \quad (3.20)$$

The unknown constants  $C_i (i = 1, \dots, 8)$  can be determined from the boundary conditions (Table 3.2 or 3.3) and the continuity conditions at  $x = L_1$  [Karn 01]:

$$\begin{aligned} W_1 &= W_2, \\ \frac{dW_1}{dx} &= \frac{dW_2}{dx}, \\ \frac{d^2W_1}{dx^2} &= \frac{d^2W_2}{dx^2}, \\ \frac{d^3W_1}{dx^3} + \alpha k_*^4 W_1 &= -\frac{d^3W_2}{dx^3}, \end{aligned} \quad (3.21)$$

where  $\alpha$  is the mass ratio defined by  $M_0/(\rho A)$ . The first three conditions originate from the continuity requirements of deflection, slope and bending moment at  $x = L_1$ , whereas the fourth requirements shows the discrepancy of the shear force depending on mass. The differentiation of the mode shape is shown in (3.18).

### 3.1.4 Euler-Bernoulli beam with cracks

This subsection is based on the article [Fekl 13a] in which an open crack in a homogeneous Euler-Bernoulli beam is discussed.

According to Rizo et al. [Rizo 90], a cracked uniform beam can be simulated as two uniform beams joined together by a rotational spring at the crack due to the localised crack effect. The continuity and compatibility conditions at the crack

( $x = L_1$ ) take the form:

$$\begin{aligned}
W_1 &= W_2, \\
\frac{d^2 W_1}{dx^2} &= \frac{d^2 W_2}{dx^2}, \\
\frac{d^3 W_1}{dx^3} &= \frac{d^3 W_2}{dx^3}, \\
W_1 + c \frac{d^2 W_1}{dx^2} &= W_2,
\end{aligned} \tag{3.22}$$

where  $W_1$  and  $W_2$  are the mode shapes of the left and right beam sections, respectively. The bending constant of the massless spring  $c$  is presented as follows [Dima 13]:

$$c = 5.346 \frac{h}{EI} J\left(\frac{a}{h}\right), \tag{3.23}$$

where  $h$  is the thickness of the beam,  $a$  is the depth of the crack and  $J(\frac{a}{h})$  is the dimensionless local compliance function proposed by Paipetis, Dimarogonas and Chondros [Dima 13]:

$$\begin{aligned}
J\left(\frac{a}{h}\right) &= 1.8624\left(\frac{a}{h}\right)^2 - 3.95\left(\frac{a}{h}\right)^3 + 16.375\left(\frac{a}{h}\right)^4 - 37.226\left(\frac{a}{h}\right)^5 + 76.81\left(\frac{a}{h}\right)^6 - \\
&\quad - 126.9\left(\frac{a}{h}\right)^7 + 172\left(\frac{a}{h}\right)^8 - 143.97\left(\frac{a}{h}\right)^9 + 66.56\left(\frac{a}{h}\right)^{10}.
\end{aligned} \tag{3.24}$$

The governing equation of motion of the Euler-Bernoulli beam shown in (3.8) can be solved using (3.20) taking into account the boundary conditions (Table 3.2 or 3.3) and the continuity and compatibility conditions (3.22).

### 3.1.5 Euler-Bernoulli beam with cracks and on elastic foundation

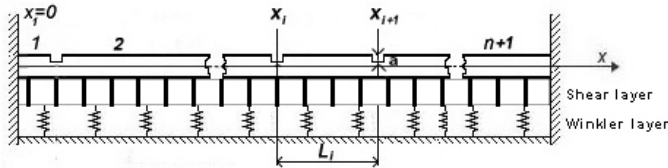
This subsection is based on the article [Jaen 16] in which a cracked Euler-Bernoulli beam on an elastic foundation is investigated.

The soil-structure interaction problems play an important role in civil engineering constructions, such as pipelines, road surfaces, building foundations. Some problems (for instance, contact pressure distribution, cracks in the medium) can be idealised and solved by modelling beams on an elastic foundation.

Several mathematical models of elastic foundations can be found in literature, for example, Winkler, Pasternak, Vlasov, Filonenko-Borodich, Leontiev models; however, the first two models are widely used in engineering for static and dynamic analysis due to their simplicity. The present subsection of the thesis focuses on the beams on the Pasternak foundation.

In the Winkler one parameter model, the foundation is composed of infinitely close elastic springs which are independent of each other; the vertical surface displacement of the beam is assumed to be proportional to the contact pressure at any point. Pasternak improved the Winkler model by adding shear interactions. The Pasternak two parameter model represents a system of closely placed elastic springs coupled to each other with the elements which transmit the shear force proportional to the slope of the foundation surface [Cele 11]. The Pasternak foundation model is used in several soil structure interactions, for example, road pavement, rigid concrete pavement for highways and airports, a bridge resting on elastomeric bearings or excavation retaining walls and tunnels in the soil.

In Figure 3.4, a clamped Euler-Bernoulli beam of length  $L$  is placed on the Pasternak foundation. The beam has  $n$  cracks. According to Rizos et al. [Rizo 90],



**Figure 3.4:** A clamped beam on Pasternak foundation.

Shifrin and Ruotolo [Shif 99], a beam with  $n$  cracks can be modelled as a beam divided into  $n + 1$  sections connected by elastic springs. The differential equation of the transverse vibration in each region  $x \in [x_i, x_{i+1}]$  of the beam placed on the Pasternak foundation is as follows [Elis 01a]:

$$EI \frac{\partial^4 y_i(x, t)}{\partial x^4} - G_2 \frac{\partial^2 y_i(x, t)}{\partial x^2} + G_1 y_i(x, t) + \rho A \frac{\partial^2 y_i(x, t)}{\partial t^2} = 0, \quad (3.25)$$

where  $G_1$  is the Winkler foundation modulus,  $G_2$  is the shear modulus of the Pasternak foundation,  $i$  is the number of the section ( $i = 1, \dots, n + 1$ ) and  $y_i(x, t)$  is the transverse deflection in the  $i$ -th section. The solution of (3.25) is sought in the form shown in (3.9). Substituting (3.9) into (3.25), the equation of the transverse vibration (3.25) takes the form of:

$$\frac{d^4 W_i(x)}{dx^4} - \mu \frac{d^2 W_i(x)}{dx^2} + (\gamma - \tilde{k}) W_i(x) = 0, \quad (3.26)$$

where

$$\mu = \frac{G_2}{EI}, \gamma = \frac{G_1}{EI}, \tilde{k} = \frac{m\omega_*^2}{EI}. \quad (3.27)$$

The characteristic equation of (3.26) can be presented as follows:

$$\lambda^4 - \mu\lambda^2 + (\gamma - \tilde{k}) = 0 \quad (3.28)$$

and the general solution of (3.26) for the present vibration problem can be presented as follows [Rosa 99]:

$$W_i = C_{1,i}e^{\lambda_1 x} + C_{2,i}e^{\lambda_2 x} + C_{3,i}e^{\lambda_3 x} + C_{4,i}e^{\lambda_4 x}, \quad (3.29)$$

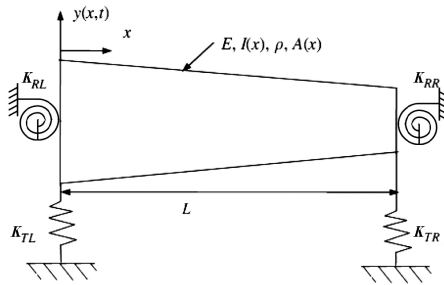
where  $\lambda_1, \dots, \lambda_4$  are the roots of (3.28) and  $C_{1,i}, \dots, C_{4,i}$  are the integration constants. The equation (3.26) should be solved separately for each beam section  $i$  ( $i = 1, \dots, n+1$ ). The solution for the whole beam can be put together taking into account the continuity and boundary conditions presented in (3.22) and Table 3.2 or 3.3.

## 3.2 Non-uniform beams

### 3.2.1 Non-uniform Euler-Bernoulli beam on elastic supports

The present subsection refers to the article [Fekl 10] in which the governing equation of the transverse vibrations of the Euler-Bernoulli beam with a varying cross-sectional area is presented.

In this subsection, a non-uniform beam of length  $L$  is considered. The beam has a variable cross-section along its length (Figure 3.5); variables  $K_{RL}$  and  $K_{RR}$  denote the stiffness coefficient of the corresponding rotational springs at the left



**Figure 3.5:** A linearly tapered beam with rotational and translational elastic constraints.

and right ends of the beam, respectively; variables  $K_{TL}$  and  $K_{TR}$  denote the stiffness coefficient of the corresponding translational springs at the left and right ends of the beam. The moment of inertia and the cross-sectional area are functions

of the coordinate, that is  $I(x)$  and  $A(x)$ . From (3.6) - (3.9), the equation of the transverse vibrations of a tapered beam can be presented as follows:

$$\frac{d^2}{dx^2} [EI(x) \frac{d^2 W(x)}{dx^2}] - \omega_*^2 \rho A(x) W(x) = 0, \quad (3.30)$$

where  $W(x)$  is the mode shape,  $A(x)$  is the cross-sectional area at the point  $x$ ,  $I(x)$  is the moment of inertia,  $\rho$  is the mass density of the beam material and  $E$  is Young's modulus. In the present thesis, it is assumed that the functions  $I(x)$  have derivatives up to the second order. From (3.30), it yields

$$\frac{d^4 W(x)}{dx^4} I(x) + 2 \frac{d^3 W(x)}{dx^3} \frac{dI(x)}{dx} + \frac{d^2 W(x)}{dx^2} \frac{d^2 I(x)}{dx^2} - \frac{\omega_*^2 \rho}{E} A(x) W(x) = 0. \quad (3.31)$$

The boundary conditions in the presence of the translational and rotational spring constraints at  $x = 0$  are presented as follows [Hsu 08]:

$$\frac{d}{dx} [EI(x) \frac{d^2 W(x)}{dx^2}] + K_{TL} W(x) = 0, \quad (3.32)$$

$$EI(x) \frac{d^2 W(x)}{dx^2} - K_{RL} \frac{dW(x)}{dx} = 0.$$

The boundary conditions at  $x = L$  can be formulated analogically. The solution of (3.31) is sought with the aid of the Haar wavelets in Chapter 4.

### 3.2.2 Non-homogeneous Euler-Bernoulli beam with delaminations

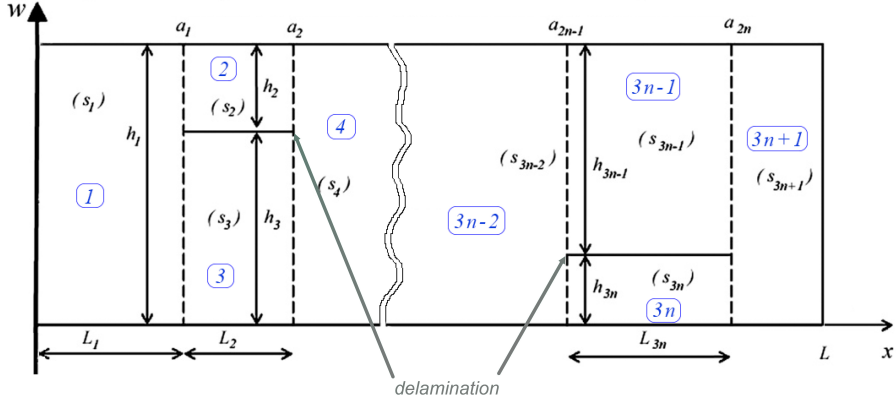
This subsection is based on the article [Hein 11b]. The section provides a mathematical model for composite beams with delaminations.

The free vibration of a laminated beam with  $n$  non-overlapping delaminations is considered. The laminated beam is presented as a combination of  $3n + 1$  beam sections connected at the delamination boundaries. Each beam section is treated as a classical Euler-Bernoulli beam model with  $L_i \gg h$ . It is assumed that the Euler-Bernoulli beam has a constrained mode, a rigid connector and a bending-extension coupling [Shu 04a]. The geometry of the beam is shown in Figures 3.6 and 3.7 [Shu 04a].

The governing equation for the intact beam sections is [Shu 04b]

$$D_i \frac{\partial^4 y_i(x, t)}{\partial x^4} + \rho_i A_i \frac{\partial^2 y_i(x, t)}{\partial t^2} = 0, \quad (3.33)$$





**Figure 3.6:** A beam with  $n$  non-overlapping delaminations.

where  $i$  is the beam section ( $i = 1, \dots, 3n+1$ );  $y_i(x, t)$  is the vertical displacement of the  $i$ -th beam section;  $D_i$  is the bending stiffness;  $\rho_i$  is the density of the material;  $A_i$  is the cross-sectional area;  $x$  is the axial coordinate and  $t$  is the time. Using the classical laminate theory, the bending stiffness  $D_i$  for the composite laminates can be determined as follows [Redd 97]:

$$D_i = D_i^* - \frac{B_i^2}{F_i}, \quad (3.34)$$

where

$$D_i^* = \frac{b}{3} \sum_{k=1}^{n_i} \bar{Q}_k (z_k^3 - z_{k-1}^3), \quad (3.35)$$

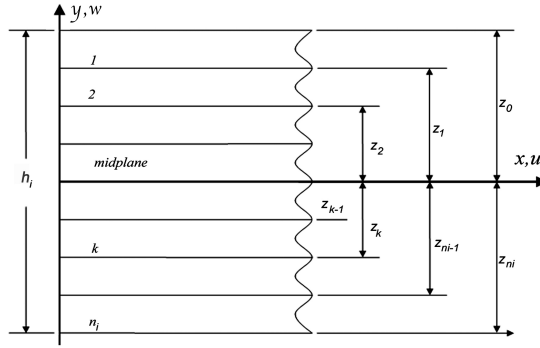
$$B_i = \frac{b}{2} \sum_{k=1}^{n_i} \bar{Q}_k (z_k^2 - z_{k-1}^2), \quad (3.36)$$

$$F_i = b \sum_{k=1}^{n_i} \bar{Q}_k (z_k - z_{k-1}), \quad (3.37)$$

$$\bar{Q}_k = Q_1^{(k)} \cos^4 \varphi + Q_2^{(k)} \sin^4 \varphi + 2(Q_1^{(k)} + 2Q_3^{(k)}) \sin^2 \varphi \cos^2 \varphi, \quad (3.38)$$

$$\begin{aligned}
Q_1^{(k)} &= \frac{E_a^{(k)}}{1 - \nu_{12}^{(k)} \nu_{21}^{(k)}}, \\
Q_2^{(k)} &= \frac{E_l^{(k)}}{1 - \nu_{12}^{(k)} \nu_{21}^{(k)}}, \\
Q_3^{(k)} &= G_{12}^{(k)}, \\
\nu_{21}^{(k)} &= \frac{\nu_{12}^{(k)} E_l^{(k)}}{E_a^{(k)}},
\end{aligned} \tag{3.39}$$

where  $D_i^*$  is the bending stiffness of the  $i$ -th section,  $B_i$  is the coupling stiffness of the  $i$ -th section,  $F_i$  is the extensional stiffness of the  $i$ -th section,  $\bar{Q}_k$  is the stiffness coefficient of the  $k$ -th lamina,  $b$  is the width,  $n_i$  is the number of the lamina,  $\nu_{12}^{(k)}$  and  $\nu_{21}^{(k)}$  are the longitudinal and transverse Poisson's ratios, respectively,  $E_a^{(k)}$  and  $E_l^{(k)}$  are the axial and lateral Young's moduli, respectively,  $\varphi$  is the angle of the  $k$ -th lamina orientation and  $z_k$  and  $z_{k-1}$  are the locations of the  $k$ -th lamina with respect to the mid-plane of the  $i$ -th beam section and  $G_{12}^{(k)}$  is the in-plane shear modulus (Figure 3.7).



**Figure 3.7:** A beam section with a delamination.

According to the constrained model [Shu 04b], the beam sections in the delaminated zone are forced to vibrate together. Hereof, the governing equations are

$$(D_{i_1} + D_{i_2}) \frac{\partial^4 y_i(x, t)}{\partial x^4} + (\rho_{i_1} A_{i_1} + \rho_{i_2} A_{i_2}) \frac{\partial^2 y_i(x, t)}{\partial t^2} = 0, \tag{3.40}$$

where  $i_1 = 2, 5, \dots, 3n - 1$ ;  $i_2 = 3, 6, \dots, 3n$ . The governing equations of the intact regions are shown in (3.33).

The solution to the beam as a whole is obtained in terms of the solutions of all beam components by enforcing the appropriate boundary and continuity conditions. In Figure 3.6, the continuity conditions for deflection, slope and shear force at the coordinate of the cross-section between  $(s_1)$  and  $(s_2) - (s_3)$ , for example,  $x = a_1$  are

$$\begin{aligned} W_1 &= W_2, \\ \frac{dW_1}{dx} &= \frac{dW_2}{dx}, \\ D_1 \frac{d^3 W_1}{dx^3} &= (D_2 + D_3) \frac{d^3 W_2}{dx^3}, \\ D_1 \frac{d^2 W_1(a_1)}{dx^2} + \frac{h_1^2}{4L_2} \left( \frac{F_2 F_3}{F_2 + F_3} \right) \left( \frac{dW_1(a_1)}{dx} - \frac{dW_2(a_2)}{dx} \right) &= (D_2 + D_3) \frac{d^2 W_2(a_1)}{dx^2}, \end{aligned} \quad (3.41)$$

where  $a_1$  denotes the coordinate of the cross-sections between  $(s_1)$  and  $(s_2) - (s_3)$ , whereas  $a_2$  is the coordinate between  $(s_2) - (s_3)$  and  $(s_4)$  beam sections;  $h_1$  is the thickness of the intact section  $s_1$ ;  $F_2$  and  $F_3$  are calculated from the continuity conditions of shear and moment at the delamination boundaries. The detailed derivation of conditions (3.41) is presented in [Shu 04a]. Similarly, the continuity conditions can be derived at  $x = a_2, \dots, a_{2n}$ . The boundary conditions at the supports  $x = 0, x = L$  are shown in Table 3.2 or 3.3.

### 3.2.3 Non-uniform axially functionally graded Euler-Bernoulli beam with elastic supports

This subsection is based on the article [Hein 11a] in which the Euler-Bernoulli beam with elastic boundary conditions, varying cross-sectional area and material properties along the axis is discussed.

In this subsection of the thesis, an axially graded Euler-Bernoulli beam of length  $L$  is considered. It is assumed that the material properties and the cross-section of the beam vary continuously along the length of the beam:  $E = E(x)$  and  $\rho = \rho(x)$ . For the simplicity of further calculations, a new quantity is introduced

$$k_*^4 = \frac{\omega_*^2 \rho_0 A_0}{E_0 I_0}, \quad (3.42)$$

where  $k_*^4$  is the natural frequency parameter, and  $\rho_0, A_0, E_0, I_0$  denote the values of  $\rho, A, E, I$  at  $x = 0$ , respectively.

The equation of motion for the transverse vibrations takes the form of:

$$\frac{d^2}{dx^2} [E(x)I(x) \frac{d^2 W(x)}{dx^2}] - k_*^4 \rho(x) A(x) W(x) = 0. \quad (3.43)$$

In the present thesis, it is assumed that the functions  $E(x)$  and  $I(x)$  have derivatives up to the second order. From (3.43), it yields

$$\begin{aligned} & \frac{d^4 W(x)}{dx^4} E(x) I(x) + 2 \frac{d^3 W(x)}{dx^3} \left[ \frac{dE(x)}{dx} I(x) + \frac{dI(x)}{dx} E(x) \right] + \\ & + \frac{d^2 W(x)}{dx^2} \left[ \frac{d^2 E(x)}{dx^2} I(x) + 2 \frac{dE(x)}{dx} \frac{dI(x)}{dx} + \frac{d^2 I(x)}{dx^2} E(x) \right] - \\ & - k_*^4 W(x) \rho(x) A(x) = 0, x \in [0, L]. \end{aligned} \quad (3.44)$$

The boundary conditions in the presence of the translational and rotational spring constraints ( $K_{TL}$ ,  $K_{RL}$ ) at  $x = 0$  are presented as follows:

$$\begin{aligned} & \frac{d}{dx} [E(x) I(x) \frac{d^2 W(x)}{dx^2}] + K_{TL} W(x) = 0, \\ & E(x) I(x) \frac{d^2 W(x)}{dx^2} - K_{RL} \frac{dW(x)}{dx} = 0. \end{aligned} \quad (3.45)$$

The boundary conditions at  $x = L$  can be formulated analogically. The equation (3.44) does not have an analytical solution. In the present thesis, the problem is solved using the Haar wavelets and their integration in Chapter 4.

### 3.2.4 Conclusion

This chapter addressed the free vibration of various beams. Namely, the following mathematical beam models were discussed in detail: a uniform beam with classical and elastic boundary conditions, a uniform beam with a point mass, a uniform beam with cracks, a uniform beam on the Pasternak foundation, a non-uniform beam with elastic boundary conditions, a non-homogeneous beam with delaminations and a non-uniform axially functionally graded beam with elastic boundary conditions. The governing equations of the free vibrations were derived for each model separately. The present chapter was essential for understanding the free vibration of beams and generating datasets for the inverse problems of the formulation.

## Chapter 4

# Numerical solutions using Haar wavelets

In this chapter, the non-inverse problems of various vibrating beams are solved in a novel way. The natural frequency parameters are calculated using the Haar wavelet integration. The calculated results tightly agree with the ones available in the literature. The approach can serve as a theoretical foundation for modal-based methods.

### 4.1 Literature review

One of the means to conduct the vibration based structural damage detection is to use model based methods. The damage locations and severities are revealed through the comparison of the system response obtained during the exploitation to the response of the mathematically modelled system. Such an approach is commonly used in the consistency based diagnosis [Comb 02].

The response of a mathematically modelled system can be obtained analytically or numerically. The former approach can be applied to only some simple models like uniform homogeneous beams, non-uniform beams with a few particular types of cross-section variations and some non-homogeneous beams with gradient change of the material property [Caru 09, Huan 10]. Most often the exact solutions to such problems are given in terms of special functions, such as Bessel functions [Conw 65, Nagu 94], trigonometric functions [Elis 01b], hypergeometric functions [Wang 67, Caru 09]. Largely, the limitation of the analytical approaches

is explained by the complexity of the equations of mode shapes which are linear differential with multiple coefficients.

In aeronautical and civil engineering, non-uniform non-homogeneous structures on elastic supports are frequently needed. The mode shapes of such constructions generally do not have analytical forms and, therefore, must be approximated using semi-analytical methods or numerical methods. For example, Klein [Klei 75] used the finite element method (FEM) and the Rayleigh-Ritz method to analyse behaviour of non-uniform beams. Grossi and Arenas [Gros 96] investigated tapered beams with elastically restrained ends using the Rayleigh-Ritz and the Rayleigh-Schmidt methods. Ho and Chen [Ho 98] studied the vibrations of elastically restrained non-uniform beams applying a differential transform. Hsu and Chen [Hsu 08] provided a semi-analytical solution to the free vibration of non-uniform beams with elastically end constraints utilising contemporary computational facilities. The solution was based on a modified Adomian decomposition method. Rousseau and Tippur [Rous 01], Kapuria et al. [Kapu 08], Kahya and Turan [Kahy 17] studied vertically functionally graded beams with the aid of the FEM. In practice, the application of the FEM based methods is limited if the size of the system extremely large (millions of degrees of freedom). In such cases, the simulation time on a cluster or a supercomputer can vary from hours to days or weeks [Kono 18].

In the present thesis, the transverse vibration of beams are investigated from a new angle by means of wavelets and their integration. The wavelet transform has been applied to solving differential and integral equations since the 1990s. The approach has not been widely accepted since a large number of wavelets, such as Daubechies, Symlet, Coiflet, do not have an explicit expression; therefore, an analytical differentiation or integration of such wavelets is not possible [Lepi 14]. Nevertheless, there are several wavelets which have clearly defined analytical expressions for the scaling function and the mother wavelet, for example, the Haar, Morlet, Gabor, Shannon, Legendre, Chebyshev, B-spline wavelets [Lepi 14]. These wavelets have been applied in multiple practical applications. Neild et al. [Neil 03] and Haigh et al. [Haig 02] used the harmonic wavelets for structural vibration analysis. Le [Le 17], Lardies and Gouttebroze [Lard 02] applied the Morlet wavelet for identification of modal parameters. Janeliukstis et al. [Jane 17] applied the wavelet transform to damage identification in beam structures. Mahdavi and Razak [Mahd 13] compared Chebyshev and the Haar wavelet approaches to each other in the vibration analysis of framed structures. In several papers, the wavelet-based solutions were combined with the FEM, for example, Han et al. [Han 07], Zhang et al. [Zhan 11], Yang et al. [Yang 14].

The present thesis focuses on the Haar wavelets since they are the simplest wavelets. The inspiration was found in several articles. Chen and Hsiao [Chen 97, Hsia 99] demonstrated that the Haar wavelets could successfully approximate the derivatives of functions in solving differential equations. The approach was further developed by Lepik [Lepi 05]. Hein successfully applied the Haar wavelets for elastic foundation parameter identification in delaminated beams [Hein 07]. Wang and Deng [Wang 99b] addressed a structural damage detection technique based on the Haar wavelet analysis of spatially distributed structural response. The authors stated that the technique did not require the analysis of the complete structure in question, nor any knowledge of the material properties and prior stress states of the structure. Chun and Zheng [Chun 07], and Shvartsman and Majak [Shva 16] studied axially functionally graded structures with the aid of Haar wavelets. The authors investigated simply supported rectangular plates with an arbitrary distribution of material properties in the transverse directions. In the present chapter, the Haar wavelets and their integration were applied to the calculation of dynamic response of homogeneous and non-homogeneous uniform and non-uniform intact Euler-Bernoulli beams with different boundary conditions.

## 4.2 Haar wavelet integrals

The present subsection refers to the article [Hein 11a].

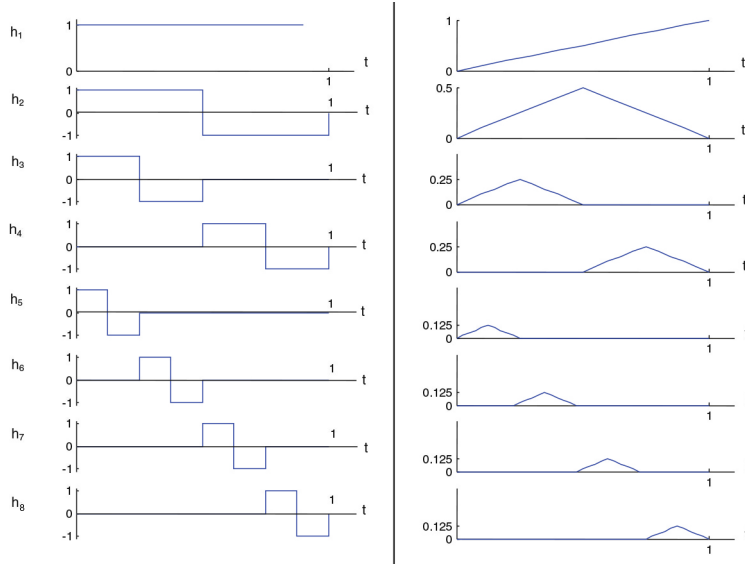
In this chapter, the free vibration of beams are solved with the aid of the Haar wavelet integration. These integrals were calculated analytically taking into account the values in each region in the range of  $[0, 1)$  [Hein 11a, Lepi 14]:

$$p_{\alpha,i}(\xi) = \underbrace{\int \dots \int}_{\alpha \text{-times}} h_i(\xi) d\xi^\alpha = \begin{cases} 0 & \text{for } \xi < \xi^{(1)}, \\ \frac{1}{\alpha!}(\xi - \xi^{(1)})^\alpha & \text{for } \xi \in [\xi^{(1)}, \xi^{(2)}), \\ \frac{1}{\alpha!}[(\xi - \xi^{(1)})^\alpha - 2(\xi - \xi^{(2)})^\alpha] & \text{for } \xi \in [\xi^{(2)}, \xi^{(3)}), \\ \frac{1}{\alpha!}[(\xi - \xi^{(1)})^\alpha - 2(\xi - \xi^{(2)})^\alpha + (\xi - \xi^{(3)})^\alpha] & \text{for } \xi > \xi^{(3)}, \end{cases} \quad (4.1)$$

where  $\xi^{(1)}$ ,  $\xi^{(2)}$  and  $\xi^{(3)}$  are defined in (2.4),  $\alpha$  is the order of integration,  $i$  is the number of the wavelet. Equation (4.1) is valid for  $i > 1$ . In case of  $i = 1$  and  $\xi^{(1)} = 0$ ,  $\xi^{(2)} = \xi^{(3)} = 1$  and the integral of the wavelet  $h_1(\xi)$ , the equation is

$$p_{\alpha,1}(\xi) = \frac{1}{\alpha!} \xi^\alpha. \quad (4.2)$$

Figure 4.1 [Kalp 07] shows the Haar scaling function  $h_1(\xi)$ , the Haar wavelets ( $i = 2, \dots, 8$ ) and their integrals.



**Figure 4.1:** The Haar wavelets: scaling function ( $i = 1$ ), the wavelets of resolution  $J = 0, 1, 2$  (left), and the corresponding integrals of the wavelets (right).

Evaluating the integrals of (4.1) in the collocation points, a  $2M \times 2M$  matrix  $P^{(\alpha)}$  is obtained

$$P^{(\alpha)}(i, l) = p_{\alpha,i}(\xi_l). \quad (4.3)$$

In the vibration problems, the boundary conditions are essential; therefore, the values at the ends of the beam  $p_{\alpha,i}(0)$  and  $p_{\alpha,i}(1)$  are calculated and presented as  $2M$  dimensional vectors.

The advantage of the integration consists in the fact that the calculation of matrices  $H(i, l)$  and  $P^{(\alpha)}(i, l)$  is carried out only once.



### 4.2.1 Haar wavelet method for solving free vibration problems

The Haar wavelet integrals were applied to the mathematical models described in Subsections 3.2.1 and 3.2.3. The fourth derivative of (3.44) was sought in the simplest approximation form:

$$W^{IV}(\xi) = \frac{d^4 y(\xi)}{d\xi^4} = \sum_{i=1}^{2M} c_i h_i(\xi), \quad (4.4)$$

where  $c_i$  are the unknown wavelet coefficients and  $\xi = x/L$ . Integrating (4.4) four times, the following equations are obtained

$$\begin{aligned} W''''(\xi) &= \sum_{i=1}^{2M} c_i p_{1,i}(\xi) + W''''(0), \\ W''(\xi) &= \sum_{i=1}^{2M} c_i p_{2,i}(\xi) + W''''(0)\xi + W''(0), \\ W'(\xi) &= \sum_{i=1}^{2M} c_i p_{3,i}(\xi) + \frac{1}{2}W''''(0)\xi^2 + W''(0)\xi + W'(0), \\ W(\xi) &= \sum_{i=1}^{2M} c_i p_{4,i}(\xi) + \frac{1}{6}W''''(0)\xi^3 + \frac{1}{2}W''(0)\xi^2 + W'(0)\xi + W(0), \end{aligned} \quad (4.5)$$

where  $p_{1,i}$ ,  $p_{2,i}$ ,  $p_{3,i}$ ,  $p_{4,i}$  are obtained from (4.1). In (4.5), the constants of the integration  $W(0)$ ,  $W'(0)$ ,  $W''(0)$ ,  $W''''(0)$  can be evaluated from the boundary conditions. Some examples, used in the following subsections of this chapter, are described below.

(i) Cantilever beams (clamped-free or CF)

One end of the beam ( $\xi = 0$ ) is clamped, while the other end ( $\xi = 1$ ) is free. Hence, the boundary conditions for the cantilever are  $W(0) = W'(0) = 0$  and  $W''(1) = W''''(1) = 0$ . The system of equations is derived from (4.5):

$$\begin{aligned} W''''(1) &= \sum_{i=1}^{2M} c_i p_{1,i}(1) + W''''(0) = 0, \\ W''(1) &= \sum_{i=1}^{2M} c_i p_{2,i}(1) + W''''(0) + W''(0) = 0. \end{aligned} \quad (4.6)$$

From (4.6),  $W''(0)$  and  $W''''(0)$  are obtained as follows:

$$\begin{aligned}
W''(0) &= \sum_{i=1}^{2M} c_i q_{1,i}, \\
W'''(0) &= - \sum_{i=1}^{2M} c_i p_{1,i}(1),
\end{aligned} \tag{4.7}$$

where  $q_{1,i} = p_{1,i}(1) - p_{2,i}(1)$ . According to (4.5), the mode shape  $W(\xi)$  is described by the following equation:

$$W(\xi) = \sum_{i=1}^{2M} c_i \left[ p_{4,i}(\xi) - \frac{1}{6} p_{1,i}(1) \xi^3 + \frac{1}{2} q_{1,i} \xi^2 \right]. \tag{4.8}$$

(ii) Simply supported beams (SS)

In the simply supported beam, the boundary conditions are  $W(0) = W''(0) = 0$  and  $W(1) = W''(1) = 0$ . The system of equations is as follows:

$$\begin{aligned}
\sum_{i=1}^{2M} c_i p_{2,i}(1) + W'''(0) &= 0, \\
\sum_{i=1}^{2M} c_i p_{4,i}(1) + \frac{1}{6} W'''(0) + W'(0) &= 0.
\end{aligned} \tag{4.9}$$

From (4.9), the following equations are obtained:

$$\begin{aligned}
W'''(0) &= - \sum_{i=1}^{2M} c_i p_{2,i}(1), \\
W'(0) &= \frac{1}{6} \sum_{i=1}^{2M} c_i q_{2,i},
\end{aligned} \tag{4.10}$$

where  $q_{2,i} = p_{2,i}(1) - 6p_{4,i}(1)$ . The equation of the mode shape takes the form of:

$$W(\xi) = \sum_{i=1}^{2M} c_i \left[ p_{4,i}(\xi) - \frac{1}{6} p_{2,i}(1) \xi^3 + \frac{1}{6} q_{2,i} \xi \right]. \tag{4.11}$$

(iii) Clamped beams (CC)

The boundary conditions for the clamped beam are  $W(0) = W'(0) = 0$  and  $W(1) = W'(1) = 0$ . The system of equations is as follows:

$$\begin{aligned}
W'''(0) &= 6 \sum_{i=1}^{2M} c_i q_{3,i}, \\
W''(0) &= \sum_{i=1}^{2M} c_i q_{4,i},
\end{aligned} \tag{4.12}$$

where  $q_{3,i} = 2p_{4,i}(1) - p_{3,i}(1)$  and  $q_{4,i} = 2p_{3,i}(1) - 6p_{4,i}(1)$ . The mode shape is described by the equation as follows:

$$W(\xi) = \sum_{i=1}^{2M} c_i \left[ p_{4,i}(\xi) + q_{3,i}\xi^3 + \frac{1}{2}q_{4,i}\xi^2 \right]. \tag{4.13}$$

(iv) Clamped - pinned beams (CP)

One end of the beam ( $\xi = 0$ ) is fixed and the other end ( $\xi = 1$ ) is simply supported. Thus, the corresponding boundary conditions are  $W(0) = W'(0) = 0$  and  $W(1) = W''(1) = 0$ . From (4.5), the following system of equations is obtained

$$\begin{aligned}
W'''(0) &= \sum_{i=1}^{2M} c_i q_{5,i}, \\
W''(0) &= \sum_{i=1}^{2M} c_i q_{6,i},
\end{aligned} \tag{4.14}$$

where  $q_{5,i} = 3p_{4,i}(1) - \frac{3}{2}p_{2,i}(1)$  and  $q_{6,i} = -q_{5,i} - p_{2,i}(1)$ . The mode shape is described as follows:

$$W(\xi) = \sum_{i=1}^{2M} c_i \left[ p_{4,i}(\xi) + \frac{1}{6}q_{5,i}\xi^3 + \frac{1}{2}q_{6,i}\xi^2 \right]. \tag{4.15}$$

(v) Elastic supports for a tapered beam described in Subsection 3.2.1

It is assumed that the elasticity modulus  $E$  is constant, but the cross-section and the second moment of area vary along the longitudinal axis ( $A = A(\xi)$  and  $I = I(\xi)$ ). The boundary conditions for the beam on elastic supports (translational and rotational springs with the stiffness coefficients  $K_{TL}$  and  $K_{RL}$  at the left end of the beam; translational and rotational springs with the stiffness coefficients  $K_{TR}$  and  $K_{RR}$  at the right end of the beam) are described in (3.32). These are rewritten

for the left and right ends of the tapered beam as follows:

$$[I(\xi)W''(\xi)]' + k_{tl}W(\xi) = 0, \quad (4.16)$$

$$I(\xi)W''(\xi) - k_{rl}W'(\xi) = 0, \quad (4.17)$$

$$[I(\xi)W''(\xi)]' - k_{tr}W(\xi) = 0, \quad (4.18)$$

$$I(\xi)W''(\xi) + k_{rr}W'(\xi) = 0, \quad (4.19)$$

where

$$k_{tl} = \frac{K_{TL}L^3}{E}, k_{rl} = \frac{K_{RL}L}{E}, k_{tr} = \frac{K_{TR}L^3}{E}, k_{rr} = \frac{K_{RR}L}{E}. \quad (4.20)$$

Taking into account (4.5) and the coordinate at the left end ( $\xi = 0$ ), equations (4.16) and (4.17) take the form of

$$I'(0)W''(0) + I(0)W'''(0) + k_{tl}W(0) = 0, \quad (4.21)$$

$$I(0)W''(0) - k_{rl}W'(0) = 0. \quad (4.22)$$

Taking into account (4.5) and the coordinate at the right end ( $\xi = 1$ ), equations (4.18) and (4.19) take the form of

$$\begin{aligned} I'(1) \left[ \sum_{i=1}^{2M} c_i p_{2,i}(1) + W'''(0) + W''(0) \right] + I(1) \left[ \sum_{i=1}^{2M} c_i p_{1,i}(1) + W'''(0) \right] - \\ - k_{tr} \left[ \sum_{i=1}^{2M} c_i p_{4,i}(1) + \frac{1}{6}W'''(0) + \frac{1}{2}W''(0) + W'(0) + W(0) \right] = 0, \quad (4.23) \end{aligned}$$

$$\begin{aligned} I(1) \left[ \sum_{i=1}^{2M} c_i p_{2,i}(1) + W'''(0) + W''(0) \right] + \\ + k_{rr} \left[ \sum_{i=1}^{2M} c_i p_{3,i}(1) + \frac{1}{2}W'''(0) + W''(0) + W'(0) \right] = 0. \quad (4.24) \end{aligned}$$

The system of (4.21), (4.22), (4.23) and (4.24) is linear; hence,  $W(0)$ ,  $W'(0)$ ,  $W''(0)$  and  $W'''(0)$  can be found.

Once the governing equation for a uniform beam (3.13), a non-uniform beam (3.31) or a non-homogeneous tapered beam (3.44) and the boundary conditions are determined in the analytical form, the governing equation can be presented as a matrix equation:

$$cR = 0. \quad (4.25)$$

In case of a cantilever, the governing equation (3.44) is presented by the Haar wavelets and their integrals by substituting (4.4) - (4.8) into (3.44), taking into account (4.25) and discretising the results. The matrix  $R$  takes the form:

$$R = B_1^T U H + B_2^T U \left[ P^{(1)} - P^{(1)}(1)U \right] + B_3^T U \left[ P^{(2)} - P^{(1)}(1)(\xi) + q_1(\xi)^2 \right] - k^4 B_4^T U \left[ P^{(4)} - \frac{1}{6}P^{(1)}(1)(\xi)^3 \right], \quad (4.26)$$

where  $P^{(\alpha)}(1) = p_{\alpha,i}(1)$ ,  $q_1 = P^{(1)}(1) - P^{(2)}(1)$ ,  $(\xi) = (\xi_1 \dots \xi_{2M})$  and  $(\xi)^n$  denotes the elementwise multiplication of coordinates.  $U$  is a unit row vector (used to put the matrices into the same dimension),  $k$  is the natural frequency parameter, which is determined as  $k = k_* L$  and  $k_*$  is determined in (3.42), and

$$\begin{aligned} B_1 &= E(\xi)I(\xi), \\ B_2 &= E'(\xi)I(\xi) + E(\xi)I'(\xi), \\ B_3 &= E''(\xi)I(\xi) + 2E'(\xi)I'(\xi) + E(\xi)I''(\xi), \\ B_4 &= \rho(\xi)A(\xi), \end{aligned} \quad (4.27)$$

are row vectors evaluated at  $\xi = \xi_l$  ( $l = 1, \dots, 2M$ ) and element-wise multiplication is applied at the right side. For (3.13) and (3.31), the matrix equations can be derived analogically.

The system (4.26) is linear and homogeneous with regard to the coefficients  $c_i$ , and it contains the natural frequency parameter. The natural frequency can be calculated as follows:

$$\omega = k^2 \sqrt{\frac{E_0 I_0}{\rho_0 A_0}} L^4. \quad (4.28)$$

To derive a non-trivial solution, the determinant of the system must be zero. According to this requirement, the values of the natural frequency parameters can be evaluated.

## 4.3 Numerical examples

### 4.3.1 Uniform homogeneous beams

The mathematical model of a homogeneous cantilever with a uniform cross-section is described in Subsection 3.1.1. In such a beam, the bending stiffness and mass are constants. Using (3.13), (4.4) and (4.8), introducing the dimensionless longitudinal coordinate  $\xi = x/L$  and applying the method of determinants, the dimensionless natural frequency parameters (DFPs) are computed ( $k_n = L\sqrt{\omega_n\sqrt{\frac{\rho A}{EI}}}$ ,  $n = 1, \dots, 5$ ). The results for different levels of resolution  $J$  are shown in Table 4.1. For reference, the table also contains the results obtained with the aid of the initial parameters method by Karnovsky [Karn 01]. The results are compared on the mean square error (MSE) given in 2.14 and the relative error (RE):

$$RE = \frac{1}{N} \sum_{n=1}^N \left| 1 - \frac{y_c}{y_t} \right| 100\%, \quad (4.29)$$

where  $y_t$  is the target value and  $y_c$  is the computed value.

**Table 4.1:** The first five  $k_n$  for the uniform cantilever.

$n$	[Karn 01, p.142]	$J = 2$	$J = 3$	$J = 4$	$J = 5$	$J = 6$
1	1.8751	1.8783	1.8759	1.8753	1.8752	<b>1.8752</b>
2	4.6941	4.7342	4.7040	4.6966	4.6948	<b>4.6943</b>
3	7.8548	7.9991	7.8899	7.8635	7.8570	<b>7.8554</b>
4	10.9956	11.3505	11.0805	11.0166	11.0008	<b>10.9969</b>
5	14.1372	14.8408	14.3045	14.1784	14.1475	<b>14.1398</b>
MSE		0.1287	0.0073	0.0004	0.0000	0.0000
RE (%)		2.2133	0.5312	0.1314	0.0337	0.0095

In Table 4.1, it is seen that a higher wavenumber  $n$  in  $k_n$  requires a higher resolution for a more accurate result. Nevertheless, the presented approach allows reaching high accuracy using relatively a small number of the collocation points.

### 4.3.2 Homogeneous beams with non-uniform cross-section

The proposed approach of the Haar wavelet discrete transform and integration (HWTI) is applied to a wedge beam with a rectangular cross-section and clamped-free ends with the aim to calculate the DFPs. The corresponding mathematical model is described in Subsection 3.2.1. Specifically, the shape of the beam, the

breadth and the height of the beam can be described by the formulae [Hsu 08]:

$$h(\xi) = h_0 [1 + (\beta_h - 1)\xi], \quad (4.30)$$

$$b(\xi) = b_0 [1 + (\beta_b - 1)\xi], \quad (4.31)$$

where  $b_0 = b(0)$ ,  $h_0 = h(0)$  and  $\beta_b$  stand for the ratio between the breadths at the beginning and at the end of the beam;  $\beta_h$  is the ratio between the heights, respectively. Hence, the area and the moment of inertia take the following form:

$$A(x) = b_0 h_0 [1 + (\beta_b - 1)\xi] [1 + (\beta_h - 1)\xi], \quad (4.32)$$

$$I(x) = \frac{b_0 h_0^3}{12} [1 + (\beta_b - 1)\xi] [1 + (\beta_h - 1)\xi]^3. \quad (4.33)$$

For (3.31), the first and the second derivatives of  $I(x)$  are needed:

$$I'(\xi) = \{(\beta_b - 1)[1 + (\beta_h - 1)\xi]^3 + 3[1 + (\beta_b - 1)\xi][1 + (\beta_h - 1)\xi]^2(\beta_h - 1)\} \frac{b_0 h_0^3}{12}, \quad (4.34)$$

$$I''(\xi) = \frac{b_0 h_0^3}{2} (\beta_h - 1)[1 + (\beta_h - 1)\xi] \{(\beta_b - 1)[1 + (\beta_h - 1)\xi] + (\beta_h - 1)[1 + (\beta_b - 1)\xi]\}. \quad (4.35)$$

The DFPs are calculated by substituting (4.32) - (4.35) into (3.31), using (4.4) and (4.5).

In Table 4.2, the first two squared DFPs ( $k_n^2 = \omega_n L^2 \sqrt{\frac{\rho_0 A_0}{E_0 I_0}}$ ,  $n = 1, 2$ ) are presented for the clamped-free wedge beam ( $\beta_b = 1$ ,  $\beta_h = \beta$ ,  $A_0 = A(0)$ ,  $\rho_0 = \rho(0)$ ,  $n = 1, 2$ ) (here and in the following tables the choice of the varying parameters was motivated by the reference calculations available in literature). In Table 4.3, the first two squared DFPs ( $k_n^2$ ,  $n = 1, 2$ ) are presented for the truncated cone beam ( $\beta_b = \beta_h = \beta$ ). Taking into account the results of the previous example (Subsection 4.3.1), the level of resolution is set to  $J = 5$  and  $J = 6$ . The DFPs are squared to make the comparison with the calculations carried out by Hsu [Hsu 08] who in turns compared the results with Naguleswaran [Nagu 94]. According to the results, the HWTI approach works accurately with an insignificant error.

**Table 4.2:** The first two  $k_n^2$  for the wedge cantilever ( $\beta_b = 1, \beta_h = \beta$ ).

$\beta$	$n = 1$			$n = 2$		
	[Hsu 08]	HWTI J = 5	HWTI J = 6	[Hsu 08]	HWTI J = 5	HWTI J = 6
	0.1	4.6307	4.6305	<b>4.6307</b>	14.9308	14.9248
0.2	4.2925	4.2922	<b>4.2924</b>	15.7427	15.7408	<b>15.7422</b>
0.3	4.0817	4.0816	<b>4.0817</b>	16.6252	16.6263	<b>16.6255</b>
0.4	3.9343	3.9343	<b>3.9343</b>	17.4879	17.4908	<b>17.4886</b>
0.5	3.8238	3.8239	<b>3.8238</b>	18.3173	18.3215	<b>18.3183</b>
0.6	3.7371	3.7373	<b>3.7371</b>	19.1138	19.1190	<b>19.1151</b>
0.7	3.6667	3.6670	<b>3.6668</b>	19.8806	19.8863	<b>19.8820</b>
MSE		0.0000	0.0000		0.0000	0.0000
RE (%)		0.0043	0.0011		0.0220	0.0055

**Table 4.3:** The first two  $k_n^2$  for the cone cantilever ( $\beta_b = \beta_h = \beta$ ).

$\beta$	$n = 1$			$n = 2$		
	[Hsu 08]	HWTI J = 5	HWTI J = 6	[Hsu 08]	HWTI J = 5	HWTI J = 6
	0.1	7.2049	7.2055	<b>7.2050</b>	18.6802	18.6763
0.2	6.1964	6.1962	<b>6.1963</b>	18.3855	18.3798	<b>18.3840</b>
0.3	5.5093	5.5089	<b>5.5092</b>	18.6412	18.6385	<b>18.6405</b>
0.4	5.0090	5.0088	<b>5.0090</b>	19.0649	19.0651	<b>19.0649</b>
0.5	4.6252	4.6251	<b>4.6251</b>	19.5476	19.5501	<b>19.5482</b>
0.6	4.3188	4.3189	<b>4.3188</b>	20.0500	20.0541	<b>20.0510</b>
0.7	4.0669	4.0671	<b>4.0670</b>	20.5554	20.5607	<b>20.5568</b>
MSE		0.0000	0.0000		0.0000	0.0000
RE (%)		0.0044	0.0012		0.0182	0.0046

Next, the boundary conditions of the cone have been changed from the classical ones for the equally varying translational spring constraints on the left and right ends of the beam ( $k_{tl} = k_{tr}$ , whereas  $k_{rl} = k_{rr} = 0$ ). The first two DFPs ( $k_n$ ,  $n = 1, 2$ ) of the vibrating cone with breadth and height ratios  $\beta_b = \beta_h = 1.4$  are calculated substituting (4.32) - (4.34) into (4.21) - (4.24), and applying the procedure described in Subsection 4.2.1. The calculations are carried out for  $J = 5$ . The results are presented in Table 4.4. For reference, the table also contains the results obtained by Hsu in [Hsu 08]. The insignificant relative error in the computations of the DFPs shows that the provided method of the HWTI is capable of calculating different frequencies for both small and large translational springs.

Although the results in Table 4.4 are precise, an attempt to improve the accuracy for  $k_3$  has been done on the account of resolution  $J$ . For the calculation of the third DFPs ( $k_3$ ), the resolution  $J$  has been increased from five to seven (the model and the conditions of the cone have been remained unchanged). The results are presented in Table 4.5. The accuracy of the calculations has been improved



**Table 4.4:** The first two  $k_n$  for the cone ( $\beta_b = \beta_h = 1.4$ ) with equally varying translational spring constraints on the left and right ends ( $k_{tl} = k_{tr}$ ), whereas  $k_{rl} = k_{rr} = 0$ ;  $J = 5$ .

$k_{tl} = k_{tr}$	$n = 1$		$n = 2$	
	[Hsu 08]	HWTI	[Hsu 08]	HWTI
0.001	0.21656	0.2166	0.31795	0.3180
0.01	0.38510	0.3851	0.5639	0.5654
0.1	0.68462	0.6846	1.00528	1.0053
1	1.21404	1.2140	1.78509	1.7851
10	2.10096	2.1009	3.13023	3.1303
100	3.07241	3.0723	5.06670	5.0668
1000	3.37553	3.3754	6.56963	6.5697
MSE		0.0000		0.0000
RE (%)		0.0015		0.0036

with the increase of the resolution. Nonetheless, it can be so only to a certain extent of the resolution: with the growth of the resolution, the values in matrices become indefinitely small and the calculations become inaccurate [Lepi 05].

**Table 4.5:** The third DFPs ( $k_3$ ) for the cone ( $\beta_b = \beta_h = 1.4$ ) with varying translational spring constraints on the left and right ends ( $k_{tl} = k_{tr}$ ), whereas  $k_{rl} = k_{rr} = 0$ ;  $J = 5, 6, 7$ .

$k_{tl} = k_{tr}$	[Hsu 08]	HWTI	HWTI	HWTI
		J = 5	J = 6	J = 7
0.001	5.19178	5.1927	5.1920	<b>5.1918</b>
0.01	5.19196	5.1929	5.1922	<b>5.1920</b>
0.1	5.19381	5.1948	5.1940	<b>5.1939</b>
1	5.21223	5.2132	5.2125	<b>5.2123</b>
10	5.39376	5.3948	5.3940	<b>5.3938</b>
100	6.71152	6.7125	6.7118	<b>6.7116</b>
1000	9.28876	9.2894	9.2889	<b>9.2888</b>
MSE		0.0000	0.0000	0.0000
RE (%)		0.0163	0.0040	0.0009

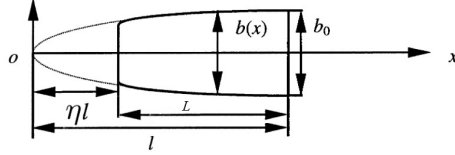
Next, a truncated tapered beam with a continuously varying cross-section is considered

$$\begin{aligned} b(\xi) &= b_0\sqrt{\xi}, \\ h(\xi) &= h_0\xi, \end{aligned} \tag{4.36}$$

where  $b_0$  and  $h_0$  are the breadth and depth of the beam at the right end  $\xi = 1$  ( $\xi = x/l$ ). In other words, the beam has a parabolic-taper width and a linear-taper height. The truncation factor  $\eta$  ( $0 \leq \eta < 1$ ) describes the beam at one end; the length of the truncated tapered beam is evaluated as follows:

$$L = (1 - \eta)l, \tag{4.37}$$

where  $l$  is the length of the sharp ended beam ( $\eta = 0$ ) and  $L$  is the length of the truncated tapered beam (without the part at the sharp end) (Figure 4.2 [Zhou 00]). In the present example, the truncated tapered beam is clamped at  $\xi = 1$  and free at  $\xi = \eta$ .



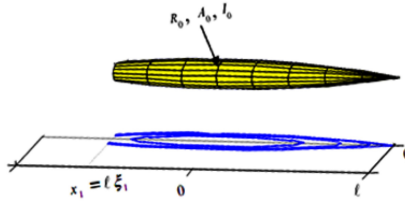
**Figure 4.2:** A truncated beam with a parabolic-taper width.

The first three DFPs ( $k_n^2$ ,  $n = 1, \dots, 3$ ) for the truncated beam ( $\eta$  varied from 0.1 to 0.8 with 0.1 increment) are calculated and presented in Table 4.6. The accuracy of the HWTI method is assured from the comparison study with [Zhou 00]: the relative error is small (less than one per cent).

**Table 4.6:** The first three  $k_n^2$  for the tapered cantilever with a parabolic-taper width, a linear-taper height and truncate factor  $\eta$ .

	$\eta$	$n = 1$		$n = 2$		$n = 3$	
		[Zhou 00]	HWTI	[Zhou 00]	HWTI	[Zhou 00]	HWTI
J = 5	0.1	5.8382	5.8383	16.696	16.6901	34.854	34.8190
	0.2	5.1971	5.1867	17.005	17.0005	38.293	38.2848
	0.3	4.7577	4.7574	17.600	17.5988	41.660	41.6669
	0.4	4.4478	4.4477	18.257	18.2587	44.857	44.8742
	0.5	4.2100	4.2101	18.922	18.9250	47.907	47.9306
	0.6	4.0198	4.0199	19.576	19.5807	50.836	50.8638
	0.7	3.8628	3.8630	20.215	20.2207	53.664	53.6955
	0.8	3.7301	3.7303	20.838	20.8437	56.453	56.4426
		MSE		0.0000		0.0000	
	RE (%)		0.0252		0.0288		0.0757
J = 6	MSE		0.0000		0.0000		0.0001
	RE (%)		0.0235		0.0049		0.0169
J = 7	MSE		0.0000		0.0000		0.0001
	RE (%)		0.0232		0.0029		0.0148

Finally, the HWTI approach has been examined on the tapered cantilever with parabolic thickness ( $h(\xi) = h_0(1 - \xi^2)$ ) and a circular cross-section (Figure 4.3 [Caru 09]).



**Figure 4.3:** A parabolic cantilever with parabolic thickness  $h(\xi) = h_0(1 - \xi^2)$  and a circular cross-section.

In such a case, the cross-section area  $A$ , the moment of inertia  $I$  and the parabolic radius variation  $R$  are described by the formulae [Caru 09]:

$$\begin{aligned} R(\xi) &= R_0(1 - \xi^2), \\ A(\xi) &= \pi R_0^2(1 - \xi^2)^2, \\ I(\xi) &= \frac{\pi R_0^4}{4}(1 - \xi^2)^4, \end{aligned} \quad (4.38)$$

where  $R_0$  is the reference radius at  $\xi = 0$  regardless where the fixed end ( $\xi = \xi_1$ ) of the cantilever is.

The results of the calculations of the first two squared DFPs ( $k_n^2$ ,  $n = 1, 2$ ) and the comparison are provided in Table 4.7. The calculated results correspond to Caruntu's research [Caru 09] in which the author used an analytical approach in terms of hypergeometric functions. The relative error is less than one per cent.

**Table 4.7:** The first two  $k_n^2$  of the cantilever with a circular cross-section and parabolic thickness  $h(\xi) = h_0(1 - \xi^2)$  versus the dimensionless coordinate of the fixed end.

$\xi_1$	$n = 1$			$n = 2$		
	[Caru 09]	HWTI J = 5	HWTI J = 6	[Caru 09]	HWTI J = 5	HWTI J = 6
-0.7	1.011	1.0028	<b>1.0087</b>	8.727	8.7001	<b>8.7201</b>
-0.6	1.572	1.5682	<b>1.5711</b>	10.57	10.5539	<b>10.5632</b>
-0.5	2.238	2.2357	<b>2.2371</b>	12.55	12.5449	<b>12.5492</b>
-0.4	3.020	3.0192	<b>3.0198</b>	14.75	14.7451	<b>14.7470</b>
-0.3	3.940	3.9394	<b>3.9397</b>	17.23	17.2265	<b>17.2273</b>
-0.2	5.026	5.0263	<b>5.0264</b>	20.07	20.0747	<b>20.0748</b>
-0.1	6.322	<b>6.3217</b>	6.3217	23.40	23.4001	<b>23.3999</b>
0	7.886	<b>7.8857</b>	7.8857	27.35	27.3542	<b>27.3538</b>
0.1	9.805	<b>9.8053</b>	9.8053	32.15	32.1529	<b>32.1523</b>
0.2	12.21	<b>12.2122</b>	12.2122	38.12	38.1183	<b>38.1174</b>
0.3	15.31	<b>15.3134</b>	15.3134	45.75	45.7554	<b>45.7539</b>
0.4	19.45	<b>19.4545</b>	19.4545	55.90	55.9045	<b>55.9019</b>
0.5	25.26	<b>25.2580</b>	25.2580	70.07	70.0771	<b>70.0728</b>
0.6	33.97	<b>33.9693</b>	33.9692	91.29	91.2953	<b>91.2880</b>
0.7	48.49	<b>48.4945</b>	48.4945	126.6	126.6097	<b>126.5970</b>
MSE		0.0000	0.0000		0.0001	0.0000
RE (%)		0.0859	0.0292		0.0434	0.0172

### 4.3.3 Uniform axially functionally graded beams

In this subsection, a uniform beam with a rectangular cross-section is considered. The flexural rigidity and mass density are variable along the longitudinal axis. The governing equation of the transverse vibration of the axially functionally graded beam (AFG) take the form:

$$E(\xi)W^{IV}(\xi) + 2E'(\xi)W'''(\xi) + E''(\xi)W''(\xi) - k^4m(\xi)W(\xi) = 0. \quad (4.39)$$

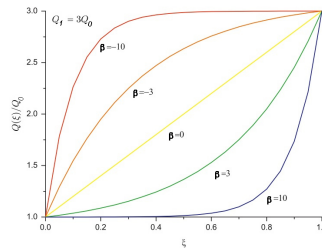
The material properties  $Q(\xi)$  (Young's modulus, the mass density) of the AFG beam vary as follows [Huan 10]:

$$Q(\xi) = \begin{cases} Q_0(1 - \frac{e^{\beta\xi}-1}{e^\beta-1}) + Q_1 \frac{e^{\beta\xi}-1}{e^\beta-1}, & \beta \neq 0, \\ Q_0(1 - \xi) + Q_1\xi, & \beta = 0, \end{cases} \quad (4.40)$$

where  $Q_0, Q_1$  are the property values at the ends of the beam ( $\xi = 0, \xi = 1$ );  $\beta$  is the gradient parameter which describes the volume fraction change of two components in the material. The chosen components are aluminium and zirconia with the following properties [Huan 10]:

- $Al : E_0 = 70GPa, \rho_0 = 2702kg/m^3,$
- $ZrO_2 : E_1 = 200GPa, \rho_1 = 5700kg/m^3.$

The material property change along the axis is shown in Figure 4.4 ( $\xi = 0$  is an aluminium-rich end and  $\xi = 1$  is a zirconia-rich end) [Huan 10].



**Figure 4.4:** Variation of the graded material properties.

The first DFPs ( $k_1^2$ ) for the AFG beams with simply supported ends (S-S), clamped ends (C-C) and clamped-pinned ends (C-P) are calculated and presented in Table 4.8. The results are compared with the calculations conducted by Huang and Li [Huan 10]. The relative error is less than one per cent.

**Table 4.8:** The first  $k_1^2$  of the axially functionally graded beam (aluminium-zirconia) versus the material gradient parameter  $\beta$ ;  $J = 5$ .

	$\beta$	S-S		C-C		C-P	
		[Huan 10]	HWTI	[Huan 10]	HWTI	[Huan 10]	HWTI
J = 5	-10	11.4532	11.4481	24.0576	24.0269	16.4775	16.3837
	-3	11.2443	11.2422	23.9456	23.9384	16.0219	16.0307
	0	10.8663	10.8660	24.3752	24.3749	15.8734	15.8729
	3	10.3669	10.3670	24.9375	24.9371	15.7171	15.7171
	10	9.9358	9.9366	24.7949	24.8080	15.4956	15.4930
	MSE		0.0000		0.0002		0.0018
	RE (%)		0.0149		0.0428		0.1288
J = 6	MSE		0.0000		0.0001		0.0013
	RE (%)		0.0039		0.0224		0.1082

#### 4.3.4 Non-uniform axially functionally graded beams

In the present subsection, AFG beams on elastic supports are considered. The flexural rigidity and mass density of the beam vary in the following form:

$$\begin{aligned} D(\xi) &= D_0 [1 + \alpha \cos(\pi\xi)], \\ \rho(\xi) &= \rho_0 [1 + \beta \cos(\pi\xi)], \end{aligned} \quad (4.41)$$

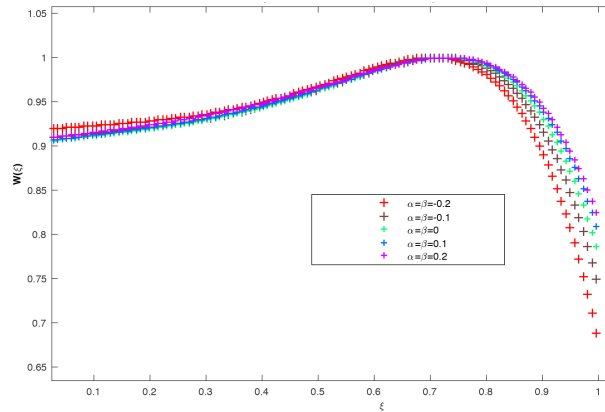
where  $|\alpha| < 1$  and  $|\beta| < 1$  are the parameters. The conditions insure that  $D(\xi)$  and  $\rho(\xi)$  are positive. In the present model, the ends of the beam are fixed by elastic spring supports described in (3.45).

In Table 4.9, the first DFPs ( $k_1^2$ ) are tabulated for the beam with a varying bending stiffness coefficient, fixed stiffness coefficients of the translational and rotational springs at the right end ( $k_{tr} = k_{rr} = 1$ ) and varying stiffness coefficients of the translational and rotational springs at the left end ( $k_{tl} = k_{rl}$ ).

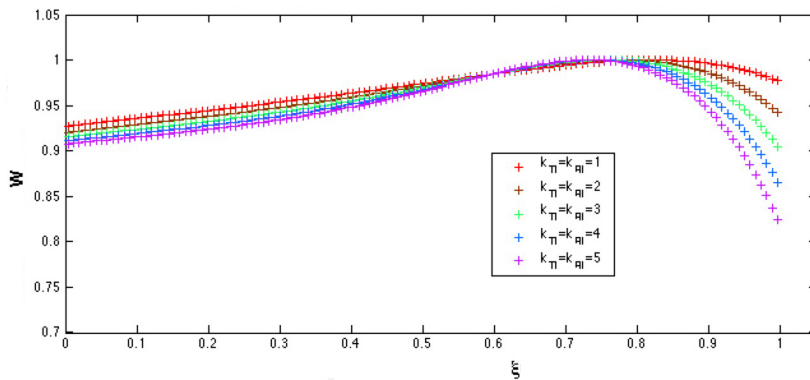
**Table 4.9:** The first  $k_1^2$  for the beams with varying left-side elastic constraints ( $k_{tl} = k_{rl}$ ); the supports at the right end are fixed ( $k_{tr} = k_{rr} = 1$ ); the beam properties are  $\alpha = \beta$ ;  $J = 6$ .

$\alpha = \beta$	$k_{tl} = k_{rl}$				
	1.0	2.0	3.0	4.0	5.0
-0.2	1.4407	2.0732	2.5756	3.0206	3.4419
-0.1	1.3866	1.9939	2.4705	2.8855	3.2678
0	1.3439	1.9325	2.3912	2.7868	3.1460
0.1	1.3096	1.8839	2.3292	2.7110	3.0551
0.2	1.2818	1.8446	2.2795	2.6510	2.9843

In Figure 4.5, the first mode shapes with respect to maximum value of the AFG Euler-Bernoulli beams with varying flexural rigidity and mass density (4.41) are shown; the elastic supports at the ends of the beam are  $k_{tl} = k_{rl} = 5, k_{tr} = k_{rr} = 1$ . The normalised first mode shapes for the AFG beams with varying left-side elastic constraints ( $k_{tl}, k_{rl}$ ) are shown in Figure 4.6: the elastic supports at the right end are fixed to the value  $k_{tr} = k_{rr} = 1$ , the parameters are  $\alpha = \beta$ ; the flexural rigidity  $D(\xi)$  is set to 0.2. The calculation have been carried out using the HWTI method at the resolution level  $J = 6$ .



**Figure 4.5:** Normalised first mode shapes of the AFG Euler-Bernoulli beam with varying flexural rigidity and mass density.



**Figure 4.6:** Normalised first mode shapes of the AFG Euler-Bernoulli beam with different elastic supports at the left end  $k_{tl} = k_{rl}$ , at the right end  $k_{tr} = k_{rr} = 1$  and flexural rigidity  $D(\xi) = 0.2$ .

Finally, the HWTI method is applied to the AFG beams with elastic supports at the ends and an additional intermediate rigid support at  $\xi = \gamma$ . The varying flexural rigidity and mass density of the AFG beam are described in (4.41). The boundary conditions at the ends of the beam are described in Subsection 3.45. Apart from two conditions on each end of the beam, an additional condition for the intermediate support is as follows:

$$W(\gamma) = 0. \quad (4.42)$$

Using (4.5), (4.42) is rewritten for the vertical displacement  $W(\gamma)$ :

$$W(\gamma) = \sum_{i=1}^{2M} c_i \left[ p_{4,i}(\gamma) + \frac{1}{6}q_{5,i}\gamma^3 + \frac{1}{2}q_{6,i}\gamma^2 \right]. \quad (4.43)$$

In Table 4.10, the calculated first DFPs ( $k_1^2$ ) for the fixed stiffness coefficients of the translational and rotational springs  $k_{rr} = k_{tr} = k_{rl} = k_{tl} = 1$ , varying  $\alpha = \beta$  and different values of  $\gamma$  are tabulated. It can be seen that in the case of symmetric boundary conditions, the DFPs are not the same. This is explained by the non-symmetric AFG material of the beam.

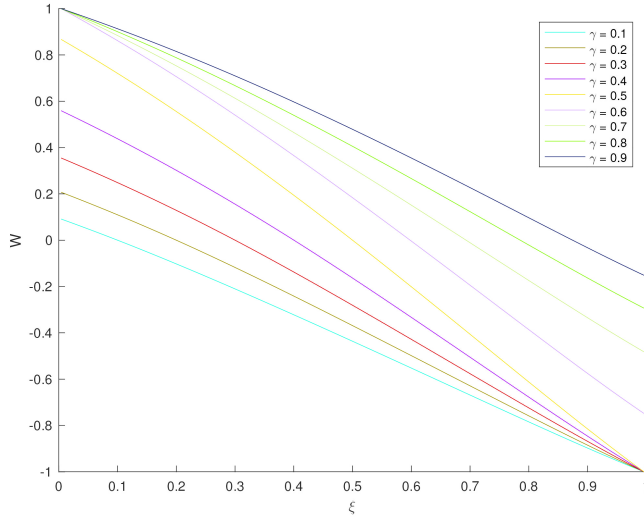
**Table 4.10:** The first  $k_1^2$  of the beam with varying flexural rigidity and location of the intermediate rigid support; the elastic end constraints are fixed to the values  $k_{rr} = k_{tr} = k_{rl} = k_{tl} = 1$ ;  $J = 6$ .

$\alpha = \beta$	$\gamma$				
	0.1	0.3	0.5	0.7	0.9
-0.2	1.9010	2.7984	3.9982	3.9408	3.2291
-0.1	1.9455	2.8924	4.0273	3.8223	3.1267
0	1.9930	2.9880	4.0431	3.7079	3.0308
0.1	2.0436	3.0868	4.0476	3.5978	2.9405
0.2	2.0979	3.1902	4.0418	3.4919	2.8552

In Figure 4.7, the normalised first mode shapes of the AFG beams with flexural rigidity, mass density  $D(\xi) = \rho(\xi) = 0.2$ , elastic supports at the ends  $k_{tl} = k_{rl} = k_{tr} = k_{rr} = 1$  and a rigid intermediate support at  $\gamma$  are shown.

## 4.4 Conclusions

The governing equation of the free transverse vibration of intact beams was presented in a matrix form using the Haar wavelet series and their integrals. The Euler-Bernoulli theory of bending was used to describe the motion of the beams. The dimensionless natural frequencies were determined for the uniform homogeneo-



**Figure 4.7:** Normalised first mode shapes of the non-uniform AFG Euler-Bernoulli beam with elastic supports at the ends and a rigid intermediate support.

us/non-homogeneous and non-uniform homogeneous beam models under various classical and elastic boundary conditions by requiring that the resulting governing equation, presented as a linear and homogeneous system of equations, had a non-trivial solution. The computed results agreed well with analytical and numerical results given in the literature. The considered models and results indicated that the HWTI method was accurate. Next, the proposed method was applied to non-uniform non-homogeneous Euler-Bernoulli beams. The dimensionless natural frequencies were calculated for non-uniform axially functionally graded Euler-Bernoulli beams. No reference was found in literature; therefore, the obtained results could serve as a theoretical foundation for natural frequency based methods and further research.

To sum up, the HWTI provides a unified and systematic procedure for the calculation of the natural frequency parameters and mode shape function. The benefits of the approach are its simplicity and sparse matrices. High accuracy is obtained even with a small number of grid points.



# Chapter 5

## Open cracks

In this chapter, the discrete Haar wavelet transform (DHWT), the artificial neural networks (ANNs) and the random forests (RFs) are applied to quantify the location and severity (the ratio of the crack depth to the height of the beam) of cracks in the Euler-Bernoulli type beam. In this regard, the first mode shape is decomposed into the Haar wavelet transform coefficients (HWT-Cs) with a small level of resolution. The obtained coefficients are used in the feature vector. In line, the machine learning methods are trained on the dimensionless natural frequency parameters (DFPs). The results of the approaches are compared to each other. The present chapter is partially based on the articles [Jaan 16, Hein 19a].

### 5.1 Related work

Cracks are the most common defects in mechanical structures [Elsh 18]. They appear in structural elements mainly due to a manufacturing defect, mechanical vibrations or cyclical loading [Niga 20]. Cracks present a threat to the whole structure since they change the behaviour of a construction to a considerable degree - the formation of a crack causes a stiffness reduction with an inherent reduction in the natural frequencies, an increase in the modal damping, changes in the mode shapes and an increase in the overall flexibility of the system [Abou 87, Elsh 18]. Hereof, detection of cracks at an early stage can increase the safety of a construction and help in scheduling maintenance procedures.

Modelling cracks or crack-like defects in beams has been the concern of structural engineering since the middle of the 20th century, after the concepts of fracture mechanics were defined [Erog 17]. In 1957, Irwin came up with the idea that a

crack in the elastic element caused local flexibility due to the strain energy concentration. He modelled the strain concentration using an equivalent spring [Erog 17]. This idea led Papaconomou and Dimarogonas [Papa 89] to the development of a more general factor called the stress intensity factor. The factor was used to calculate spring constants. Another approach to model a crack was proposed by Petrovski [Petr 81] which was based on the section modulus.

Some researchers modelled the Euler-Bernoulli beam equation so that the effect of a crack was taken into account. Christides and Barr [Chri 84] developed a cracked Euler-Bernoulli beam theory. They considered an exponential decay in the stress field due to the crack and incorporated the effect by introducing a parameter. The decay rate parameter had to be found from experimental or numerical analyses. Chondros et al. [Chon 98] developed a continuous cracked beam vibration theory. They considered that a crack introduced the continuous change in the flexibility and modelled it by incorporating a displacement field consistent with the singularity. A finite element method (FEM) was also used to model vibrations of cracked components. Haisty and Springer [Hais 88] developed a beam element to be used in the finite element codes. The crack was simulated as a linear spring for axial vibrations and as a torsional spring for bending vibrations. Gounaris and Dimarogonas [Goun 88] developed a finite element for a cracked prismatic beam for structural analysis based on the compliance matrix. All these studies created the background for the crack identification problem, including a recent area of interest in engineering which is crack modelling in nano-beam structures [Loya 09, Akba 17, Hein 19a].

The model-based crack identification problem as a forward problem stands for determining changes in structural dynamic characteristics of a given structure based on damage location and severity [Fan 11]. Shen and Pierre [Shen 90] suggested an approximate Galerkin solution to the one-dimensional cracked beam theory developed by Christides and Barr (the decay rate) for free bending of simply supported beams with pairs of symmetric open cracks. Fernandez-Sadez et al. [Fern 99] constructed the transverse deflection of the cracked beam by adding polynomial functions to the intact beams. The admissible function, which satisfied the boundary and the kinematic conditions, and the Rayleigh method were used to obtain the closed-form expressions for the fundamental frequency. An analytical approach based on the transfer matrix method was described by Attar [Atta 12]. Liang et al. [Lian 92] addressed the issue of frequency sensitivity in a simply supported beam or a cantilever with one crack. They developed analytical relationships between the eigenfrequencies and the magnitude/location of the crack. This method required the symbolic computation of the characteris-

tic equation. Rezaee and Hassannejad [Reza 11] proposed an approach based on the mechanical energy balance: the response of the cracked beam was obtained repetitively calculating the total mechanical energy corresponding to the initial conditions of the beam in terms of the specified point and its amplitude. Caddemi and Calio [Cadd 09] proposed the differential quadrature method which addressed discretisation, approximation and weight coefficients of the elastically supported cracked cantilever and irregular plates; yet, the accuracy of the method depended on the sampling points.

The exact close form solution of a uniform Euler-Bernoulli column with the presence of multiple cracks was proposed by Caddemi and Calio in 2008 [Cadd 08] and further developed by Caddemi and Morassi in 2013 [Cadd 13]. The Dirac's delta function and a rotational spring were used to model flexibility due to the crack. The authors stated that frequency sensitivity turned to be proportional to the potential energy stored at the cracked cross-section of the intact column.

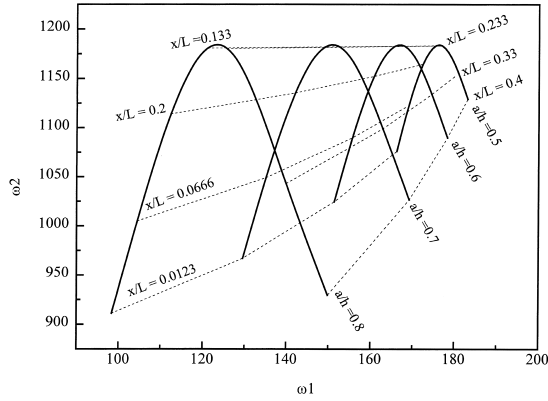
Researchers have tackled the inverse problem of crack identification using a proper analytical model, signal analysis, an efficient numerical and optimisation technique or a combination of several methods. Close attention has been devoted to the changes in the fundamental frequencies, mode shapes or dynamic flexibility [Atta 12]. Rizos et al. [Rizo 90] proposed a method based on the flexural vibration of uniform beams by representing the crack section as a rotational spring. The method required measurements of the amplitude at any two locations along the beam. A new technique for crack detection in beam structures based on kurtosis was presented by Hadjileontiadis et al. [Hadj 05a]. Specifically, the location of the crack was determined by the abrupt changes in the spatial variation of the analysed response, while the size of the crack was related to the estimate of the kurtosis. Compared to other crack detection methods, the proposed kurtosis based prediction scheme was attractive due to low computational complexity and inherent robustness against noise. Hu and Afzal [Hu 06] proposed a statistical algorithm for damage detection in timber beam structures calculating deviations in the mode shapes before and after damage. Although the method based on the mode shapes could accurately predict the location and size of the damage, the utility of it in practical applications was limited due to the requirement of a large number of sensors at every point of the structure.

In many studies, crack identification is determined by tracking changes in the first few natural frequencies. Owolabi and Seshadri [Owol 03] detected cracks in aluminium beam experimentally by measuring acceleration frequency response at seven different points on each beam model using a dual channel frequency analyser. The damage detection schemes depended on the measured changes in the first

three natural frequencies and the corresponding amplitudes of the measured acceleration frequency response functions. Baviskar et al. [Bavi 11] observed changes in the natural frequency due to the crack propagation both theoretically using finite element analysis software and experimentally using the fast Fourier transform analyser. The results of both methods were in good agreement. Meshram and Pawar [Mesh 15] revealed a relationship between a single crack depth, location and natural frequency using the finite elemental analysis. Barad et al. [Bara 13] detected the crack (its size and location) on the surface of a beam type element using the first two natural frequencies. Liang et al. [Lian 92] proposed a method similar to [Atta 12], but it required measurement of three transverse natural frequencies of the beam. The method was extended to the stepped beams [Nand 97a], to the cantilevers with inclined edge cracks and internal cracks [Nand 97b], and to the geometrically segmented beams [Chau 00]. Messina et al. [Mess 98] linked damage locations and extents with the frequency changes using a sensitivity matrix that could be obtained from the intact model. The authors set the objective function as the multiple damage location assurance criterion (MDLAC) and found the optimal solution that maximised the MDLAC using a traversal search strategy. The approach provided good predictions of both the location and the absolute size of the cracks. Lee [Lee 09] solved the inverse problem of crack identification using the Newton–Raphson method. The identified crack locations and sizes were in excellent agreement with the actual ones; however, the method had serious limitations in its application if the number of cracks in the beam was not known a priori.

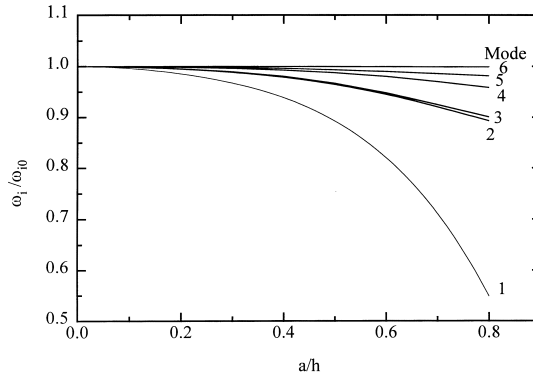
Noteworthy, Han et al. [Han 05b] reported in their research that the natural frequency shift was not sensitive to cracks. Salawu [Sala 97] confirmed that the natural frequency changes alone might not be sufficient for the unique identification of damage location. Specifically, cracks with similar depths but at two different locations caused the same amount of the frequency change (Figure 5.1 [Mahm 99]).

Recently, the ANNs have received wide acceptance for damage identification in civil structures [Haki 15]. This is due to the fact that ANNs are capable of pattern recognition, classification and signal processing. In [Mahm 99], Mahmoud and Kiefa investigated a steel cantilever beam with a single edge crack. They used the general regression neural networks (GRNN) and the first six natural frequencies in order to predict the crack size and location. The natural frequencies were calculated using M-matrix technique and the Newton-Raphson method. Mahmoud and Kiefa drew several important conclusions:



**Figure 5.1:** Nomographs for the first two natural frequencies ( $\omega_1$  and  $\omega_2$ ) with different crack sizes ( $a/h$ ) and crack locations ( $x/L$ ).

- the first two natural frequencies ( $\omega_1, \omega_2$ ) are not enough to predict the depth  $a/h$  and location  $x/L$  of the crack since the natural frequencies vary in a cyclic manner (Figure 5.1). For example, the crack of  $a/h = 0.5$  located at  $x/L = 0.067$  has the same values of  $\omega_1$  and  $\omega_2$  as the crack of  $a/h = 0.65$  and  $x/L = 0.333$ ;
- if the crack depth is smaller than  $a/h = 0.2$ , it is difficult to quantify since the change in the natural frequencies are small (Figure 5.2 [Mahm 99]).



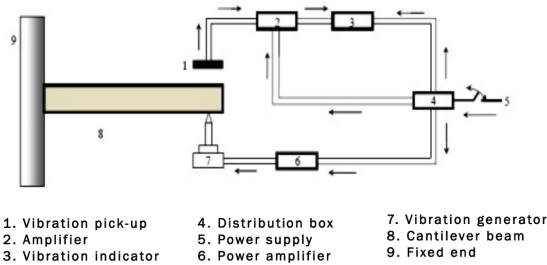
**Figure 5.2:** Variation of the natural frequencies with different crack depths.

The calculations by GRNN in [Mahm 99] showed that the network was capable of identifying the cracks in the range  $0.08 < a/h \leq 0.82$  quite accurately.

He et al. [He 01] implemented genetic algorithms for shaft crack detection. In the research, the authors formulated shaft crack detection as an optimisation problem by means of the finite element method. The accuracy of the crack location prediction was 98.46 per cent, and the accuracy in the case of the crack depth prediction was 88.22 per cent.

Hakim et al. [Haki 15] applied ANNs to detect cracks in I-beams, particularly the locations of two cracks and the severity (the cracks had the same depths). For the ANN training, 52 patterns of 3D finite element simulations and 52 experimentally obtained patterns were used. Each pattern contained the first natural frequency and 14 mode shape values of the first mode at the points on the centreline of the beam except the points at the ends. The optimal feed-forward back propagation ANN had the architecture of 15-8-4-3. The MSE of the test was 0.00449. The R-value of the crack severity and two locations of the cracks were 0.9925, 0.9680 and 0.9700, respectively. Later, Hakim et al. improved the results using an ensemble of five ANNs. Each ANN with the architecture of 15-8-4-3 was trained with the data which contained one of the first five natural frequencies and its mode shape values. The MSE was 0.0037. The R-value of the crack severity and two locations of the cracks were 0.9898, 0.9856 and 0.9855, respectively. It was also concluded that the identification of the crack location was a more challenging task than identifying of the crack depth.

In 2015, Sutar et al. [Suta 15] tried to realise an ANN-based controller for crack identification in an aluminium cantilever. The input parameters to the controller were relative divergence of the first three natural frequencies obtained experimentally (Figure 5.3 [Suta 15]) and the output parameters were crack depth



**Figure 5.3:** A block diagram of the experimental set-up to measure natural frequencies.

and location in the dimensionless form. A three-layered feed-forward back propagation ANN with nine neurons in the hidden layer was used for the training. The results showed that the mean absolute percentage error between the actual and

the predicted responses was less than 15 per cent. The authors assumed that the result could be improved if the number of natural frequencies in the feature vector was increased.

Although the results look promising, some issues need to be discussed and resolved. Firstly, in engineering “data are often the result of expensive experiments and will be in short supply; in this case, the only way to ensure generalisation is to restrict the number of weights in the network” [Word 11]. Secondly, the nature of the data is a critical aspect. According to Ndambi et al. [Ndam 02], natural frequencies can follow the damage severity but are not influenced by the crack damage locations; the modal assurance criterion is, in contrast, less sensitive to crack damage compared with the natural frequencies; the coordinate modal assurance criterion can localise damage in the beams but cannot follow severity and spreading; the damage indices method based on the strain energy appears to be more precise than the other methods in damage localisation, but the difficulty remains when the damage is spread out over a certain length of the beam. To overcome the stated issues, it is proposed to transform the numerically calculated or measured mode shapes into the Haar wavelet coefficients (Subsection 2.2.1) as a part of the data processing procedure since the wavelet transform can reveal some hidden parts of data that other signal analysis techniques fail to detect [Yan 07]. The obtained data are used for the ANN and RF training. The results of different machine learning methods and datasets are compared to each other with the aim to highlight the most promising approach. No related work has been found in the literature.

## 5.2 Quantification of the crack

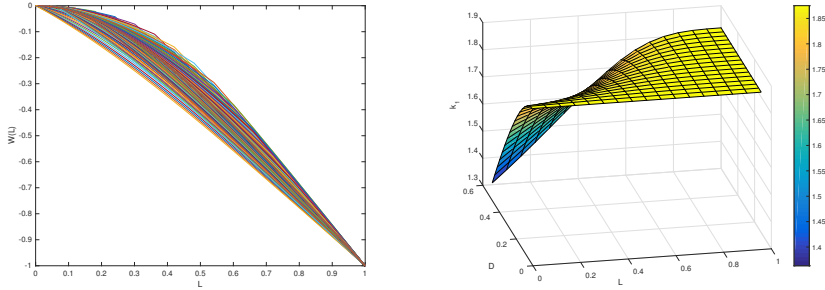
The present simulation study was based on the free vibration of a uniform homogeneous Euler-Bernoulli type beam with a crack. The left end of the beam was clamped and the right end was free. The ratio between the beam height and length was set to 0.25. A crack of an arbitrary depth ( $D$ ) was modelled to occur at an arbitrary point of the beam ( $L$ ). The corresponding mathematical model of the cracked beam was described in Subsection 3.1.4.

### 5.2.1 Datasets

An essential prerequisite to train a predictive model is to identify a set of features that may serve as indicators of the phenomenon in question. The literature review shows that most of the studies consider the first three natural frequencies as input

features [Erog 16]. The frequencies are obtained experimentally or calculated using the FEM or power series technique. According to Mahmoud and Kiefa [Mahm 99], the fewer the number of the natural frequencies, the less accurate predictions of the ANNs are.

In the present study, a more rigorous approach was adopted. It was assumed that the predictive model could be built in a more manageable way using the Haar wavelet transform. In order to evaluate the hypotheses, two sets of data were calculated numerically. In the first set, each pattern contained the scaled values of the crack depth, location, and the first eight DFPs of vibration ( $k_i$ ,  $i = 1, \dots, 8$ ). The DFPs were calculated using the equations from Subsection 3.1.4. The calculated DFPs related to the ones available in [Rosa 09]. The calculated first mode shapes and DFPs are shown in Figure 5.4. The first 25 patterns are tabulated in Table A1 (Appendix A).



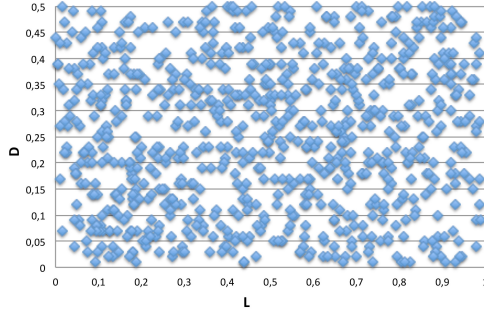
**Figure 5.4:** The first mode shape (left) and DFPs (right) in function of the crack location ( $L$ ) and the crack depth ( $D$ ).

In the second set of data, each pattern contained the scaled values of the crack depth, location, and 64 HWTCs ( $h_j$ ,  $j = 1, \dots, 64$ ). The coefficients were calculated using (2.7) - (2.10) and normalised as follows:

- calculate the first DFP of the cracked cantilever and obtain the Haar wavelet transform coefficients of the first mode shape  $y_c$ ;
- calculate the first DFP of the intact cantilever and obtain the Haar wavelet transform coefficients of the first mode shape  $y_i$ ;
- calculate the difference  $y_c - y_i$ ;
- normalise the results.



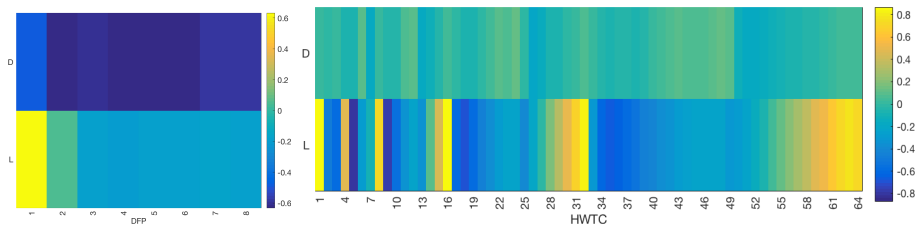
In total, each dataset contained 750 patterns. The location and depth of the cracks in the patterns were chosen randomly. On practical grounds, the minimum and maximum values of the crack depth were set to 0.01 and 0.5. The location values of the cracks were set in the range from 0.001 to 0.99 (Figure 5.5).



**Figure 5.5:** Distribution of crack characteristics ( $L$  - location,  $D$  - depth).

The calculation of the first eight DFPs took 15 times more time than the calculation of 64 HWTCs. According to Majak [Maja 18], the calculation time depended on the mesh used and the accuracy required. The computing time of the DFPs could be reduced substantially by applying higher-order methods which allowed to achieve high accuracy with a smaller mesh.

Before providing the ANNs with the data, the correlation between the crack characteristics and other features was observed (Figure 5.6). A few individual metrics from the HWTC-based dataset had a strong positive or negative correlation ( $R > |0.7|$ ) with the crack location. A moderate negative correlation was observed between a few individual metrics from the DFP-based dataset and the crack depth. There were no individual metrics which strongly correlated with both characteristics at the same time (Tables 5.1 and 5.2). This was in line with the conclusions presented by Mahmoud and Kiefa [Mahm 99].



**Figure 5.6:** Correlation between crack characteristics and the DFPs or the HWTCs.

**Table 5.1:** Correlation between the DFPs and the crack characteristics.

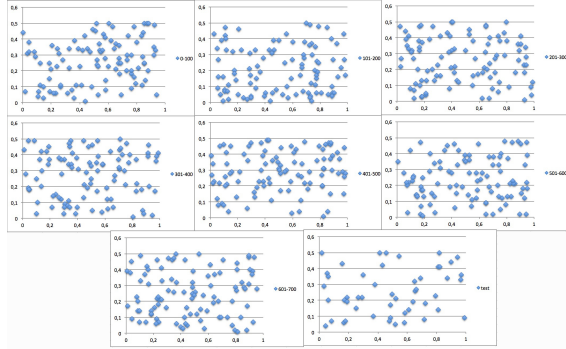
Crack	$f_1$	$f_2$	$f_3$	$f_4$	$f_5$	$f_6$	$f_7$	$f_8$
$L$	6.21e-1	5.5e-2	-1.78e-1	-2.1e-1	-1.9e-1	-1.9e-1	-1.67e-1	-1.81e-1
$D$	-4.88e-1	-6.31e-1	-5.97e-1	-6.18e-1	-6.32e-1	-6.32e-1	-5.74e-1	-5.86e-1

**Table 5.2:** Correlation between the HWTCs and the crack characteristics.

Crack	$h_1$	$h_5$	$h_8$	$h_9$	$h_{16}$	$h_{32}$	$h_{62}$	$h_{63}$
$L$	8.68e-1	-8.06e-1	7.27e-1	-7.81e-1	8.46e-1	8.35e-1	7.13e-1	-7.76e-1
$D$	7e-3	-6.5e-2	1.3e-2	-4.8e-2	5.2e-2	5.8e-2	4.6e-2	5.4e-2

The correlations between the features themselves were not studied in the thesis as it would not have added any impact to the research. The primary goal of the present study was to obtain models with remarkable predictive accuracy rather than to obtain explainable models.

Next, to assess the influence of the training pattern amount on the predictive accuracy, 700 patterns were randomly divided into reasonably small parts, 100 patterns in each portion (Figure 5.7). In the eighth portion, there were 50 patterns that were used for testing the predictive models.



**Figure 5.7:** Distribution of the training patterns.

Before providing the machine learning methods with the feature vectors, the data were scaled to fall in the range of zero and one:

$$x_S = \frac{x - x_{min}}{x_{max} - x_{min}} \quad (5.1)$$

where  $x_S$  was the scaled value of  $x$ ;  $x_{max}$  and  $x_{min}$  were the maximum and minimum values of the variable  $x$  in the dataset.

## 5.2.2 Feed-forward neural networks with back propagation

ANN model building refers to selecting an “optimal” network topology, data representation, training algorithm, training parameters, and terminating criteria, such that some desired level of performance is achieved [Twom 95]. In the present study, different feed-forward back propagation ANNs were examined. The following factors were manipulated:

- the training algorithm,
- the number of neurons in the hidden layer,
- the size of the training set,
- the features in the training patterns.

Each ANN was constructed using the *fitnet* function in the MATLAB environment. The ANNs were trained by one of the following training function (Table 2.1): Levenberg-Marquardt (LM), scaled conjugate gradient (SCG), resilient back propagation (RP), Broyden–Fletcher–Goldfarb–Shanno (BFGS), and Bayesian regularisation (BR). For the RP, the learning rate was set to 0.01.

To avoid the construction of unreasonably large ANNs, the number of hidden layers was set to one. According to Beale et al. [Beal 16], “a network of two layers, where the first layer is sigmoid and the second layer is linear, can be trained to approximate any function arbitrarily well”. Following this recommendation, the Elliot sigmoid function was chosen for the hidden layer and the linear transfer function - for the output layer.

The number of neurons in the input layer was dictated by the input variables of the model. The number of neurons in the hidden layer was initially set to ten and gradually increased to 150 with the increment of 20 neurons in order to find a reasonable solution. The number of neurons in the output layer was set to two: one for the crack location and one for the crack extension. A general architecture of the ANN is shown in Figure 5.8 [Beal 16].

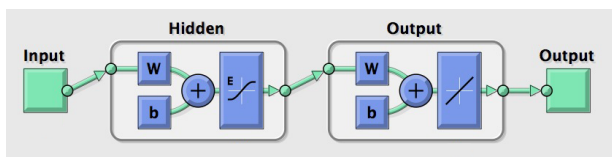


Figure 5.8: Feed-forward back propagation ANN.

To speed up the learning process [Beal 16], the training was performed in the batch mode (the weights and biases were updated after all inputs were presented). The network training was stopped at one of the following conditions:

1. the magnitude of the gradient was less than  $1e - 7$ ,
2. the number of the validation checks reached 6,
3. the number of the epochs reached 1000,
4. the performance value became  $1e-4$ .

The training time was not limited.

The number of the training patterns was initially set to 100 and gradually increased to 700 with step 100. Each ANN was trained 50 times starting at randomly chosen initial conditions in the weight space in the range of  $-1$  to  $1$ .

The test set contained 50 patterns that were not shown to the ANNs during the training. The assessment of different ANN performances was made on this set on the basis of the mean square error (MSE).

Table 5.3 shows the results of the training and testing of the ANNs provided with the DFPs. Table 5.4 shows the results of the training and testing of the ANNs provided with the HWTCs. Both tables show the average MSE of 50 test crack quantification (localisation and extension) and 50 trainings. The tables also show the correlation parameter (the R-value) for the predicted location and depth of the test cracks, the average learning time per network training, the number of the neurons in the hidden layer, the number of the patterns in the training set and the reason of training stop according to the list above.

In the case of training on the DFPs, the lowest average MSE of 50 runs to quantify 50 cracks from the test set was  $3.4e-3$ . The average R-value for predicting the location was  $9.765e-1$ ; the average R-value for the prediction of the depth was  $9.713e-1$ . The results were obtained by the ANNs with ten neurons in the hidden layer trained by the Levenberg-Marquardt using 700 training patterns with eight DFPs in each.

The results of the scaled conjugate gradient, resilient propagation and BFGS back propagation functions were mutilated by overfitting: the MSE was higher on the testing set than on the training set.

**Table 5.3:** Average results of the predicted 50 cracks using different training functions, ANN configurations and DFPs.

Training function	Avg. training $MSE$	Avg. test $MSE$	Avg. $R_{location}$	Avg. $R_{depth}$	Avg. time per training (s)	Avg. nr of epochs	Neurons (10,30,...,150)	Training patterns(100, 200,...,700)	Stopping reason
<i>LM</i>	3.5e-3	<b>3.4e-3</b>	9.765e-1	9.713e-1	1.157	228	10	700	2
<i>SCG</i>	1.39e-2	1.60e-2	8.311e-1	8.991e-1	0.188	92	10	700	2
<i>RP</i>	1.16e-2	1.32e-2	8.053e-1	9.219e-1	2.97e-1	187	130	700	2
<i>BFG</i>	7.7e-3	9.2e-3	9.010e-1	9.438e-1	60.298	132	90	700	2
<i>BR</i>	5.3e-3	4.4e-3	9.618e-1	9.531e-1	6.75	1000	10	500	3

**Table 5.4:** Average results of the predicted 50 cracks using different training functions, ANN configurations and HWTGs.

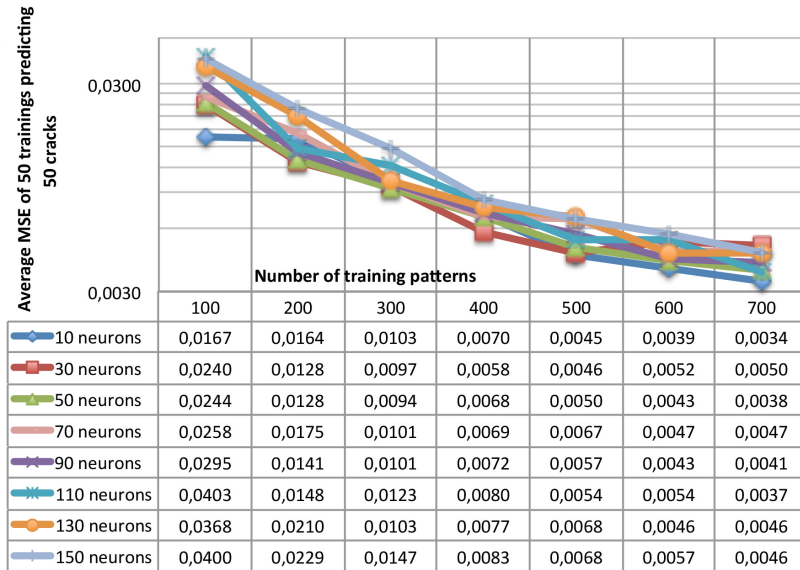
Training function	Avg. training $MSE$	Avg. test $MSE$	Avg. $R_{locat}$	Avg. $R_{depth}$	Avg. time per training (s)	Avg. nr of epochs	Neurons (10,30,...,150)	Training patterns	Wavelet coef (8,16,...,64)	Stopping reason
<i>LM</i>	3.8e-3	3.6e-3	9.999e-1	8.216e-1	63.345	134	150	700	8	2
<i>SCG</i>	8.2e-3	8.4e-3	9.959e-1	6.209e-1	0.312	64	70	700	16	2
<i>RP</i>	4.4e-3	5.4e-3	9.974e-1	7.610e-1	0.5310	126	110	700	48	2
<i>BFG</i>	6.6e-3	5.9e-3	9.993e-1	7.258e-1	1732.67	86	130	700	8	2
<i>BR</i>	3.4e-3	<b>3.1e-3</b>	9.998e-1	8.389e-1	6.375	1000	10	300	8	3

According to Table 5.3, the Bayesian regularisation also showed accurate results on the crack quantifications. The training was stopped due to the maximum number of epochs (in the pre-set training determination conditions, the maximum number of the epoch was 1000). The increase of the epochs up to 6000 resulted in significant improvement in predictive accuracy: the average training MSE was  $2.2e-3$ , the average testing MSE was  $2.2e-3$ , the average R-value of the crack localisations was  $9.745e-1$ , and the average R-value of the crack depth quantifications was  $9.620e-1$ . The average time per training increased more than six times.

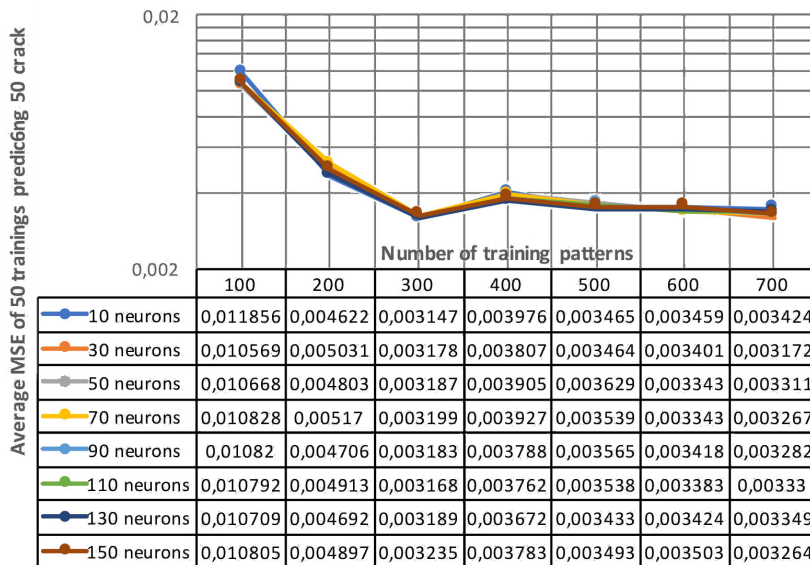
In case of training on the HWTCs, the lowest average MSE of 50 runs to quantify 50 cracks from the test set was  $3.1e-3$ . The average R-value for the prediction of the location was  $9.998e-1$ ; the average R-value for predicting the depth was  $8.389e-1$ . The average result was obtained by the ANN with ten neurons in the hidden layer. The network was trained by the Bayesian regularisation using 300 training patterns and 1000 epochs. In each pattern, there were the first eight HWTCs out of 64. An increase of the epochs from 1000 to 4500 or 6000 did not show any satisfactory improvement in the prediction accuracy.

Next, for the most promising approaches (the Levenberg-Marquardt and DFPs; the Bayesian regularisation and HWTCs), the influence of the neurons, the training patterns and their amount on the predictive accuracy of the ANNs to quantify the cracks are shown in Figure 5.9. The approach based on the DFP dataset required at least 700 training patterns in order to learn the relationship between the inputs and outputs. In the case of the HWTC dataset, 300 training patterns were sufficient.

Afterward, in order to improve predictive accuracy, an ensemble of 50 individual ANNs was created. The idea originated from the articles [Marw 99, Haki 15, Beal 16], in which the ensembles of ANNs produced better results than individual networks. Figure 5.10a shows the results of 50 ANNs with ten neurons in the hidden layer trained by the Levenberg-Marquardt and 700 training patterns containing eight DFPs. The MSE of the predicted parameters of the cracks from the test set reduced from  $3.3e-3$  to  $1.3e-3$  ( $MSE_D = 9e-4$ ,  $MSE_L = 1.6e-3$ ). Figure 5.10b shows the results of 50 ANNs with ten neurons in the hidden layer trained by the Bayesian regularisation and 300 training patterns containing eight HWTCs. The MSE of the predicted parameters of the cracks from the test set reduced from  $3.1e-3$  to  $2.3e-3$  ( $MSE_D = 4.6e-3$ ,  $MSE_L = 7e-6$ ). The target (calculated) crack characteristics and the predicted values are visualised in Figures 5.10 and 5.11. In most cases, large errors occurred from the quantification of the crack depth.

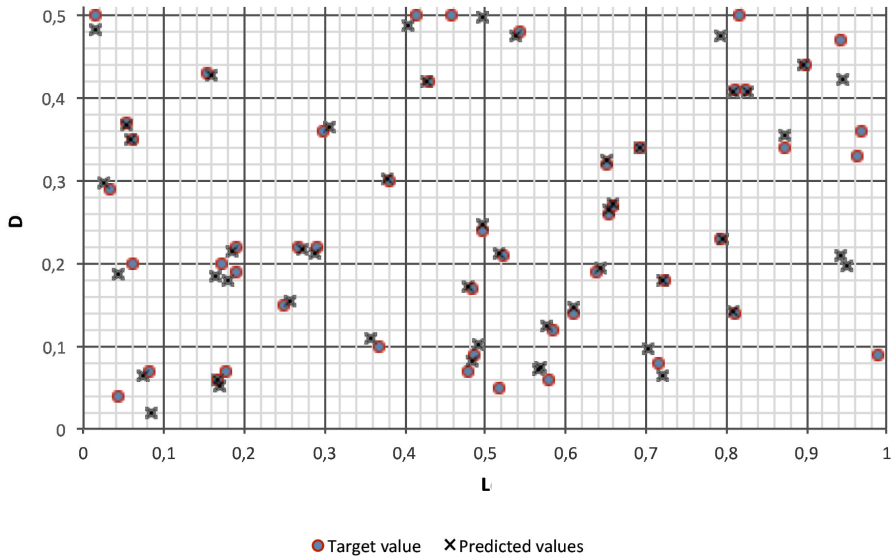


(a) Averaged MSE of crack predictions by Levenberg-Marquardt and eight DFPs.

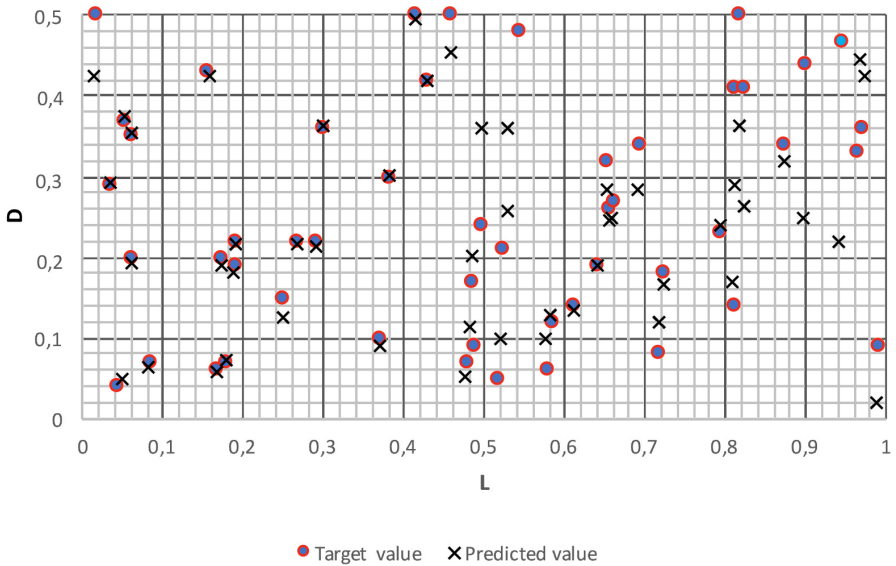


(b) Averaged MSE of crack predictions by Bayesian regularisation and eight HWTs.

**Figure 5.9:** Average MSE of quantification 50 cracks using varying number of hidden neurons and training patterns.



(a) Crack characteristics predicted by an ensemble of 50 ANNs trained by Levenberg-Marquardt and 700 training patterns containing eight DFPs.

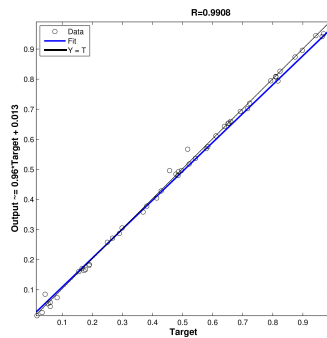


(b) Crack characteristics predicted by an ensemble of 50 ANNs trained by Bayesian regularisation and 300 training patterns containing eight HWTCs.

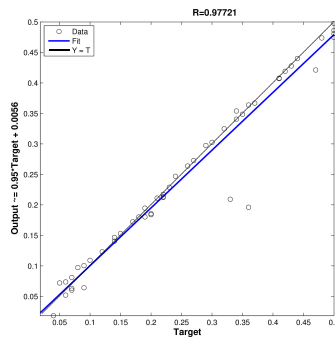
**Figure 5.10:** Characteristics of 50 test cracks: x - predicted depth and location; o - target values.



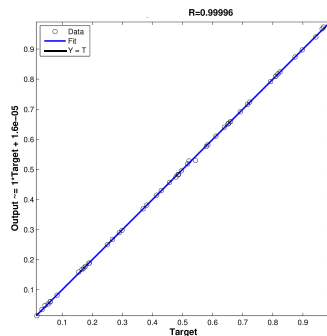
Nevertheless, the ensemble of the ANNs provided with the DFPs predicted crack depth more precisely than the ensemble of the ANNs provided with the HWTCs ( $R = 9.772e-1$  and  $R = 8.871e-1$ , respectively). The observation was in line with the correlation coefficients (Tables 5.1 and 5.2). In the case of location predictions, the results were vice versa. The R-value between the outputs and the crack location targets was very close to 1 (in the case of the HWTCs  $R = 9.999e-1$ , and in the case of the DFPs  $R = 9.908e-1$ , respectively), which indicated a close fit and accurate performance of the ANNs. The observation was also in line with the correlation coefficients (Tables 5.1 and 5.2).



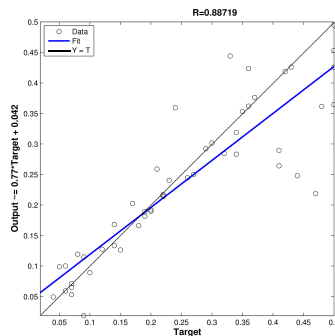
(a) Location prediction.



(b) Depth prediction.



(c) Location prediction.

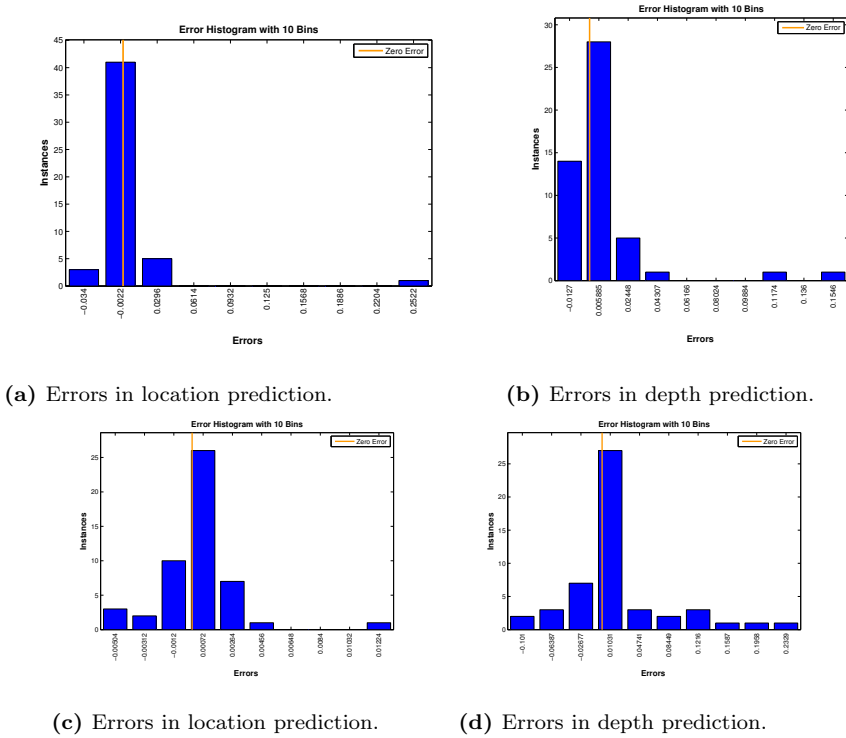


(d) Depth prediction.

**Figure 5.11:** Correlation plot for the predicted characteristics of 50 cracks: (a), (b) predictions based on eight DFPs; (c), (d) predictions based on eight HWTCs.

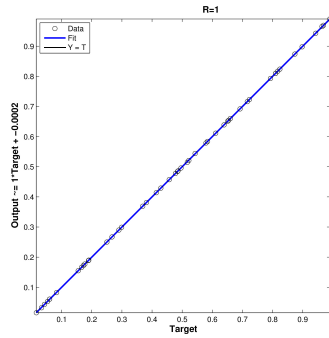
The error distributions for both approaches are shown in Figure 5.12. For the HWTCs, the absolute error of the crack localisation was less than 0.0051 in 49

cases. For the DFPs, the absolute error of the crack depth quantification was less than 0.044 in 48 cases.

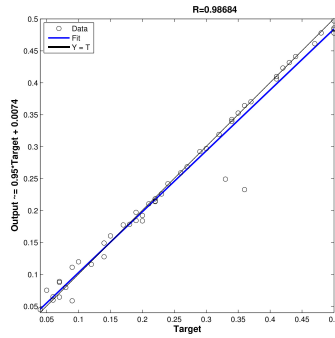


**Figure 5.12:** Error distribution for the predicted characteristics of 50 cracks: (a), (b) predictions based on 8 DFPs; (c), (d) predictions based on 8 HWTCs.

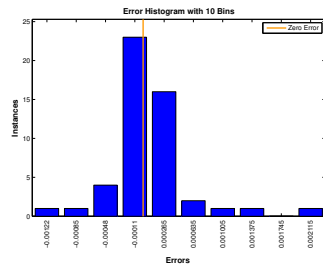
To improve the results, the methods were combined: the ensemble of 50 ANNs provided with the DFPs was used to predict the crack depths, and the ensemble of 50 ANNs provided with the HWTCs was used to predict the location of the cracks. In such a case, the average MSE of the crack quantification was  $2e-4$  ( $MSE_D = 5e-4$ ,  $MSE_L = 2e-7$ ), the R-value for the prediction of the location was 1.00, and the R-value for predicting the depth was  $9.868e-1$ . The absolute error of the crack localisation was less than 0.0021 and the absolute error of the crack depth quantifications was less than 0.044 in 48 cases (Figure 5.13). The increased accuracy could be explained by the fact that each ANN had one output neuron instead of two and an ensemble of 50 ANNs produced more accurate predictions than a single ANN. Nevertheless, the combined approach could not follow the severity of cracks if it was located very close to the free end of the beam.



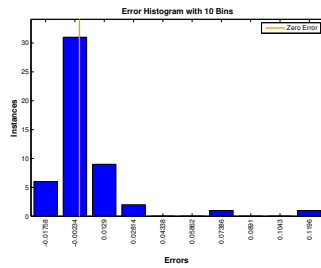
(a) Location prediction.



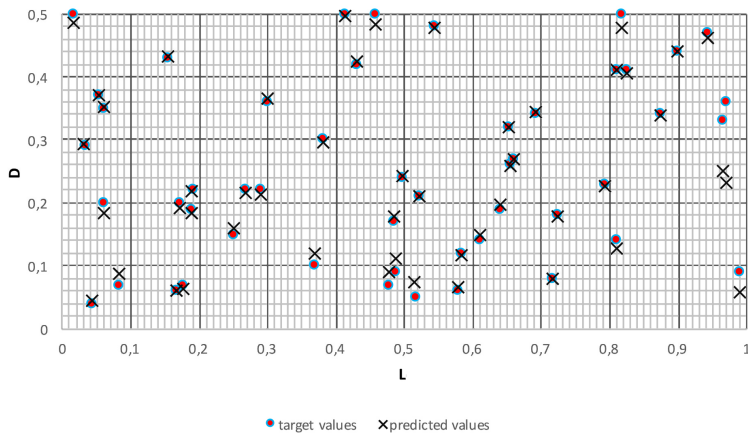
(b) Depth prediction.



(c) Location prediction.



(d) Depth prediction.



(e) Characteristics of the target and predicted cracks.

**Figure 5.13:** The results of the complex approach: 50 ANNs trained on the DFPs to predict the depth of the cracks; 50 ANNs trained on the HWTCs to localise the cracks.

### 5.2.3 Random forest

Next, the previous simulation study on the crack quantification was examined by the RFs. Providing the same mathematical models and datasets, it was assumed that the RFs were easier to tune due to the smaller number of the hyperparameters, the training time could be shorter and the performance could be at least as accurate as of the ANNs. To test the hypothesis, the following configurations of the RFs were manipulated:

- the number of predictors in samples (8 DFPs; 8, 16, 32, 48 or 64 HWTCS);
- the number of predictors without replacement in samples  $p$  (1/6, 1/2 and 2/3 of the predictors in the pattern);
- the number of trees (10, 20, 30, 40, 50, 75, 100, 150, 200, 250, 300, 400, 500, 750, 1000);
- the number of training patterns (100, 200, ..., 700).

Each RF configuration was tested 50 times on 50 cracks from the testing set. Tables 5.5 and 5.6 show the average MSE and the configurations of the RFs with the lowest MSE.

**Table 5.5:** The most accurate results of 50 crack quantifications using the RFs and DFPs ( $L$  - location,  $D$  - depth of the crack).

Crack characteristic	Nr of training patterns	Nr of predictors in a pattern	Predictors without replacement ( $p$ )	Nr of trees	Avr. test $MSE$	Avg. $R$	Avg. training time
$L$	500	8	4	20	<b>2.0e-3</b>	9.896e-1	0.1108
	500	8	6	10	2.1e-3	9.885e-1	0.0674
	600	8	4	10	2.1e-3	9.880e-1	0.0619
	500	8	4	40	2.2e-3	9.888e-1	0.2112
	600	8	4	400	2.3e-3	9.881e-1	2.1502
$D$	700	8	6	50	<b>8e-4</b>	9.841e-1	0.3847
	700	8	4	100	8e-4	9.821e-1	0.6683
	600	8	6	300	8e-4	9.826e-1	2.0682
	700	8	6	750	8e-4	9.820e-1	5.7232
	700	8	4	40	9e-4	9.812e-1	0.2739

In the case of training on the DFPs, the lowest average MSE to localise and estimate the severity of 50 cracks after 50 runs were 2.0e-3 and 8e-4, respectively. The corresponding average R-value of the location prediction was 9.896e-1; the average R-value of predicting the depth was 9.841e-1. The results were obtained by the RF with 20 trees provided with 500 training patterns and by the RF with 50 trees provided with 700 training patterns, respectively.

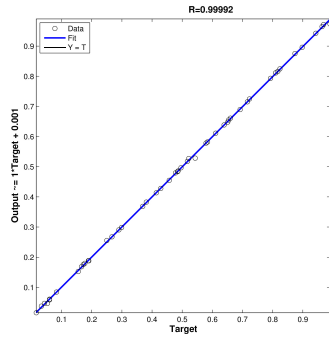
**Table 5.6:** The most accurate results of 50 crack quantifications using the RFs and the HWTCs ( $L$  - location,  $D$  - depth of the crack).

Crack characteristic	Nr of training patterns	Nr of predictors in a pattern	Predictors without replacement ( $p$ )	Nr of trees	Avr. test $MSE$	Avg. $R$	Avg. training time
L	700	8	6	10	<b>8e-6</b>	9.999e-1	0.0653
	700	8	6	20	9e-6	9.999e-1	0.1201
	700	8	6	100	1.1e-5	9.999e-1	0.5646
	500	8	6	10	1.2e-5	9.999e-1	0.0587
	500	8	6	100	1.4e-5	9.999e-1	0.4883
D	700	16	11	10	<b>6.1e-3</b>	8.491e-1	0.1365
	700	64	43	100	6.3e-3	8.395e-1	2.9505
	700	64	43	150	6.4e-3	8.361e-1	4.4674
	700	64	32	75	6.4e-3	8.374e-1	1.7222
	700	64	32	150	6.4e-3	8.378e-1	3.4962

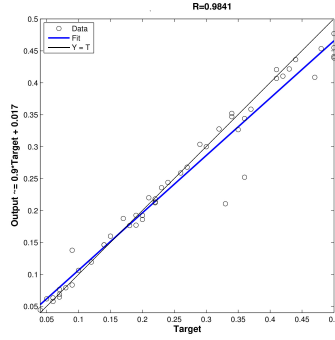
In the case of training on the HWTCs, the lowest average MSE of 50 runs to localise and estimate the severity of the test cracks were 8e-6 and 6.1e-3, respectively. The average R-value for the prediction of the location was 9.999e-1; the average R-value for predicting the depth was 8.491e-1. The results were obtained by the RF with ten trees provided with 700 training patterns.

As in the case with the ANNs, the dataset of eight DFPs produced more accurate predictions of the crack depths; meanwhile, the dataset of eight HWTCs produced more precise predictions of the crack locations. On this premise, the combined approach (RFs, DFPs and HWTCs) was tested. The results are shown in Figure 5.14. In this case, the average MSE of the crack quantification was 4e-4 ( $MSE_D = 8e-4$ ,  $MSE_L = 8e-6$ ), the R-value for the prediction of the location was 9.999e-1, and the R-value for the prediction of the depth was 9.841e-1. The absolute error of the crack localisation was less than 0.0044 in 48 cases and the absolute error of the crack depth quantification was less than 0.045 in 45 cases.

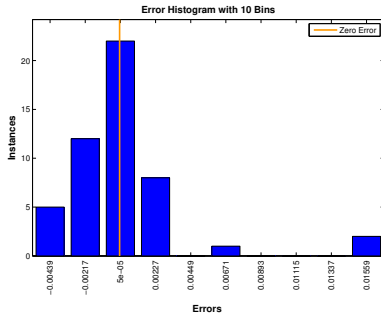
In comparison with the ANNs, the RFs produced slightly less accurate predictions of the crack characteristics. Nevertheless, the RFs configuration required less hyperparameters to adjust and the training time was notably shorter.



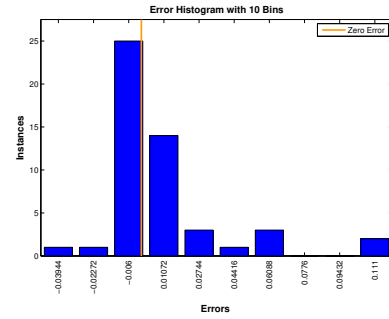
(a) Location prediction.



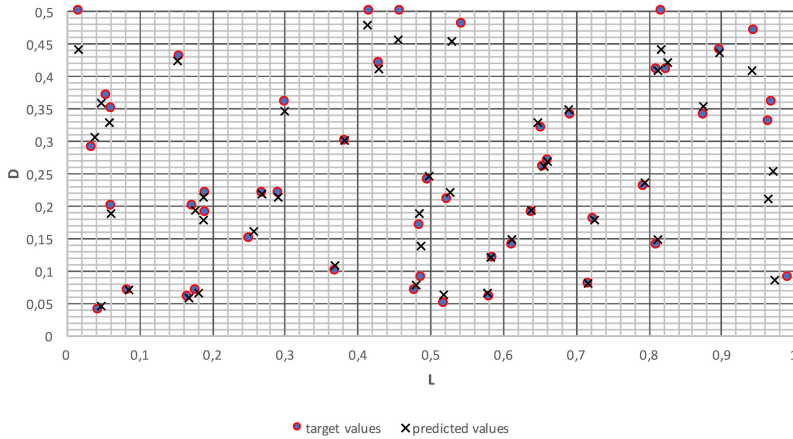
(b) Depth prediction.



(c) Location prediction.



(d) Depth prediction.



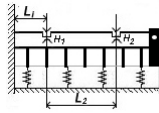
(e) Characteristics of the target and predicted cracks.

**Figure 5.14:** The results of the complex approach: 50 RF trained on the DFPs to predict the depth of the cracks; 50 RFs trained on the HWTCs to predict location of the crack.

### 5.3 Quantification of two cracks

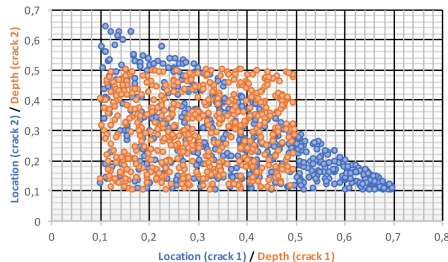
The proposed approach of the DFPs, the HWTCs and the ensembles was applied to the quantification of multiple cracks in the beam. The predictive models which produced the most promising results of one crack characteristics were verified whether they could quantify the characteristics of two cracks in the beam. As distinct from the previous simulation studies, the number of epochs was increased from 1000 to 10000. The settlement was motivated by the complexity of the task to quantify four characteristics of the cracks and the enhanced performance of the Bayesian regularisation with numerous iterations.

In the present simulation study, the beam was placed on the Pasternak elastic foundation ( $G_1 = 10, G_2 = 2.5\pi^2$ ). One end of the beam was clamped, the other one was pinned (Figure 5.15). The ratio between the beam height and length was set to 0.1. The beam length was scaled to 1. The corresponding mathematical model was described in Subsections 3.1.4 and 3.1.5.



**Figure 5.15:** A clamped-pinned beam with two cracks and on the Pasternak elastic foundation.

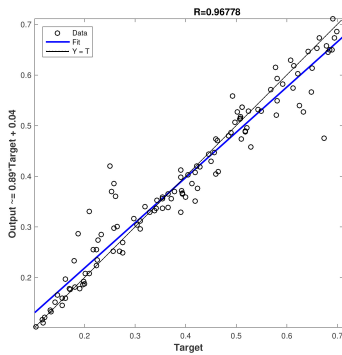
Two cracks were induced at the arbitrary points along the beam. One crack was induced from 0.1 to 0.7 units from the left side of the beam ( $L_1$ ); the second crack was induced from 0.1 to 0.8 units from the first crack ( $L_2$ ) so that both cracks were in the range within 0.1 and 0.8 units. On practical grounds, the minimum and maximum values of crack depths ( $D_1, D_2$ ) were set between 0.01 and 0.5 (Figure 5.16).



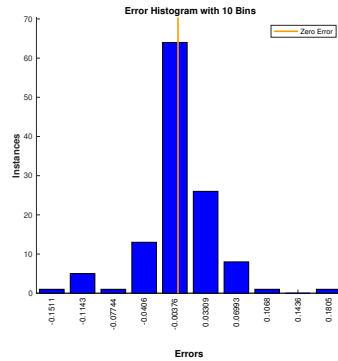
**Figure 5.16:** The dataset of two cracks in the beam.

The dynamic response of the cracked beam (the first mode shape and the first eight DFPs) was computed using the equations from Subsections 3.1.2 and 3.1.5. In the first dataset, the records contained scaled characteristics of the cracks (location and depth) and the first eight DFPs. In the second set of data, each record contained scaled crack characteristics, and 64 HWTCs. The coefficients were calculated using (2.7) - (2.10) and normalisation. In total, each dataset contained 1230 patterns: 1110 records were used for training and 120 records were used for testing the predictive models.

Figure 5.17 shows the results obtained by the ensembles of the ANNs. In particular, the depths of two cracks were predicted by two ensembles with 50 ANNs in each. Each ANN had ten hidden nodes in the hidden layer. The ANNs were trained by the Bayesian regularisation and provided with the dataset of the DFPs. The training was stopped when the number of epochs reached 10000. The MSE of the first crack depth was  $1.1e-3$  and of the second crack depth was  $1.0e-3$ . The R-values were  $9.515e-1$  and  $9.586e-1$ , respectively. The locations of the cracks were predicted by the other two ensembles of 50 ANNs. Each ANN also had ten hidden nodes in the hidden layer. The ANNs were trained by the Bayesian regularisation and provided with the dataset of the HWTCs. The feature vector contained the first eight HWTCs out of 64. The training was stopped when the number of epochs reached 10000. The MSE of the first crack location was  $2.1e-3$  and the MSE of the distance between two cracks was  $1.9e-3$ . The R-values were  $9.553e-1$  and  $9.677e-1$ , respectively.

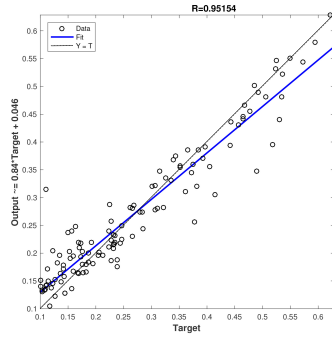


(a)

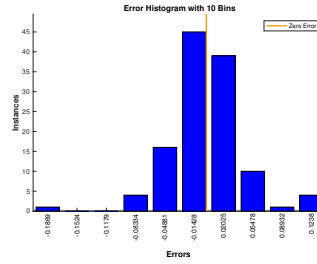


(b)

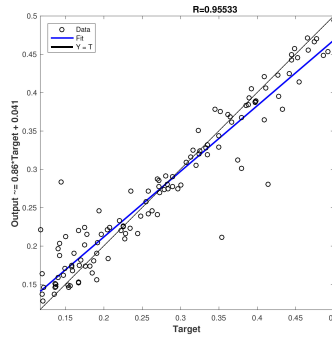




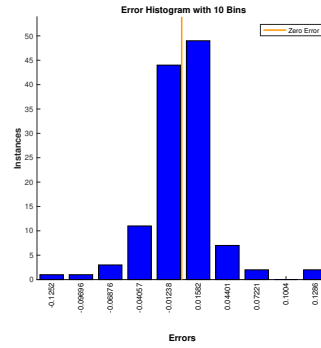
(c)



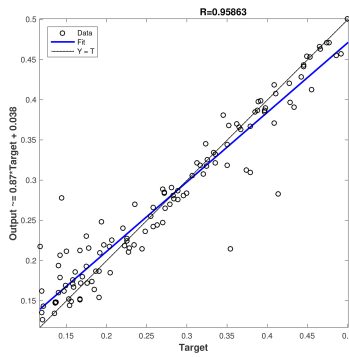
(d)



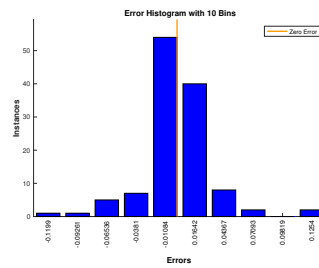
(e)



(f)



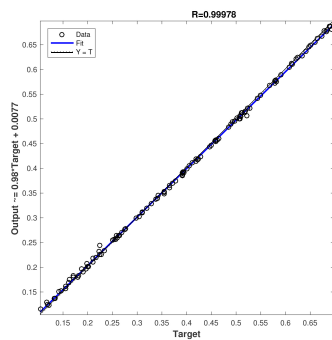
(g)



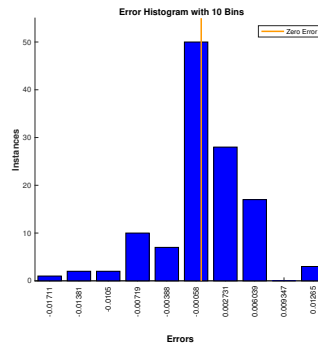
(h)

**Figure 5.17:** Correlation and error distribution of the predicted cracks by the ensemble of the ANNs: (a)-(b) location from the left side of the beam; (c)-(d) distance between two cracks; (e)-(f) depth of the first crack; (g)-(h) depth of the second crack.

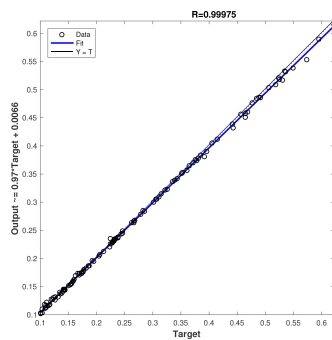
Figure 5.18 shows the results obtained by the RFs. Specifically, the depths of two cracks were predicted by two RFs with 50 trees in the forest trained independently. Each RF was provided with the same DFP-based dataset. The feature vector contained eight DFPs (six predictors without replacement). The MSE of the first crack depth was  $6.3e-6$  and of the second crack depth was  $5.9e-6$ . The R-values were  $9.998e-1$  and  $9.998e-1$ , respectively. The locations of the cracks were predicted by the other two RFs with ten trees in each forest. The RFs were provided with the HWTC-based dataset. The feature vector contained the first eight HWTCs out of 64 (six predictors without replacement). The MSE of the first crack location was  $2.4e-5$  and the MSE of the distance between two cracks was  $2.1e-5$ . The R-values were  $9.997e-1$  and  $9.997e-1$ , respectively.



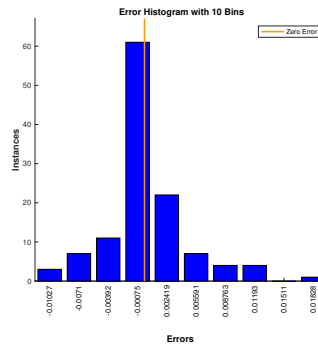
(a)



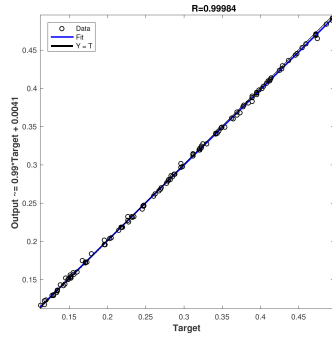
(b)



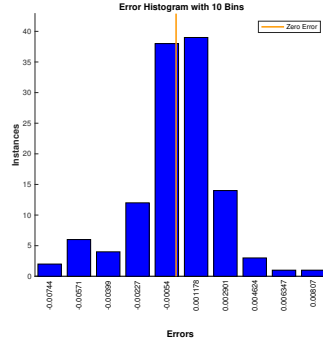
(c)



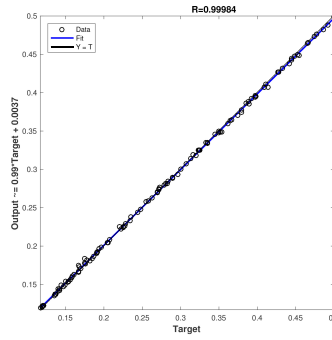
(d)



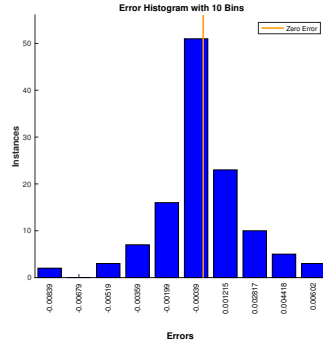
(e)



(f)



(g)



(h)

**Figure 5.18:** Correlation and error distribution of the predicted cracks by the ensemble of the RFs: (a)-(b) location from the left side of the beam; (c)-(d) distance between two cracks; (e)-(f) depth of the first crack; (g)-(h) depth of the second crack.

## 5.4 Discussion and conclusions

The primary aim of the present chapter was to find an efficient model for the crack quantification in the beam. The feed-forward back propagation ANNs and the RFs were incorporated into the search for an accurate predictive model of the formulations. Another objective of the study was connected to the datasets, specifically to the feature vectors and the size of the training set. Two sets of data were calculated numerically. The first one contained the first eight DFPs; the other one - up to 64 HWTCs derived from the first mode shape. The hypotheses were evaluated on the testing set (not shown to the models in advance).

The results of one crack quantification showed that the ensemble of 50 ANNs produced as accurate predictions as the RFs. However, if two cracks had to be quantified, the RFs slightly outperformed the ensemble of the ANNs. Notably, the RFs had fewer hyperparameters to tune and the training process was remarkably shorter than in the case of the ANNs.

Analysing the results of the predictions, it was found out that the depth of cracks was more difficult to predict accurately than the location. The dataset of eight DFPs produced more accurate predictions of the crack depths, but not of the crack location. This was in line with the correlation analysis, Mahmoud and Kiefa [Mahm 99], and Ndambi et al. [Ndam 02] results: the natural frequencies could follow the damage severity but were not influenced by the crack damage locations. The hypothesis on the sensitivity of the Haar wavelet transform coefficients towards the crack localisation was decisively confirmed; however, the Haar wavelet transform method could not follow the severity of the crack.

# Chapter 6

## Elastic supports

The present chapter focuses on the Euler-Bernoulli beam with elastic supports. The supports are simulated by the spring model. The inverse problem of the stiffness parameter identification is solved using the modal domain, the feed-forward back propagation neural network (ANN), the random forests (RF) and the discrete Haar wavelet transform (HWT). In particular, the first mode shape is decomposed into the Haar wavelet transform coefficients (HWT-Cs) with a small level of resolution. The obtained coefficients are used in the feature vector. In line, the machine learning methods are trained on the dimensionless natural frequency parameters (DFPs). The results of the approaches are compared to each other. The foundation for this chapter can be found in [Fekl 13b, Fekl 14].

### 6.1 Related work

Structural supports play an important role in engineering. They do not only firmly carry a structure, but are used to improve the overall constructional performance. For example, the fundamental frequency can be increased if a beam has additional internal point supports. If supports are rigid, the optimum locations of the supports are the nodal points of the highest vibration mode [Cour 66]. If supports are elastic and the stiffness parameter of the supports exceeds a certain minimum value, the optimum locations of the supports are still the same as in the case of rigid supports - no decrease in the fundamental frequency is observed [Akes 88].

Compared to the rigid supports, the elastic supports have the advantage of hardening or softening the non-linear behaviour of the structure. Furthermore, both horizontal and vertical elastic supports reduce the dynamic coefficient of dis-

placement [Liu 13]. Therefore, beams with elastic supports are frequently used in spring-beam coupled systems, cable-arch structures, fluid-conveying pipes, frames and trusses, railway tracks, towers, piles, tall buildings, robot arms and other technical applications [Wu 06, Ronu 19].

It is theoretically and practically proved that a long-term performance of supported constructions greatly depends on the stiffness parameters of their supports [Wang 06]. Due to environmental conditions or damage, the stiffness characteristics of supports can change. The decreased stiffness may lead to the collapse of the whole construction if no preventive maintenance measures are taken on time. To avoid loss of functionality or catastrophic failure, it is vital to monitor the stiffness characteristics of supports.

Different boundary conditions and supports have been analysed in a large number of papers. Most of the papers are devoted to the vibration of beams with classical boundary conditions. Fewer papers are focused on the beams with elastic supports. Some of them are [Sait 79, Glab 99, Nagu 02, Bane 04, Xant 07, Hsu 08, Silv 09, Wang 13, Lore 18]. The exact expressions for the natural frequencies and mode shapes of the beam with one end hinged and restrained by a rotational spring and the other end free were derived by Chun [Chun 72]. The effects of rotational and transversal supports at one end of the beam was studied in [Afol 86] and Lau [Lau 84]. Lau expanded Rutenbergs research on the free vibration of the uniform beams with a rotational constraint and presented a closed-form solution to the beam with rotational and translational supports at some point of the beam.

The frequency equation of the beam with an intermediate elastic support using the continuity conditions at the supported point was presented by Chellapilla [Chel 89]. Albarracin et al. [Alba 04] described the effect of an intermediate support mathematically when the ends of the beam were elastically constrained. Opposite, Rao and Mirza [Afol 86], and Li [Li 00] studied the vibrations of the beams restrained by two transverse springs and two rotational springs. The numerical results presented in the papers demonstrated that the natural frequencies and the mode shapes were sensitive to the position and stiffness of the intermediate elastic supports. The authors also stated that the stiffness parameter of the elastic supports considerably caused the first few modes shapes and was negligible on the higher frequencies.

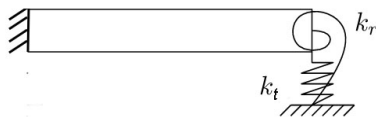
Sato et al. [Sato 08] demonstrated that a beam on equidistant elastic supports could be considered as a beam on an elastic foundation in static and free vibration problems. Nevertheless, the presented model was valid for a limited range of support stiffness, spacing and flexural rigidity of the beam. The proposed model

was suitable for simplified analysis of the global behaviour of some structures, such as floating tunnels.

The stiffness parameter identification from the governing equation of the free vibration of beams with elastic springs at the ends of the beam is an inverse problem and cannot be solved analytically. Therefore, alternative methods have to be sought. ANNs and RFs are a promising tool in the search for the relationships between the dynamic response of the beam and the corresponding stiffness parameters of elastic supports. The present chapter is focused on the Euler-Bernoulli beam with non-classical (elastic) supports. The supports are simulated by the elastic spring model. Two datasets are calculated numerically: the first eight dimensionless natural frequency parameter based dataset (DFP) and 16 Haar wavelet transform coefficient based dataset (HWTC). The HWTCs are obtained from the first mode shape. No alternative research has been found in the literature.

## 6.2 Quantification of the stiffness parameters

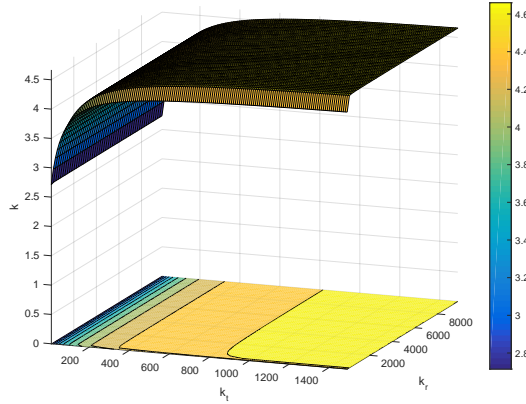
In the present simulation study, a uniform homogeneous Euler-Bernoulli beam was considered. The left end of the beam was clamped, the right end of the beam was supported by elastic supports (Figure 6.1). Different stiffness parameters of the translational spring ( $k_t$ ) and the rotational spring were investigated ( $k_r$ ).



**Figure 6.1:** A uniform homogeneous Euler-Bernoulli beam with a clamped left end and an elastically supported right end.

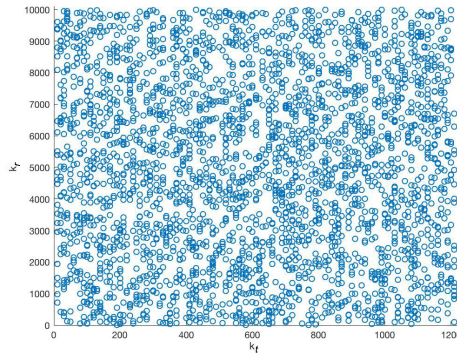
### 6.2.1 Datasets

In order to get a general understanding of the variational trend of the non-dimensional natural frequency parameters (DFPs) and the stiffness parameters of the elastic supports, more than 3000 different cases are plotted in Figure 6.2. It is seen that the stiffness parameter of the rotational spring has less influence on the first DFP than the stiffness parameter of the translational spring. The finding about the influence of the stiffness parameters on the DFP is in line with [Kim 01].



**Figure 6.2:** The first DFP in function of the translational ( $k_t$ ) and rotational ( $k_r$ ) springs.

In the present simulation study on the stiffness parameter quantification, 3000 different cases were chosen randomly (Figure 6.3). The minimum and maximum values of the stiffness parameter of the translational spring were set to 10 and 1490. The minimum and maximum values of the stiffness parameter of the rotational spring were set to 10 and 9990. The boundaries were set considering the influence of the stiffness parameters on the DFPs and practical applications of the springs.



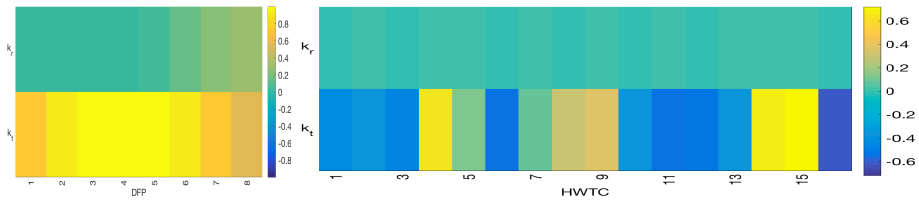
**Figure 6.3:** Distribution of stiffness characteristics.

With regard to the quantification of the crack characteristics presented in Chapter 5 (the DFPs were more sensitive to the crack depth and the HWTCs were more sensitive to the crack localisation), two sets of data were calculated: the DFP-based dataset and the HWTC-based dataset. The calculations were motivated by the assumption that the combined approach of the DFPs and the HWTCs could quantify the stiffness parameters of the springs more accurately than any particular dataset. Hereof, for the chosen cases (Figure 6.3), the first eight DFPs ( $k_i$ ,



$i = 1, \dots, 8$ ) were calculated using the equations from Subsections 3.1.1 and 3.1.2. For the second set of data, the first mode shape was transformed into 16 HWTCs using normalisation and equations (2.7) - (2.10) and taking into account the results presented in [Vika 12, Fekl 13b]. The calculation of the HWTCs was more than 20 times faster than the calculation of the DFPs.

The correlation between each DFP ( $k_i$ ) or HWTC ( $h_j$ ) and the stiffness parameters are presented in Figure 6.4. Both the DFPs and the HWTCs correlate with the stiffness parameter of the translational spring; the correlation between the DFPs or HWTCs and the stiffness parameter of the rotational spring is insignificant. It is also noted that the third DFP correlates with the stiffness parameter of the translational spring; in the case of the rotational spring, the eighth DFP (out of the first eight DFPs) correlates the most with the stiffness parameter.



**Figure 6.4:** Correlation between the stiffness parameters ( $k_t$ ,  $k_r$ ) and the DFPs (left) or the HWTCs (right).

Taking into account the results of the correlation analysis (Figure 6.4), the following datasets were formed:

**Table 6.1:** Configurations of the datasets for stiffness parameter prediction.

Set number	Feature nature	Feature coefficients
1	$k_i^2$	$i = 1, \dots, 8$
2	$k_i^2$	$i = 6, 7, 8$
3	$h_j$	$j = 1, \dots, 16$
4	$k_i^2, h_j$	$i = 1, j = 1, \dots, 16$
5	$k_i^2, h_j$	$i = 3, j = 1, \dots, 16$
6	$k_i^2, h_j$	$i = 8, j = 1, \dots, 16$

Before providing the machine learning methods with the data, the calculated values were scaled within the range of zero and one using (5.1). Each dataset was split into two sets: the training set with 2400 records and the test set with 600 records. The comparison of different training models was made on the bases of the MSE (2.14).

## 6.2.2 Feed-forward neural networks with back propagation

In the present simulation study, the stiffness parameters of the springs were predicted by feed-forward back propagation ANNs with one hidden layer. The networks were trained using one of the training functions given in Table 2.1. Taking into account the results published in [Fekl 13b, Fekl 14], it was proposed to predict the stiffness parameter of the springs one-by-one (one output per network). The number of the hidden neurons was gradually increased from 10 to 50 with a step of 10 in order to select the most promising network structure. The differentiable transfer function in the hidden layer was Elliot sigmoid; the linear transfer function was used in the output layer. The training of the ANN was stopped when an acceptable level of error was achieved ( $MSE = 1e-4$ ), or when the number of the iterations exceeded the preset maximum ( $epoch = 1000$ ), or the number of the validation checks reached the predefined value ( $validation\_checks = 6$ ).

Tables 6.2 and 6.3 summarise the results of different trainings. Each row of the tables shows the lowest MSE of the five-fold cross-validation using a particular training function; the number of the hidden nodes are given in the parentheses.

**Table 6.2:** The lowest MSE of the five-fold cross-validation using a particular training function and dataset to predict the stiffness parameter of the translational spring  $k_t$ .

Func.	Set 1	Set 2	Set 3	Set 4	Set 5	Set 6
LM	6e-7(10)	3e-4(20)	3e-4(20)	4e-4(10)	3e-6(50)	1e-5(10)
SCG	3e-4(10)	8e-4(10)	1.4e-3(30)	7e-4(20)	2e-4(30)	6e-4(10)
RP	7e-4(20)	6e-4(50)	7e-4(10)	7e-4(10)	5e-5(40)	1e-4(10)
BFGS	2e-4(10)	6e-4(40)	6e-4(50)	6e-4(50)	7e-5(40)	9e-5(10)
BR	<b>5e-8(20)</b>	3e-4(40)	1e-4(10)	3e-4(20)	5e-7(30)	1e-5(40)

**Table 6.3:** The lowest MSE of the five-fold cross-validation using a particular training function and dataset to predict the stiffness parameter of the rotational spring  $k_r$ .

Func.	Set 1	Set 2	Set 3	Set 4	Set 5	Set 6
LM	2.22e-2(50)	2.5e-3(50)	8.32e-2(10)	8.29e-2(10)	6.82e-2(40)	2.08e-2(50)
SCG	5.29e-2(30)	5.01e-2(10)	8.36e-2(10)	8.35e-2(10)	8.39e-2(10)	7.12e-2(20)
RP	4.70e-2(30)	3.01e-2(50)	8.37e-2(10)	8.38e-2(40)	8.36e-2(20)	6.14e-2(40)
BFGS	3.84e-2(40)	1.81e-2(40)	8.30e-2(40)	8.34e-2(20)	8.05e-2(30)	5.10e-2(40)
BR	4.4e-3(10)	<b>1.1e-3(10)</b>	8.24e-2(20)	8.17e-2(30)	6.34e-2(20)	8.4e-3(20)

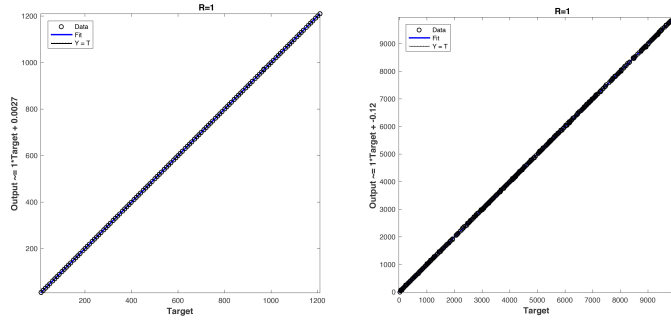
According to the results, the stiffness parameter of the rotational spring was more challenging to predict than the stiffness parameter of the translational spring. The most accurate predictions of the stiffness parameter of the translational spring were made by the ANNs with 20 hidden nodes trained by the Bayesian regularisa-

tion. If the ANN was provided with the first eight DFPs (dataset 1), an average MSE was  $5e-8$  and the R-value was 1.00. The most accurate predictions of the stiffness parameter of the rotational spring were made by the ANN with ten hidden neurons trained by the Bayesian regularisation using the sixth, seventh and eight DFPs (dataset 2). The MSE of the five-fold validation was  $1.1e-3$  and the R-value was  $9.934e-1$ .

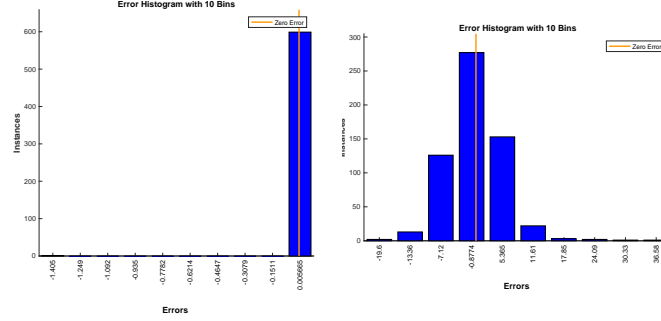
Furthermore, the results in Table 6.2 indicated that the combination of the third DFP and 16 HWTCs (dataset 5) and the ANN with ten hidden neurons trained by the Bayesian regularisation also produced quite accurate results on the stiffness parameter of the translational spring (MSE was  $5e-7$  and the R-value was 1.00). The other results based on the HWTCs or a combination of the HWTCs and DFPs were around  $e-4$  or  $e-5$ . According to Table 6.3, the combination of the eighth DFP and 16 HWTCs (dataset 6) and the ANN with 20 hidden nodes trained by the Bayesian regularisation produced relatively accurate results on the stiffness parameter of the rotational spring in comparison with other combinations of the DFPs and the HWTCs (MSE was  $8.4e-3$  and the R-value was  $9.482e-1$ ). The other results based on the HWTCs or a combination of the HWTCs and DFPs were around  $e-2$ . The observations tied in the correlation analysis (Figure 6.4).

Next, two of the most promising ANNs trained by the Bayesian regularisation were merged into a complex approach and examined on the test set with 600 records. The first ANN predicted the stiffness parameter of the translational spring. The ANN had 20 hidden nodes; it was trained on the records which contained eight DFPs. The second ANN predicted the stiffness parameter of the rotational spring. The ANN had ten hidden nodes; it was provided with the records which contained the sixth, seventh and eighth DFPs. The results are shown in Figure 6.5. For clarity and descriptive reasons, the stiffness parameters are shown in the unscaled format. In the case of the stiffness parameter of the translation spring, the R-value was 1.00. The absolute error was less than 0.006 in 600 cases. In the case of the stiffness parameter of the rotational spring, the R-value was 1.00. The absolute error was less than 20 in 593 cases.

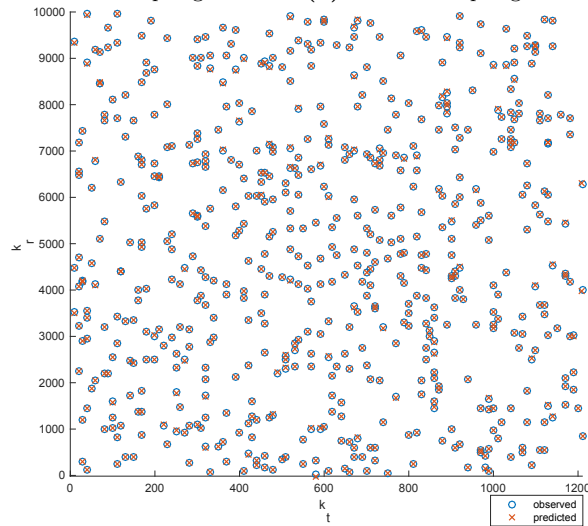
For the comparison, Figure 6.6 shows the unscaled results of the predictions based on the combined data of the DFP and HWTCs. The predictions were made by the ANN trained by the Bayesian regularisation. In the case of the translational spring, the ANN had ten hidden neurons; it was provided with the testing data formed according to dataset 5. The R-value was 1.00, and the absolute error was less than 0.5 in 592 cases. In the case of the rotational spring, the ANN had 20 hidden neurons; it was provided with the testing data formed according to dataset 6. The R-value was  $9.7568e-1$ , and the absolute error was less than 80 in 368 cases.



(a) Translational spring stiffness. (b) Rotational spring stiffness.

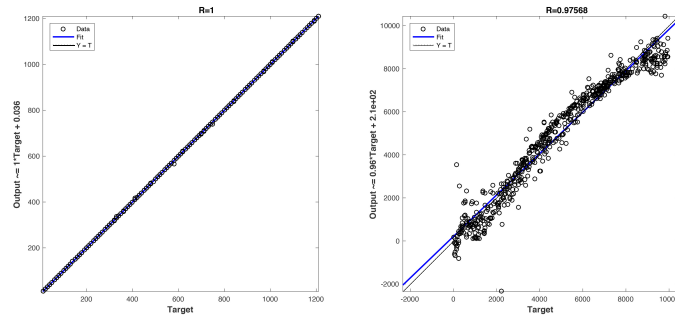


(c) Translational spring stiffness. (d) Rotational spring stiffness.

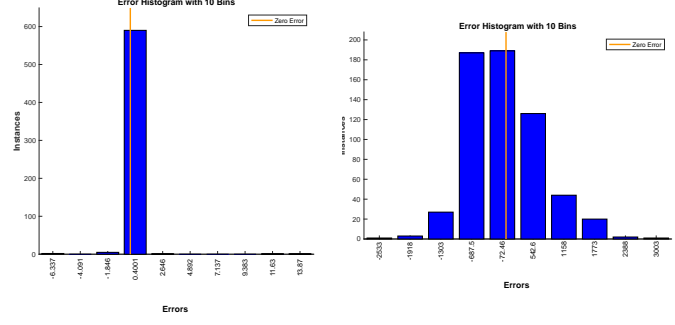


(e) Observed and predicted stiffness parameters of the translational ( $k_t$ ) and rotational ( $k_r$ ) springs.

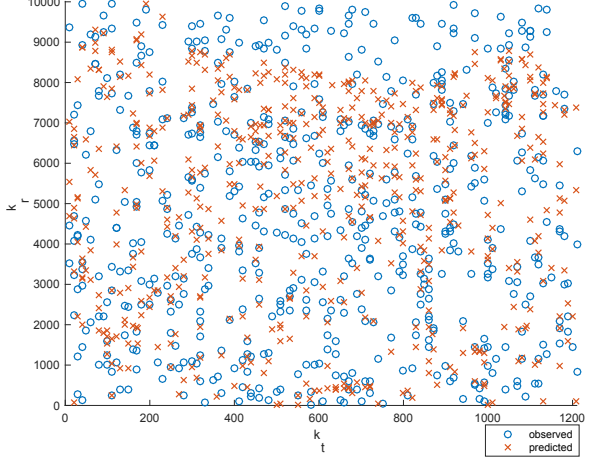
**Figure 6.5:** The results of the ANNs trained to predict stiffness parameters of the translational ( $k_t$ ) and rotational ( $k_r$ ) springs using the DFPs.



(a) Translational spring stiffness. (b) Rotational spring stiffness.



(c) Translational spring stiffness. (d) Rotational spring stiffness.



(e) Observed and predicted stiffness parameters of the translational and rotational springs.

**Figure 6.6:** The results of the ANNs trained to predict stiffness parameters of the translational ( $k_t$ ) and rotational ( $k_r$ ) springs using the HWTCs.

In comparison with the results presented in [Fekl 13b, Fekl 14], the HWTCs did not produce accurate predictions of the stiffness parameters of the springs. The reasons could be seen in the scope of the task. In the previous articles, the rotational spring parameter was fixed to a particular value ( $k_t = 10$ ). In the present simulation study, the stiffness parameter of both springs was predicted sequentially.

### 6.2.3 Random forest

Next, the previous simulation study was examined using the RFs. The following RF configurations were considered:

- the number of predictors in samples (8 in dataset 1, 3 in dataset 2, or 16 in dataset 3, or 17 in datasets 4, 5, 6);
- the number of predictors without replacement in samples  $p$  (1/6, 1/2 and 2/3 of the predictors in the pattern or all);
- the number of trees (10, 20, 30, 40, 50, 75, 100, 150, 200, 250, 300, 400, 500, 750, 1000).

The five-fold cross-validation was conducted on the datasets described in Table 6.1. Each set contained 2400 records. Table 6.4 shows the MSE and the corresponding RF configuration which produced the lowest error.

**Table 6.4:** The lowest MSE and the configuration of the corresponding RF provided with a particular dataset to predict the stiffness parameters of the translational and rotational springs.

Parameter	Dataset	Predictors in a pattern	$p$	Nr of trees	MSE
$k_t$	dataset 1	8	6	50	<b>5e-6</b>
	dataset 2	3	3	150	8e-4
	dataset 3	16	11	200	2e-4
	dataset 4	17	8	100	2e-4
	dataset 5	17	17	10	1e-5
	dataset 6	17	17	400	1e-4
$k_r$	dataset 1	8	8	150	<b>1.5e-3</b>
	dataset 2	3	3	200	2.2e-3
	dataset 3	16	16	50	1.54e-2
	dataset 4	17	17	300	1.5e-2
	dataset 5	17	17	250	1.34e-2
	dataset 6	17	17	1000	3.2e-3

Similar to the results produced by the ANNs, the stiffness parameter of the rotational spring was harder to predict than the stiffness parameter of the translational spring. Also, the DFP-based dataset produced the most promising results. The accuracy of the stiffness parameter predictions was  $MSE = 5e-6$ ,  $R = 9.999e-1$  for the translational spring and  $MSE = 1.5e-3$ ,  $R = 9.912e-1$  for the rotational spring. The corresponding predictions based on the combination of the HWTCs and the DFP were  $MSE = 1e-5$ ,  $R = 9.999e-1$  (dataset 5) and  $MSE = 3.2e-3$ ,  $R = 9.817e-1$  (dataset 6). The results tied in the correlation analysis (Figure 6.4): the third DFP correlated the most with the stiffness parameter of the translational spring and the eighth DFP correlated the most with the stiffness parameter of the rotational spring.

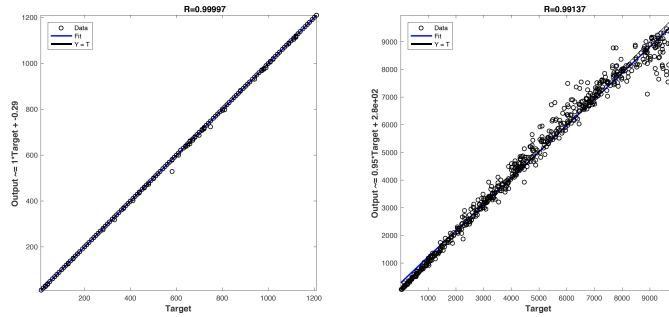
Next, two of the most promising RFs were merged into a complex approach and examined on the test set with 600 records. The first RF was trained on the records which contained eight DFPs. The second RF was provided with the records which contained the sixth, seventh and eighth DFPs. The results are shown in Figure 6.7. For clarity and descriptive reasons, the stiffness parameters are shown in the unscaled format. In the case of the stiffness parameter of the translation spring, the R-value was  $9.999e-1$ , and the absolute error was less than 2 in 583 cases. In the case of the stiffness parameter of the rotational spring, the R-value was  $9.991e-1$ , and the absolute error was less than 151 in 187 cases.

For the comparison, Figure 6.8 shows the unscaled results of the predictions based on the combined data of the DFP and HWTCs. In the case of the translational spring, the RF was provided with the testing data formed according to dataset 5. The R-value was  $9.999e-1$ ; the absolute error was less than 2.2 in 583 cases. In the case of the rotational spring, the RF was provided with the testing data formed according to dataset 6. The R-value was  $9.820e-1$ ; the absolute error was less than 200 in 217 cases.

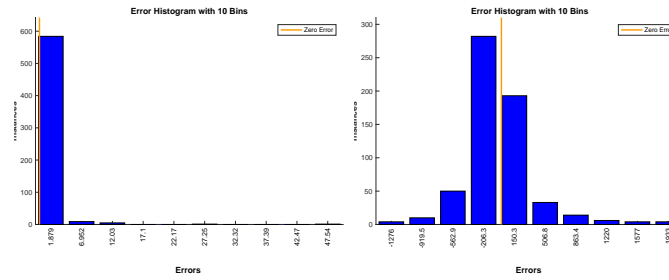
### 6.3 Discussion and conclusions

A large number of studies are focused on the Euler-Bernoulli beams with classical boundary conditions. From the viewpoint of engineering, elastic boundary supports are more significant and practical. Motivated by such limitation, the Euler-Bernoulli beam resting on elastic supports were investigated in the present chapter. The supports were simulated by the elastic spring model.

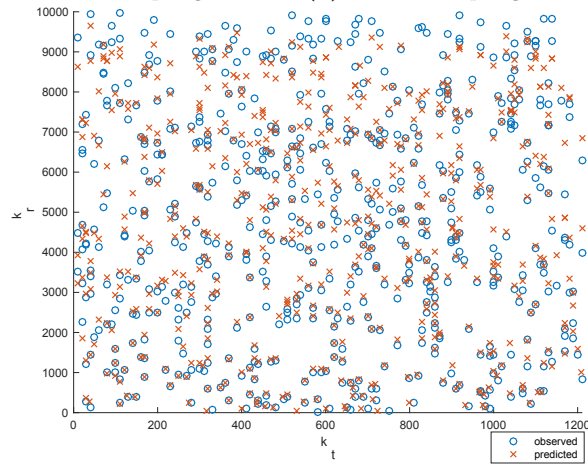
The solution procedure for predicting the stiffness parameters of the elastic supports was developed by generalising the procedure described in the previous



(a) Translational spring stiffness. (b) Rotational spring stiffness.



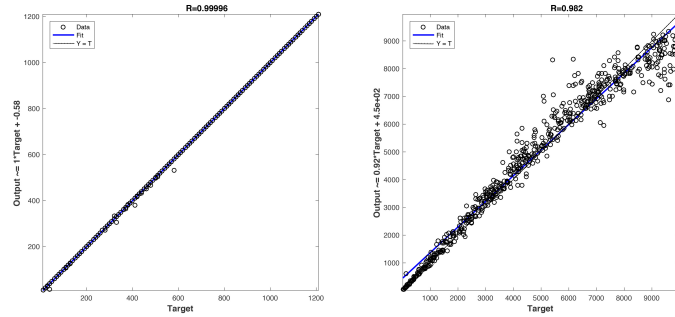
(c) Translational spring stiffness. (d) Rotational spring stiffness.



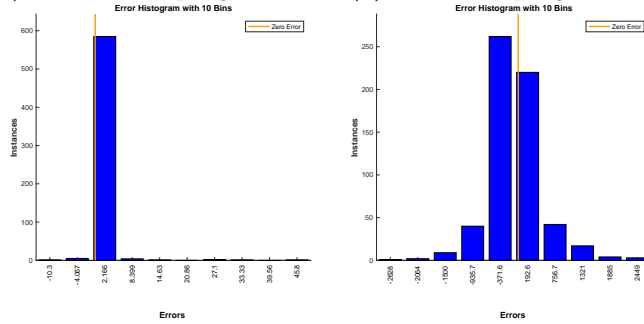
(e) Observed and predicted parameters of the translational and rotational stiffness parameters.

**Figure 6.7:** The results of the RF trained to predict stiffness parameters of the translational ( $k_t$ ) and rotational ( $k_r$ ) springs using the DFPs.

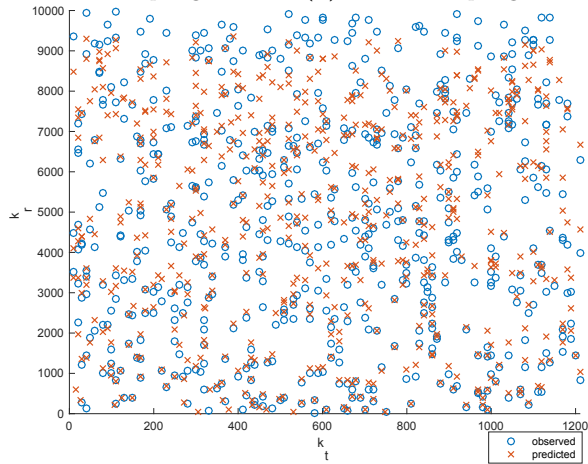




(a) Translational spring stiffness. (b) Rotational spring stiffness.



(c) Translational spring stiffness. (d) Rotational spring stiffness.



(e) Observed and predicted parameters of the translational and rotational stiffness parameters.

**Figure 6.8:** The results of the RF trained to predict stiffness parameters of the translational ( $k_t$ ) and rotational ( $k_r$ ) springs using the HWTCs.

chapter. The solution was based on the DFPs and the first mode shape decomposition into the HWTCs. The elastic parameters of the supports were predicted by the ANNs and the RFs.

The simulation study indicated that the stiffness parameter of the rotational spring was more harder to predict than the stiffness parameter of the translational spring. The results of the predictions showed that the overall efficiency of the predictions based on the DFPs was substantially higher (over  $e^{-5}$ ) and the identified parameters were similar to the expected ones than the results based on the HWTCs. Hereof, the hypothesis on the sensitivity of the Haar wavelet transform coefficients towards the stiffness parameters was not confirmed. This could be explained by the fact that the HWTCs had a low correlation with the stiffness parameter of the springs.

# Chapter 7

## Point mass

The inverse problem of determining the location and mass ratio of a concentrated point mass attached to the homogeneous Euler–Bernoulli beam is considered in this chapter. Under the assumption that the size of a point mass is small compared to the total mass of the beam, it is shown that the problem can be solved in terms of point-mass-induced changes in the natural frequencies or mode shapes. The predictions of the point mass location and mass ratio are made by the artificial neural networks (ANNs) or the random forests (RFs). The dimensionless natural frequency parameters (DFPs) or the first mode shape transformed into the Haar wavelet transform coefficients (HWTCS) are used at the inputs of the machine learning methods. The foundation for this chapter laid [Hein 09].

### 7.1 Related work

Effective methods for timely identification of concentrated point masses on vibrating beams is an issue of increasing interest in several fields, such as electronics, aerospace, naval engineering. Some applications with an attached mass to a vibrating beam are plane wings with a turbine, slabs supporting engines or motors which are not directly accessible from the exterior. Apart from the applications, many engineering simulations require numerical computations to describe the behaviour of the structures carrying their own weight and imposed loading. Such simulations help analyse the influence of concentrated masses on the resonant frequencies of beams.

Numerous papers have been published on the exact and approximate analyses of the concentrated mass and vibrating systems. The problem of a vibrating

simply supported beam carrying a concentrated mass at its centre was solved analytically by Chen [Chen 63] using the method of the frequency determinant. It was, however, claimed that, with this method, the number of the beam equations increased as the number of the attached masses increased. The eigenfunction of the beam-mass systems was obtained by satisfying the differential equation of motion and by imposing the corresponding boundary and compatibility conditions associated with the masses by Rosa et al. [Rosa 96]. The Laplace transformation technique was used to formulate the frequency equation for elastically restrained beams carrying intermediate concentrated masses by Liu et al. [Liu 88]. Laura et al. [Laur 83] used polynomial coordinate functions to study continuous beams subjected to the axial forces and carrying concentrated masses. Hamdan et al. [Hamd 94] compared the results of the exact solution with the Rayleigh-Ritz method, the Galerkin method and the FEM. The comparison showed that the FEM was preferable due to numerical stability, accuracy and convergence rate for small attached inertia values.

Extensive research on determining the natural frequencies of vibrating beams and plates with attached loading was conducted by Low. He derived two analytical expressions using eigenfunctions and Rayleigh's method [Low 93, Low 97c]. The methods were compared to each other in [Low 03]. Low concluded that the Rayleigh method with simple shape functions could provide good approximation and thus could replace solving the eigenfrequency equations. The time saving by using Rayleigh's method became more significant as the number of masses carried by the beam increased. Low [Low 94] also presented the research on an equivalent-center method for obtaining the frequencies of the loaded beams. The method was complemented with the use of the strain energy and the stiffness ratios [Low 01]. The Rayleigh-Ritz method was used in the studies on rectangular plates and beams carrying a concentrated mass [Low 97a, Low 97b, Low 98]. Low et al. presented both experimental and theoretical results and showed that the correlation between theory and experiments was much improved when the stretching effect was considered. In the latest research on the beam system carrying a single mass, Low calculated the eigenvalues by virtue of Dunkerley's formula [Low 00].

A large number of research papers propose machine learning methods for predicting the natural frequencies of beams and plates carrying a point mass (a non-inverse problem). The basic idea in such vibration-based machine learning approaches relies on the fact that the vibration-based parameters depend on the physical properties of the system structures. Changes in the mass ratio and location result in detectable alterations in the natural frequencies, displacements or mode shapes. Özkaya and Pakdemirli [Ozka 99] used a feed-forward back propa-

gation ANN, the mass ratio and the location of the point mass to predict the first five natural frequencies of the beam. Nikoo et al. [Niko 18] used ANNs to model the frequency of the first mode.

Many modern engineering problems require the identification of mass loading on the basis of the dynamic responses (an inverse problem). The solution uniqueness of such problems is not guaranteed; therefore, approximation methods are needed. Hosseini and Abbas [Hoss 12] studied the deflection of the clamped beams struck transversely by a mass using the linear regression and various ANNs. Material properties and geometry of the beam were selected as the independent variables of the model to predict the deflection of the beam. It was found out that a simple feed-forward back propagation network was either as good as or even slightly better than the linear regression or other sophisticated networks, such as the cascade-forward back propagation network or the radial basis function network. The analysis of the sensitivity of different variables showed that raw input variables performed better than (non-normalised) grouped variables.

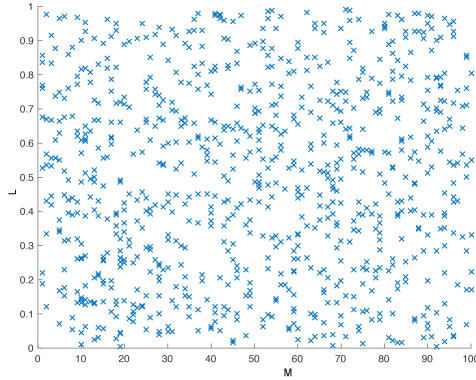
Other studies on the natural frequencies of beams and rods carrying masses can be found in [Nagu 02, Rosa 03, Su 05, Baro 15]. However, none research has been found on the concentrated point mass identification using the mode shape transformed into a set of the HWTCs. The idea of the wavelet packets and ANN-based parameter identification originates in [Hein 07]. This chapter demonstrates that both the ANNs and the RFs, and the DFPs and the HWTCs are capable of predicting the mass ratio and location of the attached concentrated point mass quite precisely.

## 7.2 Quantification of the point mass

In this simulation study, a homogeneous Euler–Bernoulli type cantilever carrying a concentrated point mass in different locations was investigated. The beam length was scaled to 1. A point mass of arbitrary mass ratio ( $M$ ) was modelled to occur at the arbitrary point of the beam ( $L$ ).

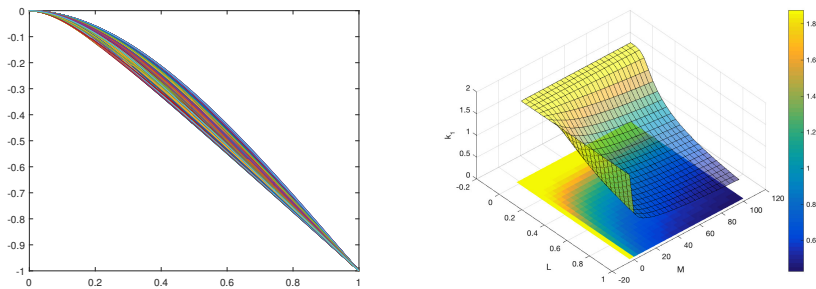
### 7.2.1 Datasets

For the present task, 860 different cases of a point mass placed on the cantilever were considered. The mass ratio and the location of the point mass were chosen randomly. The point mass ratios were chosen in the range from one to 100; the locations were chosen in the scaled range from 0.001 to 0.991 (Figure 7.1). The corresponding eight DFPs ( $k_i, i = 1, \dots, 8$ ) for each concentrated point mass were calcu-



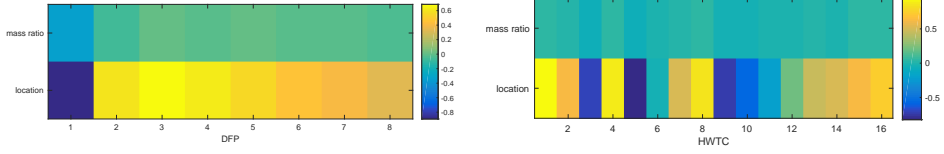
**Figure 7.1:** The dataset of the point masses.

lated using the equations from Subsection 3.1.3. Sixteen HWTCs ( $h_j, j = 1, \dots, 16$ ) were calculated using (2.7) - (2.10) and normalisation. The calculated values of the first DFPs and the mode shapes had good agreement with the results obtained by Low [Low 94]. The confirmation can also be seen in Figure 7.2 which displays the scaled first mode shape of each case and the first DFPs. The smooth graphs indicate the accuracy of the calculations. Here it should be noted that the calculation of 16 HWTCs was 22 times faster than the calculation of the first eight DFPs.



**Figure 7.2:** The scaled first mode shapes (left) and the first DFPs (right) of the dataset.

The correlation between the DFPs and the point mass ratios/locations are shown in Figure 7.3 (left); the correlation between the HWTCs and the point mass ratios/locations are shown in Figure 7.3 (right). The mass ratio hardly correlates to any feature. The point mass location closely correlates to the first DFP, or the first, fourth, fifth, eighth, ninth and sixteenth HWTCs ( $R > |0.7|$ ).



**Figure 7.3:** Correlation between point mass parameters ( $L$ ,  $M$ ) and the first eight DFPs (left) or 16 HWTCs (right).

Next, the influence of each independent parameter on the point mass quantification was analysed: each input neuron was eliminated in turns and its influence on the prediction was evaluated using the mean square error (MSE). The network architecture considered in the sensitivity analysis had one hidden layer with ten hidden neurons. The maximum value of epochs was set to 1000. The training function was Levenberg-Marquardt, the transfer function in the hidden layer was Elliot sigmoid, the linear transfer function was used in the output layer. In the test, the weights of the ANNs were set to the same initial values. The results are shown in Tables 7.1 and 7.2.

**Table 7.1:** Influence of each DFP on the point mass quantification ( $M$  - mass ratio,  $L$  - location).

	$k_1$	$k_2$	$k_3$	$h_4$	$k_5$	$k_6$	$k_7$	$k_8$
$M$	7.19e-2	1.28e-2	6.30e-3	4.00e-3	4.80e-3	9.20e-3	5.00e-3	6.40e-3
$L$	8.60e-3	1.60e-3	1.00e-4	4.00e-4	7.00e-4	6.00e-4	5.00e-4	1.00e-4

**Table 7.2:** Influence of each HWTC on the point mass quantification ( $M$  - mass ratio,  $L$  - location).

	$h_1$	$h_2$	$h_3$	$h_4$	$h_5$	$h_6$	$h_7$	$h_8$
$M$	7.00e-2	7.39e-2	7.42e-2	7.6e-2	6.35e-2	9.45e-2	7.38e-2	7.42e-2
$L$	2.10e-5	2.01e-6	4.22e-5	8.83e-6	4.94e-5	5.18e-5	4.09e-5	4.46e-5
	$h_9$	$h_{10}$	$h_{11}$	$h_{12}$	$h_{13}$	$h_{14}$	$h_{15}$	$h_{16}$
$M$	6.97e-2	7.97e-2	7.86e-2	7.60e-2	8.18e-2	7.03e-2	7.69e-2	6.48e-2
$L$	2.00e-5	3.94e-5	2.62e-5	8.07e-6	3.83e-5	3.57e-6	1.89e-5	3.12e-5

The results showed that the first DFP played an important role in the point mass quantification - if the first DFP was eliminated from the input feature vector, the prediction error increased. This observation coincided with the correlation analysis (Figure 7.3). Concerning the HWTCs, the sixth coefficient fluctuated the predictive accuracy of the point mass.

Since the results of the analysis were slightly different, the machine learning methods were examined on the datasets described in Table 7.3.

**Table 7.3:** Configurations of the datasets for the point mass prediction.

Set number	Parameter to predict	Feature nature	Feature coefficients
1	M	$k_i^2$	$i = 1, 2, 6$
2	M	$k_i^2$	$i = 1, 2, 3, 4, 8$
3	M	$k_i^2$	$i = 1, \dots, 8$
4	M	$h_j$	$j = 1, 2, 3, 4, 6, 7, 8, 10, 11, 12, 13, 14, 15$
5	M	$h_j$	$j = 1, \dots, 16$
6	M	$k_i^2, h_j$	$i = 1, j = 1, \dots, 16$
7	L	$k_i^2$	$i = 1, 3, 2, 4$
8	L	$k_i^2$	$i = 1, \dots, 8$
9	L	$h_j$	$j = 1, 5, 9, 3, 4, 8$
10	L	$h_j$	$j = 1, \dots, 16$
11	L	$k_i^2, h_j$	$i = 1, j = 1, \dots, 16$

In the following machine learning tests, 860 patterns were divided into two sets: 774 patterns were used for training and 86 patterns were held back for the independent test and method evaluations. Before applying the data into the training and testing of the machine learning methods, the values were scaled within the range of zero and one.

## 7.2.2 Feed-forward neural networks with back propagation

In the present simulation study, a feed-forward back propagation ANN with one hidden layer was used. The network was trained using one of the training functions given in Table 2.1.

Taking into account the results published in [Fekl 09], the point mass parameters were predicted one-by-one (one output per network). The number of the hidden neurons was increased gradually from 10 to 50 with an increment of 10 neurons in order to select the most promising network structure. The differentiable transfer function in the hidden layer was Elliot sigmoid; the linear transfer function was used in the output layer. The training of the ANN was stopped when an acceptable level of error was achieved ( $MSE = 1e-4$ ), or when the number of the iterations exceeded the preset maximum ( $epoch = 1000$ ), or the number of the validation checks reached the predefined value ( $validation\_checks = 6$ ).

Tables 7.4 and 7.5 summarise the results of different trainings. Each row describes the network configuration which produces the lowest MSE of the five-fold cross-validation using a particular training function, the number of hidden neurons and the dataset.



**Table 7.4:** The lowest MSE of five-fold cross-validation using a particular training function, the number of hidden neurons and the dataset features to predict the mass ratio.

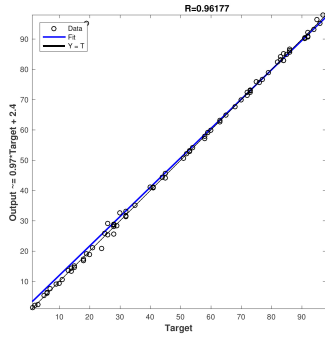
Training function	MSE	Hidden neurons	Dataset
LM	2.6e-3	10	3
SCG	2.17e-2	50	2
RP	1.64e-2	30	3
BFGS	1.82e-2	50	3
BR	<b>2.1e-3</b>	10	3

**Table 7.5:** The lowest MSE of five-fold cross-validation using a particular training function, the number of hidden neurons and the dataset features to predict the location.

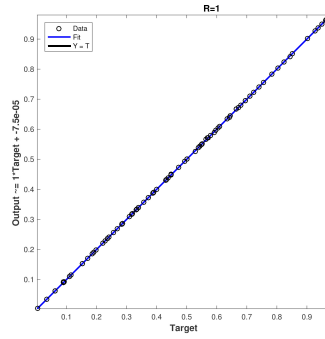
Training function	MSE	Hidden neurons	Dataset
LM	3e-6	10	11
SCG	2e-4	40	10
RP	1.64e-2	50	10
BFGS	6e-4	50	10
BR	<b>3e-7</b>	10	10

According to the results, the mass ratio was harder to predict than the point mass location. It was noted that the dataset with eight DFPs performed better on the prediction of the mass ratios ( $MSE = 2.1e-3$ ); however, the dataset of 16 HWTCs performed better on the prediction of the location ( $MSE = 3e-7$ ). An optimal network structure had ten hidden neurons and the Bayesian regularisation training function.

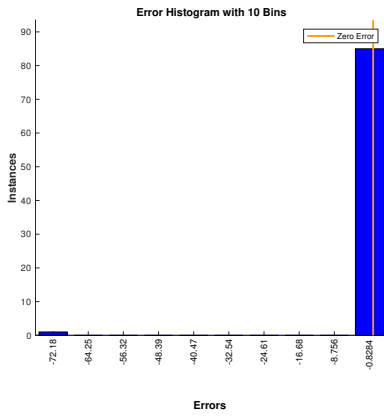
Next, two ANNs with ten hidden neurons and the Bayesian regularisation training function were examined on the set of independent data. One ANN was trained on the first eight DFPs to predict the mass ratios, and the second ANN was trained on 16 HWTCs to predict the locations of the concentrated point masses. The histogram of errors, correlation and the predicted values against the target (observed) values are plotted in Figure 7.4. For clarity and descriptive reasons, the mass ratios are shown in the unscaled format. The MSE of the point mass localisation was  $2e-7$ ; the MSE of the mass ratio quantification was  $1.6e-3$ . The R-values were 1.00 and  $9.61e-1$ , respectively. The absolute error of the point mass localisation was less than 0.0015 in 85 cases out of 86; the absolute error of the mass ratio quantification was less than 0.9 in 85 cases.



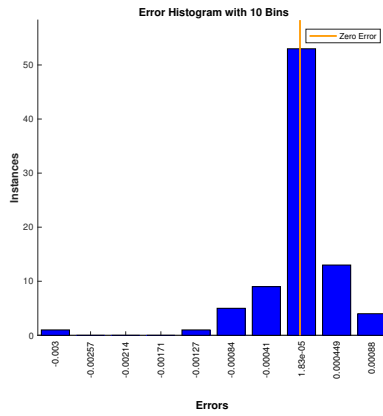
(a) Point mass ratios.



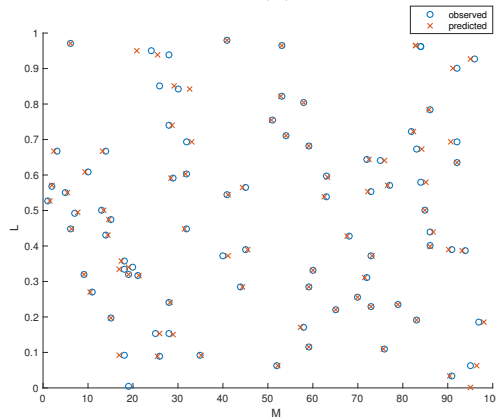
(b) Point mass locations.



(c) Mass ratio prediction.



(d) Location prediction.



(e) Predicted and target parameters of point masses.

**Figure 7.4:** Results of two ANNs trained to predict mass ratios and locations of the concentrated point masses using the DFP and the HWTCs.

### 7.2.3 Random forest

Next, the previous simulation study was examined using the RFs. The following RF configurations were considered:

- the number of predictors without replacement in samples  $p$  (1/6, 1/2 and 2/3 of the predictors in the pattern or all);
- the number of trees (25, 50, 75, 100, 150, 300, 500, 750, 1000).

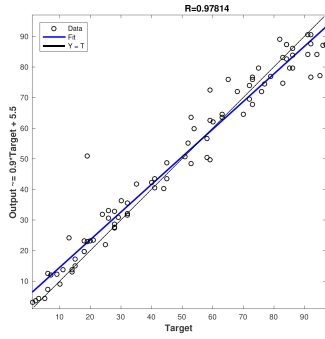
The five-fold cross-validation was conducted on the datasets described in Table 7.3. Each set contained 774 records. Table 7.6 shows the lowest MSE and the configurations of the corresponding RF.

**Table 7.6:** The lowest MSE of five-fold cross-validation to quantify point mass using the RFs and a particular dataset.

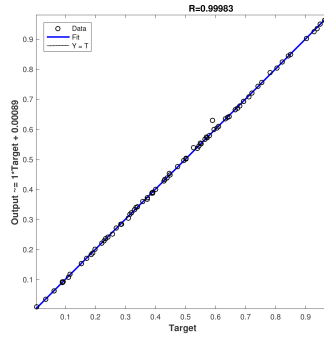
Parameter	Dataset	Predictors in a pattern	$p$	Nr of trees	$MSE$
M	DFPs	8	8	75	3.9e-3
	HWTCs	16	8	500	8.76e-2
L	DFPs	8	6	50	2e-4
	HWTCs	16	16	150	6e-6

As in the case of the ANNs, the RFs produced accurate results if they were provided either with the DFPs (dataset 3) or the HWTCs (dataset 10); the combination of the DFPs and HWTCs did not produce promising results. In the case of training on the DFPs, the lowest MSE of the point mass localisation was 2e-4; the result was obtained using an RF with 50 trees and six DFPs without replacement. The lowest MSE to estimate the mass ratios was 3.9e-3; the result was obtained using an RF with 75 trees and all DFPs without replacement. In the case of training on the HWTCs, the lowest MSE to localise the point masses was 6e-6. The result was obtained using an RF with 150 trees and all HWTCs were used at the nodes without replacement. The lowest MSE to estimate the mass ratio of the point masses was 8.67e-2 using an ensemble of 500 trees and eight HWTCs without replacement.

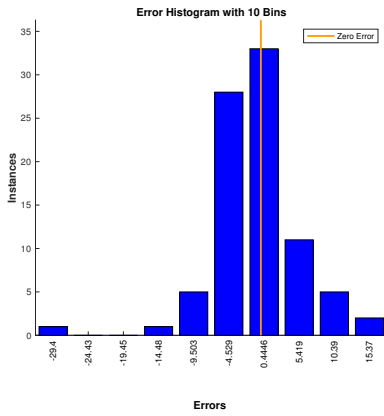
Next, two RFs were merged to form a combined approach of the DFPs and the HWTCs. Namely, the locations were predicted by the ensemble of 150 trees provided with the HWTCs, and the mass ratios were predicted by the ensemble of 75 trees provided with the DFPs. The combined approach was tested on the testing set with 84 records. The results are visualised in Figure 7.5e. The MSE of the point mass localisation was 6e-6, the R-value was 9.998e-1. The absolute



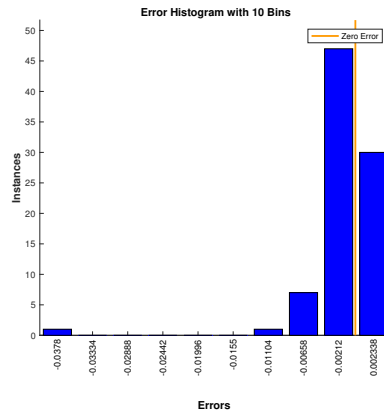
(a) Point mass ratios.



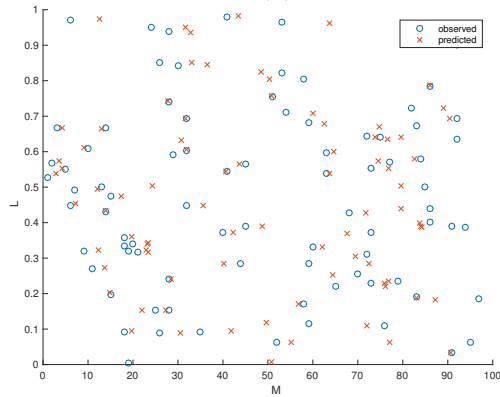
(b) Point mass locations.



(c) Mass ratio prediction.



(d) Location prediction.



(e) Predicted and target parameters of point masses.

**Figure 7.5:** The results of two ensembles of the RFs trained to predict mass ratios and locations using the DFP and the HWTCs.

error was less than 0.007 in 84 cases. The MSE of the mass ratio estimation was  $3.7e-3$ , the R-value was  $9.781e-1$ . The absolute error was less than 0.5 in 34 cases.

On the whole, as in the case with the ANNs, the RFs provided with the dataset of DFPs produced more accurate predictions of the mass ratios; meanwhile, the RFs provided with the dataset of HWTCs produced precise predictions of the locations of the concentrated point masses.

## 7.2.4 Discussion and conclusions

The development of effective methods for timely identification of a concentrated point mass on vibrating beams is an increasing interest in several fields. Motivated by the need for a fast and accurate tool for quantifying the concentrated point masses, an Euler-Bernoulli type cantilever was investigated in the present chapter.

The concentrated point mass quantification solution was based on the DFPs and the first mode shape decomposition into 16 HWTCs. The ANNs and the RFs predicted the mass ratio and location of the point masses.

According to Tables 7.4, 7.5, 7.6 and Figures 7.4, 7.5, the ANN trained by the Bayesian regularisation training function was either as good as or even slightly better than other ANNs or RFs. The results also indicated that using the HWTCs at inputs might be more beneficial for the localisation of the concentrated point masses than the DFPs. On the other hand, the DFP-based methods predicted the mass ratio of the concentrated point masses more precisely.

# Chapter 8

## Delamination

The inverse problem of determining the delamination status (location and size) in the composite non-homogeneous Euler–Bernoulli type beam is considered in this chapter. It is shown that the delamination status can be predicted using the first eight natural frequency parameters (NFPs) or the first mode shape transformed into 16 Haar wavelet transform coefficients (HWTs) by the artificial neural networks (ANNs) or the random forest (RFs). The present simulation study is a general treatment to the problems stated in [Hein 11b, Fekl 12].

### 8.1 Related work

Laminate is a type of material made of two or more layers joined by adhesive. The layers can be of the same material, such as laminated glass, plywood, or different materials, such as a sheet of glass sandwiched between plastic. In comparison to homogeneous beams, the combination of materials facilitates to get a laminate with higher stiffness properties as well as improved fatigue resistance, functional properties and durability of the structural element. Due to the advanced properties, the laminates are frequently used in mechanical, civil, marine, automotive, and other high-performance structures [Jafa 13].

Despite the multiple advantages of laminates, some materials used in the layers might be sensitive to damage. Loading, strain, stress, an impact of foreign objects, chemical corrosion, ageing, cutting or drilling may force the layers to stratify and cause delamination. Delamination is probably the most dangerous defect in composite materials [Pati 17]. It can appear suddenly without any prior notice and keep developing to collapse the structural member. Composite materials with

delamination can lose up to 60 per cent of their stiffness and remain visibly unchanged [Pati 17]. Nevertheless, the presence of a delamination in the composite structure affects its integrity as well as its mechanical properties [Luo 00].

According to Yang et al. [Yang 09], common non-destructive techniques, such as ultrasonic testing and radiography are expensive for extensive use in practice. Therefore, industries are focused on structural health monitoring (SHM) methods. The advantage of such methods is that they allow monitoring structural integrity online without dismantling structures. Some applications of the SHM methods can be found in [Yam 03, Card 04, Frit 05, Tuck 11]. This chapter is focused on one of the SHM methods which is based on the vibrations with the purpose to quantify delaminations in beams.

The vibration-based methods use a dynamic response of the structure. In the case of delamination, the local physical parameters of the structure, such as mass and stiffness are changed. These local parameters influence the modal parameters and the vibration responses of the structure.

One of the earliest models for the vibration analysis of composite beams with delaminations was proposed by Ramkumar et al. [Ramk 79]: four Timoshenko beams were connected at the delamination edges to simulate a composite beam with one through-width delamination. The obtained frequencies were consistently lower than the results of the experimental measurements. Wang et al. [Wang 82] improved the analytical solution by including the coupling between flexural and axial vibrations of the delaminated sublaminates. Using an isotropic beam with splits and the classical beam model, Wang et al. derived natural frequencies close to the experimental results. Later, Mujumdar and Suryanarayan [Muju 88] pointed out that some mode shapes computed by Wang et al. were physically unacceptable because of possible overlapping between the delaminated sublaminates. To avoid incompatibility, the sub-beams located in the delaminated region were assumed to remain close during the vibrational motion. The model was called the “constrained mode model” in contrast with the “free mode model” proposed by Wang.

Delaminations and their effects on the vibration behaviour of composite beams were investigated with the aid of the FEM in [Naga 10, Kuma 13, Jafa 13, Gowd 17]. The results showed that the natural frequencies were reduced with an increase of the delamination size; however, the natural frequencies were higher in the simply supported composite beams than in the cantilevers due to the increased bending stiffness. Also, the natural frequencies of symmetric laminates were found to be higher than of the cross-ply laminate [Gowd 17].

Yet, the FEM-based numerical simulations are popular, they are often time-consuming. If the input parameters need to be adjusted, even slightly, the simulations have to be re-done from scratch [Kono 18]. Recently, many researchers have used ANNs or genetic algorithms (GAs) and shifts in frequencies to detect various types of damage in beams. Okafor et al. [Okaf 99] trained a feed-forward back propagation neural network (FFBPANN) on the first four natural frequencies. The network had 4-10-1 neurons in its layers. The trained ANN predicted the size of the dimensionless delamination between 0.22 and 0.82 quite accurately (the error was close to zero), but underpredicted the dimensionless delamination of the size below 0.08. Chakraborty [Chak 05] trained a FFBPANN on the first ten natural frequencies. The network had 10-9-3 neurons in its layers. The trained ANN predicted the lengthwise location, size and shape of the delamination in the plate. The network could predict the delamination size and shape almost accurately with a very small error; however, the network could not precisely predict the delamination location. Adams [Adam 94] trained an FFBPANN using the first five mode shapes obtained from the modal testing; the predicted values of the axial location and size had the maximum error of 27 per cent and ten per cent, respectively, in comparison with the measured frequencies. Watkins et al. [Watk 02] trained an FFBPANN using the first five natural frequencies in the feature vector to predict the lengthwise location and size of the delaminations prescribed in the mid-plane of the cantilever (between the fourth and fifth plies). The delamination size and location predictions had an average error of 5.9 and 4.7 per cent, respectively. Krawczuk and Ostachowicz [Kraw 02] quantified delaminations in composite beams using a GA by minimising the error function which expressed the discrepancy between the measured and theoretical frequencies. It was demonstrated that the GA could predict the delamination location and magnitude at a high level of accuracy. However, in comparison to ANN, GAs-based structural damage detection required repeatedly searching from numerous damage parameters to find the optimal solution of the objective function (measured data) [Nag 02]. When the measured data and the structural damage parameters to be determined were multitudinous, the efficiency of the method was often not feasible to online damage detection of in-service structures [Yam 03].

A large number of studies investigate a single relatively large delamination in the mid-plane of the structural element. The solution is sought in the shifts of the mode shapes or natural frequencies. Yet, changes in the structural dynamic performance caused by the structural damage that is less than one per cent of the total structural size are unnoticeable [Yang 09, Yam 03, Kim 03]. Recently, the wavelet transform-based method for vibration signal analysis has been adopted in



many fields due to its time-frequency localisation. Chui [Chui 97] points out that the local singularity in the time-sequence signal can be more clearly exhibited if the signal is decomposed with the aid of the wavelet transform. When the structural vibration response signal in the time domain is decomposed into multiple sub-signals, the change corresponding to the structural damage in each sub-signal may manifest notable difference, and some of the sub-signals may possess high sensitivity to small damage in structures [Yam 03]. Therefore, the wavelet transform has been applied to the vibration-based structural damage detection by several authors [Yam 03, Yan 04, Han 05a, Zhu 06, Ruck 06a, Zhen 09]. By now, non-sufficient interest has been paid to the discrete Haar wavelet functions, which are mathematically the simplest wavelets. Chen and Hsiao [Chen 97, Hsia 99] have demonstrated that these wavelets can successfully approximate the derivatives of functions for solving differential equations. The approach has been developed further by Lepik [Lepik 05].

In the present chapter, it is proposed to apply the Haar wavelets to the first mode shape. According to several authors [Zou 00, Kim 03, Dera 08], the mode shape approach is much more sensitive to the local delaminations in comparison with the changes in natural frequencies. The ANNs or RFs are used to establish the relationship between the structural vibration response (NFPs or HWTCs) and the structural damage status. The results of the approaches are compared to each other. No similar research has been found in the literature.

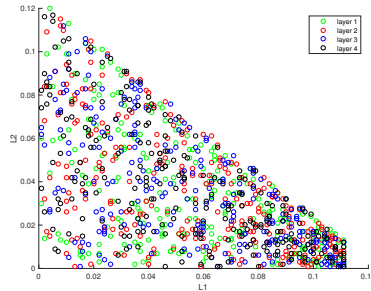
## 8.2 Quantification of the delamination

In the following simulation study, a composite cantilever made of *T300/934* graphite and epoxy with stacking sequence of  $[0^0/90^0]_{2s}$  was considered. The dimensions of the eight-ply beam were  $127 \times 12.7 \times 1.016 \text{ mm}^3$ . The material properties for the lamina were  $E_{11} = 134 \text{ GPa}$ ,  $E_{22} = 10.3 \text{ GPa}$ ,  $G_{12} = 5 \text{ GPa}$ ,  $\nu_{12} = 0.33$  and  $\rho = 1.48 \times 10^3 \text{ kg/m}^3$ . A delamination of an arbitrary length ( $L_2$ ) was modelled to occur at the arbitrary axial ( $L_1$ ) and ordinate ( $H_1$ ) locations of the beam.

### 8.2.1 Datasets

The basic idea of the present research was to establish an input-output relationship between the modal response and the delamination status using the ANNs and the RFs. To employ and compare the approaches, the vibration response of the composite beam with different delaminations was calculated considering the dimensions of the graphite/epoxy cantilever. The delamination location values from

the left end  $L_1$  varied from 0.001 to 0.111 metres; the values of the delamination extension  $L_2$  were randomly set in the range from 0.001 to 0.125 metres. Since the cantilever was vertically symmetric, only half of the cantilever layers was analysed (Figure 8.1).



**Figure 8.1:** Randomly generated delamination properties:  $L_1$  - delamination location from the left side of the beam;  $L_2$  - delamination length.

Next, 1000 sample delamination feature indexes and the first eight NFPs ( $k_i, i = 1, \dots, 8$ ) were calculated using equations from Subsections 3.2.2 and 3.2.3. The calculated values of the first NFP were compared with the ones available in literature (Table 8.1). A good agreement was observed between the results obtained in the present thesis, experiments [Shu 04a] and the FEM [Shen 90, Shu 04a].

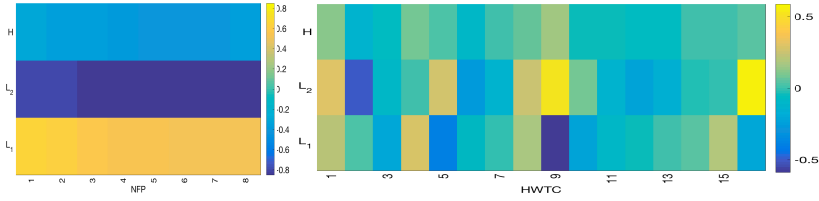
**Table 8.1:** Primary frequencies of the composite cantilever.

Delamination length (mm)	Present (Hz)	Shu, Della [Shu 04a]	Shen, Pierre [Shen 90]	Shu, Della [Shu 04a]
0.0	82.02	81.88	82.04	81.86
25.4	79.93	80.47	80.13	81.84
50.8	74.36	75.36	75.29	76.81
76.2	65.07	66.14	66.94	67.64
101.6	54.75	55.67	57.24	56.95

The HWTCs were obtained using equations from Subsections 3.2.2 and 3.2.3, normalisation and the Haar wavelet transform (2.7) - (2.10). Each record contained 16 HWTCs and the delamination status. The first mode shape was used since it was the most informative [Cao 11, Hein 11b].

According to the correlation analysis (Figure 8.2), the NFPs closely correlated ( $R > |0.7|$ ) to the extension of the delamination. The NFPs and HWTCs had a moderate correlation ( $R > |0.4|$ ) to the axial location of the delamination. A weak

correlation was observed between the NFPs or HWTCs and the ordinate location of the delamination.



**Figure 8.2:** Correlation between the delamination status and the NFPs (left) or the HWTCs (right).

Taking into account the results published in [Hein 11b], three datasets were formed. The first set of data was based on the first eight NFPs, the second dataset was based on 16 HWTCs and the third set of data was based on the first NFP and 16 HWTCs. Before training and testing the machine learning methods, all values were scaled within zero and one. The comparison of different predictive models was based on the mean square error (MSE).

## 8.2.2 Feed-forward neural network with back propagation

Comprehensive research on various homogeneous and composite beams with delaminations and different boundary conditions was published in [Fekl 12]. The investigation on the ANN architecture and training functions showed that the ANN made the most accurate predictions with ten hidden neurons trained by the Bayesian regularisation training function. The ANN were provided with eight NFPs or 16 HWTCs. The predictive model worked well if one parameter was predicted. If the ANN had to predict two parameters of the delamination status at the same time, the prediction error notably increased. Therefore, in the present simulation study on the delaminated graphite/epoxy cantilever, the problem of the formulation was solved in a slightly different way. Specifically, a chain of three independent ANNs was constructed. Each ANN predicted only one parameter: the delamination extension, the axial location and the ordinate location. The number of hidden neurons was set to ten. The differentiable transfer function in the hidden layer was Elliot sigmoid; the linear transfer function was used in the output layer. The training of the ANNs was stopped when an acceptable level of error was achieved ( $MSE = 1e-4$ ), or when the number of the iterations exceeded the preset maximum ( $epoch = 1000$ ), or the number of the validation checks reached the predefined value ( $validation\_checks = 6$ ).

The five-fold cross-validation was conducted using 850 records (150 patterns were held back for the independent test). According to the results presented in Table 8.2, the dataset of the NFPs was sensitive to the extent of the delamination (MSE = 3.2e-3, R = 9.729e-1) and its ordinate location (MSE = 8.02e-2, R = 6.889e-1). The dataset of the first NFP and 16 HWTCs quantified the axial location of the delamination more precisely (MSE = 1.2e-3, R = 9.931e-1) than the other two datasets.

**Table 8.2:** MSE of five-fold cross-validation to predict the axial location ( $L_1$ ), the ordinate location ( $H_1$ ) and the extend of the delamination ( $L_2$ ) using various datasets by ANNs.

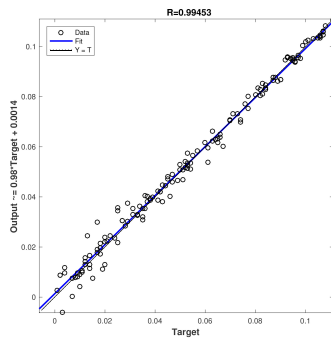
Parameter to predict	Dataset 1 (8 NFPs)	Dataset 2 (16 HWTCs)	Dataset 3 (16 HWTCs & 1st NFP)
$L_1$	5.9e-3	3.4e-3	1.2e-3
$L_2$	3.2e-3	6.8e-3	3.3e-3
$H_1$	8.02e-2	1.131e-1	9.25e-2

Following on from the results presented in Table 8.2, a chain of three ANNs was constructed and examined on the testing set of 150 records:

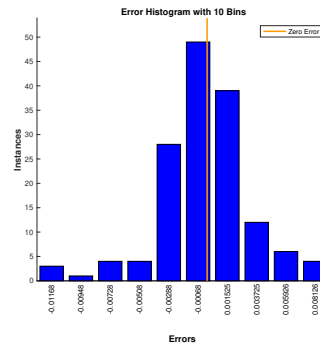
1. the delamination axial location was predicted by the ANNs provided with the records from dataset 3;
2. the delamination extent was predicted by the ANNs provided with records from dataset 3 (the choice was motivated by the computation time: despite a slightly better performance on the NFPs, the calculation of the HWTC was significantly faster than the calculation of the first eight NFPs);
3. the delamination ordinate location in the beam was predicted by the ANNs trained on the dataset 1.

The histogram of errors and correlation are plotted in Figure 8.3. For clarity and descriptive reasons, the delamination characteristics are shown in the unscaled format. The MSE of the axial localisation was 9e-4; the MSE of the delamination extent was 2.4e-3; the MSE of the ordinate localisation was 7.83e-2. The R-values were 9.945e-1, 9.816e-1 and 6.917e-1, respectively. The absolute error of the quantification of the delamination axial localisation was less than 0.012 in all 150 testing cases; the absolute error of the quantification of the delamination extent was less than 0.014 in 148 cases; the absolute error of the quantification of the ordinate location was less than 0.0003 in 150 cases.

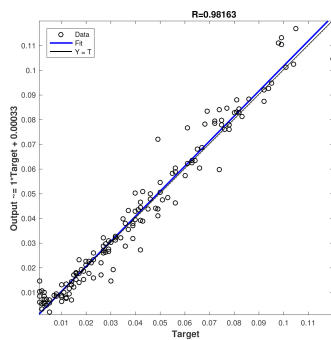
According to Figure 8.3, the extent of the delamination and its location from the left side of the cantilever was easier to predict than the ordinate location of the delamination. This could be explained by the fact that one NFP or HWTC based feature vector might correspond to different ordinate location values. Therefore, the following assumption was made: once the delamination extent was predicted, it could also be used as an input feature. In other words, in order to predict the ordinate location of the delamination, its extent and the first eight NFPs had to be identified. The assumption about improving the accuracy of the ordinate localisation prediction by adding the knowledge of the delamination extent improved the results: the MSE decreased from 7.83e-2 to 2.42e-2 (Figure 8.3 (g) and (h)). An assumption about improving the accuracy of the ordinate localisation prediction by adding the knowledge of the delamination axial location was disproved: MSE = 6.53e-2, R = 7.540e-1 (Figures 8.3 (i) and (j)).



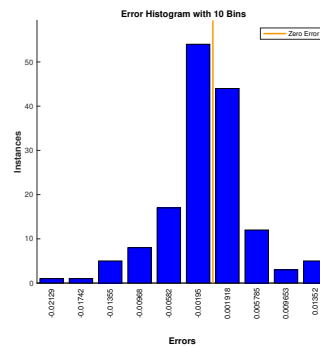
(a)



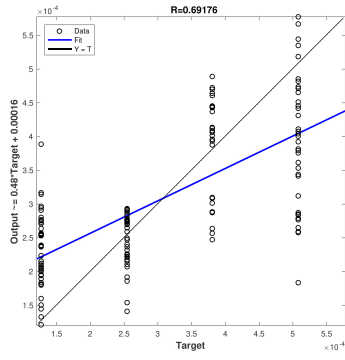
(b)



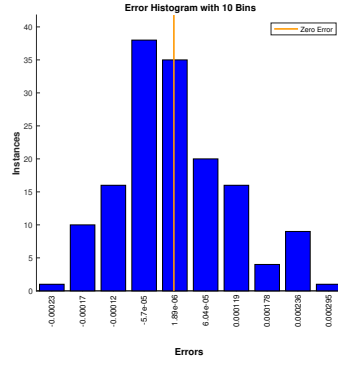
(c)



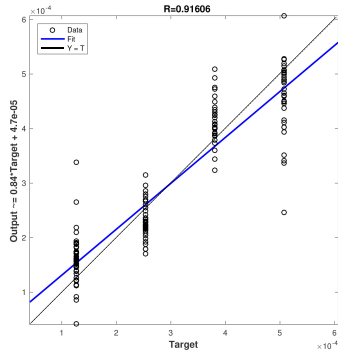
(d)



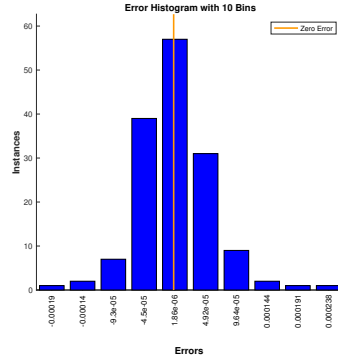
(e)



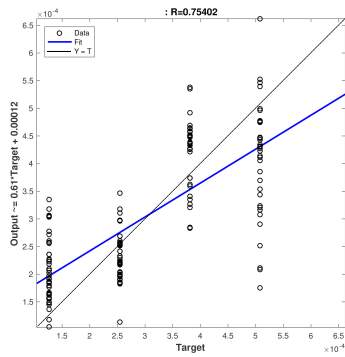
(f)



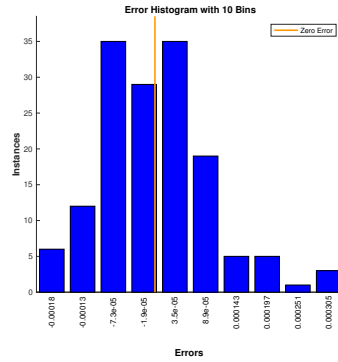
(g)



(h)



(i)



(j)

**Figure 8.3:** Correlation and error distribution of the predicted delamination statuses by the ANNs: (a)-(b) axial location; (c)-(d) delamination length; (e)-(f) ordinate location; (g)-(h) delamination ordinate location predicted with the additional input feature  $L_2$ ; (i)-(j) delamination ordinate location predicted with the additional input feature  $L_1$ .

### 8.2.3 Random forest

Next, the previous simulation study was examined using the RFs. The following RF configurations were considered:

- the number of predictors in samples (eight NFPs or 16 HWTCs or 17 which are NFP and 16 HWTCs);
- the number of predictors without replacement in samples  $p$  (1/6, 1/2 and 2/3 of the predictors in the pattern or all);
- the number of trees (25, 50, 75, 100, 150, 300, 500, 750, 1000).

The most promising results are shown in Table 8.3. Each row of the table shows the MSE of the five-fold cross-validation and the configurations of the corresponding RFs. The common tendency of the delamination status quantification by the RFs was similar to the ANNs. The dataset based on 16 HWTCs and the first NFP produced more precise results on the delamination size (MSE = 1.2e-3, R = 9.899e-1) and its axial location (MSE = 5.946e-4, R = 9.967e-1); while the dataset based on the first eight NFPs produced more accurate results on the delamination ordinate location (MSE = 7.35e-2, R = 7.183e-1).

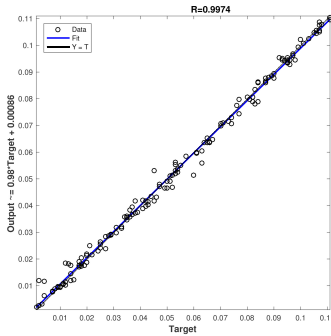
**Table 8.3:** The lowest MSE of five-fold cross-validation to predict delamination status by RFs.

Parameter	Dataset	Predictors in a pattern	$p$	Nr of trees	<i>MSE</i>
$L_1$	dataset 1	8	5	25	9e-4
	dataset 2	16	8	25	7e-4
	dataset 3	17	9	75	<b>5e-4</b>
$L_2$	dataset 1	8	5	25	1.9e-3
	dataset 2	16	16	25	3.4e-3
	dataset 3	17	17	50	<b>1.2e-3</b>
$H_1$	dataset 1	8	4	500	<b>7.35e-2</b>
	dataset 2	16	16	150	9.45e-2
	dataset 3	17	17	100	7.92e-2

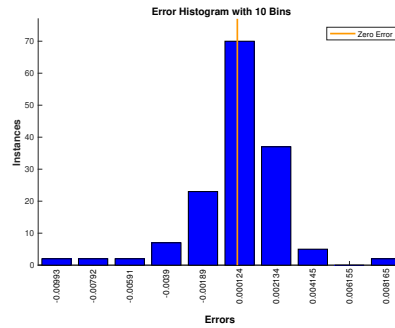
Three of the most promising RFs were merged to form a combined approach of the NFPs and the HWTCs. The results of predicting 150 test delaminations are plotted in Figure 8.4. The axial location of the delaminations was predicted by the ensemble of 75 trees trained on the HWTCs and the first NFP. The MSE was 4e-4, the R-value was 9.974e-1 and the absolute error was less than 0.009 in 149 cases. The length of the delaminations was predicted by the ensemble of 50 trees using the HTWTCs and the first NFP. The MSE was 1.2e-3, the R-value was

9.903e-1, and the absolute error was less than 0.009 in 145 cases. The ordinate location of the delaminations was predicted by the ensemble of 500 trees using the NFPs. The MSE was 7.34e-2, the R-value was 7.198e-1, and the absolute error was less than 0.009 in 148 cases.

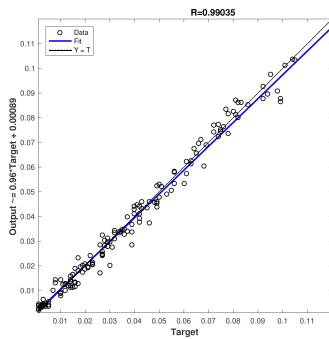
Figure 8.4 (g)-(j) were based on the assumption about improving the prediction accuracy of the delamination ordinate locations by adding the knowledge of the delamination axial location or its length. As in the case with the ANNs, the knowledge of the delamination axial location did not improve the accuracy of the predictions. If the length of the delamination was added into the feature vector, the accuracy increased significantly. The MSE decreased from 7.34e-2 to 3.72e-2. The absolute error was less than 0.0002 in 150 cases.



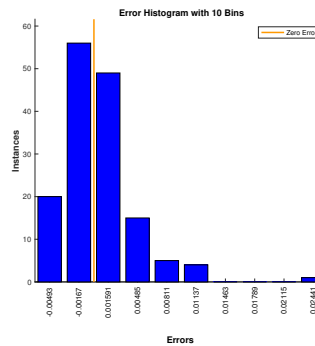
(a)



(b)

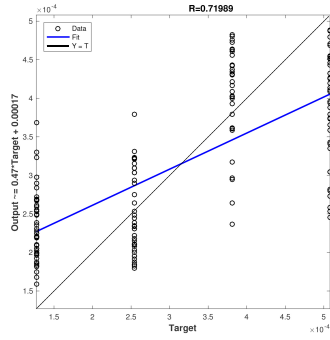


(c)

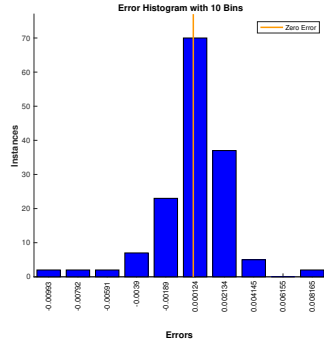


(d)

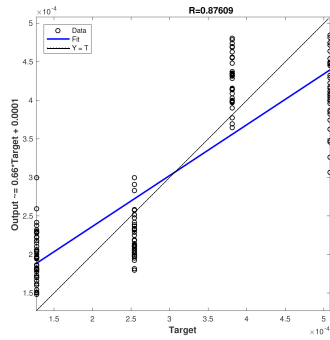




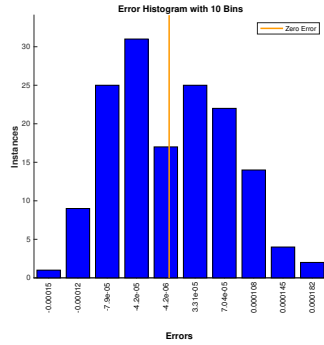
(e)



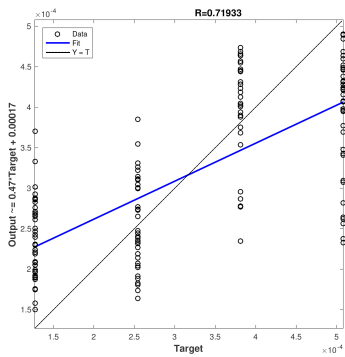
(f)



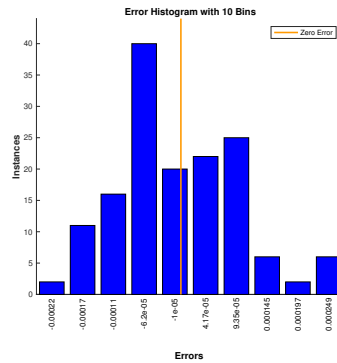
(g)



(h)



(i)



(j)

**Figure 8.4:** Correlation and error distribution of the predicted delamination statuses by the RFs: (a)-(b) axial location; (c)-(d) delamination length; (e)-(f) ordinate location; (g)-(h) delamination ordinate location predicted with the additional input feature  $L_2$ ; (i)-(j) delamination ordinate location predicted with the additional input feature  $L_1$ .

### 8.3 Discussion and conclusions

Delamination is internal damage that is not visible from the outside. Nevertheless, the presence of delamination in the laminate reduces the stiffness of the structure, its strength and the natural frequencies. Therefore, the development of effective methods for timely identification of the delamination is very actual.

In the present chapter, the Euler-Bernoulli composite cantilever was investigated for delamination quantification. In comparison to [Hein 11b], the Haar wavelet transform and machine learning methods were extended to a more complex inverse problem - delamination localisation (lengthwise and height-wise) and its extension. The five-fold cross-validation revealed that the delamination axial localisation and its extension were more precisely predicted if the feature vector contained both the first NFP and 16 HWTCs. However, the delamination ordinate localisation was more precisely predicted if the feature vector contained eight NFPs. The prediction of the delamination ordinate localisation could be improved if the feature vector contained the value of the delamination extent.

On the whole, the NFPs/HWTCs and machine learning allowed fast and accurate predictions of the delamination status even if the delamination size was less than one per cent of the beam length. Noteworthy, the RFs were capable of learning the information regarding the induced delamination in the laminate notably better than the ANNs.

# Chapter 9

## Conclusion

As one of the oldest structural elements, beams are widely used in many different fields of engineering. Hereof, modelling the dynamic behaviour of intact and damaged beam type structures is a vast subject. The present thesis focuses on the Euler–Bernoulli type beams since it is the oldest and yet widely used theory about slender beams.

The interest in detecting and quantifying damage at the earliest possible stage is pervasive throughout civil and military engineering. Visual or localised experimental methods, such as magnetic field methods, radiography, or thermal field methods require the structural element of the inspection to be readily accessible. The requirement cannot always be met if the structure is complex and the element is mounted. The need for quantitative global damage detection methods has led to the research and development of methods that examine changes in the vibration characteristics of the structure. The basic idea behind this technology is that the modal parameters (natural frequencies, mode shapes and modal damping) are functions of the physical properties of the structure (mass and stiffness). Changes in the physical properties cause detectable changes in the modal properties.

The present thesis provided new insight into the non-inverse and inverse problems of the free vibration of intact and damaged beams with classical and elastic boundary conditions as a key step of the damage quantification problem. The partial differential equations of the vibrations were solved using analytical approximate methods. It was demonstrated that the dynamic response of the intact beams could be calculated using the Haar wavelet integrations. The numerical examples indicated that the proposed approach was simple, fast and accurate. The relative error was less than 0.1 per cent if the level of resolution was equal to six ( $J = 6$ ).

Further investigation of the approach carried by Majak [Maja 18, Kirs 18] revealed even more accurate results on the vibration analysis proposing the higher-order Haar wavelet method.

The second part of the thesis concerned the problems where the desired response, such as the mode shapes and the natural frequency parameters of the system were known (calculated numerically), but the damage parameters were unknown - the inverse problems. These problems were difficult to solve since a unique solution was rarely possible. Therefore, alternative computational solutions had to be sought. In the present thesis, different types of damage (cracks, delaminations, mass points, stiffness coefficients in elastic supports) in the Euler-Bernoulli type beams were quantified. The algorithm of the damage quantification involved the calculation of datasets and tuning the machine learning methods. To generate the datasets, the governing vibration equation of the beam had to be solved (the natural frequency parameter based dataset), and the mode shapes transformed into the Haar wavelet transform coefficients (the Haar wavelet transform coefficient based dataset). Damage characteristics (location and severity) were predicted by the feed-forward back propagation neural networks or the random forests. The neural networks were chosen since they were proven to be effective mapping tools for various problems; however, the random forests were chosen since they had fewer hyperparameters to tune. Multiple simulation cases indicated that

- the Haar wavelet transform coefficient based dataset could be more than ten times faster obtained than the natural frequency parameter based dataset;
- the Haar wavelet transform coefficients were more sensitive to the damage location quantification, while the natural frequency parameters were more sensitive to the damage severity quantification (Table B1 in Appendix B);
- in most cases, the artificial neural networks made as precise predictions as the random forests; an exception was the quantification of the stiffness parameters in the elastic supports: the neural networks made significantly more precise predictions than the random forests (Table B1 in Appendix B).

At large, the proposed approach of the machine learning, the modal data and the Haar wavelets can be referenced as an alternative method for vibration analysis and damage quantification; it can be used in further theoretical non-inverse and inverse problem applications or be applied in the diagnostics of damaged beams. That is, architects and practitioners can use the described approach in modelling and simulations on the structural elements.

## Future directions

A systematic approach for vibration analysis and damage quantification in beams was in focus in the present thesis. The approach was based on the Haar wavelets: integrals and transform. Multiple simulation studies on intact and damaged beams showed accurate results. Nevertheless, a further comparative study on the mainstream methods in engineering could give a clear picture of the advantages and limitations of the method.

The combined approach of the modal data, Haar wavelets and machine learning produced accurate results on quantification of various types of damage: open cracks, elastic supports, a concentrated point mass and delamination. As future work, the proposed approach could be applied to the investigation of other structural elements (I-beams, T-beams, rods, ties, shells, plates), material constitutive models (elastic-plastic or plastic models), and types of damage (breathing cracks, subsurface cracks, transverse cracks, necks, debonding, faults, fractures). As a starting point, the following research papers on the Timoshenko beam model, buckling and nano-cracks [Hein 12a, Hein 12b, Hein 19b] could be used (the papers were not discussed in the present thesis).

A comparative study of damage detection methods based on laboratory tests of two cracked beams conducted by Ndambi et al. [Ndam 02] showed that the natural frequencies could follow the damage severity, but were not influenced by the crack damage locations; the modal assurance criterion was, in contrast, less sensitive to crack damage compared with the natural frequencies; the coordinate modal assurance criterion could localise damage in the beams, but could not follow severity; the damage indices method based on the strain energy appeared to be more precise than the other methods in damage localisation, but the difficulty remained when the damage was spread out over a certain length of the beam. Hereof, as future work and the continuation of the present research, damage quantification could be studied providing the machine learning methods with other modal properties.

In the present thesis, the mathematical relationship between the numerically calculated structural vibration response and the structural damage status was established using the feed-forward back propagation neural networks and the random forests. In the field of machine learning, more advanced methods are developed every year. As a continuation of the present research, more sophisticated neural networks could be examined for damage quantification (provided more data on intact and damaged beams are available).

The main focus of the present thesis was restricted to the damage localisation and assessment problems. The damage classification problems were set out of the scope. In order to provide a cohesive approach to damage identification (Figure 1.2), collaborative research on damage classification is needed.

At large, the present thesis proposed a theoretical approach for vibration analysis and damage parameter quantification. All the data used in the simulation studies were obtained numerically. The present thesis did not discuss the problems arising from the arrangement of experiments and measured modal data cleansing (filter noise, spike removal, removal of outliers, treatment of missing data). In order to apply the proposed numerical approach not only to the modelling and beam like structure behaviour simulation tasks, but also in practice, the approach has to be validated by the experiment and experimental data.

# References

- [Abou 87] J. ABOUDI. **Stiffness reduction of cracked solids.** *Engineering Fracture Mechanics*, Vol. 26, No. 5, pp. 637–650, 1987. 81
- [Adam 94] P. ADAMS. **Damage detection in composite structures using piezoelectric materials (and neural net).** *Smart Material Structures*, Vol. 3, pp. 318–328, 1994. 136
- [Addi 02] P.S. ADDISON. *The illustrated wavelet transform handbook.* Institute of Physics Publishing, 2002. 34
- [Afol 86] D. AFOLABI. **Natural frequencies of cantilever blades with resilient roots.** *Journal of Sound and Vibration*, Vol. 110, pp. 429–441, 1986. 110
- [Akba 17] K. M. AKBARZADEH, M. SHAAT, A. ABDELKEFI, ET AL. **Nonlocal modeling and buckling features of cracked nanobeams with von Karman nonlinearity.** *Journal of Applied Physics*, Vol. 123, No. 62, 2017. 82
- [Akes 88] B. ÅKESSON AND N. OLHOFF. **Minimum stiffness of optimally located supports for maximum value of beam eigenfrequencies.** *Journal of Sound and Vibration*, Vol. 120, pp. 457–463, 1988. 109
- [Alba 04] C. ALBARRACIN, L. ZANNIER, AND R. GROSSI. **Some observations in the dynamics of beams with intermediate supports.** *Journal of Sound and Vibration*, Vol. 271, pp. 475–480, 2004. 110
- [Atta 12] M. ATTAR. **A transfer matrix method for free vibration analysis and crack identification of stepped beams with multiple edge cracks and different boundary conditions.** *International*

- Journal of Mechanical Sciences*, Vol. 57, No. 1, pp. 19–33, 2012. 82, 83, 84
- [Aydi 14] K. AYDIN AND O. KISI. **Damage detection in Timoshenko beam structures by multilayer perceptron and radial basis function networks.** *Neural Computing and Applications*, Vol. 24, pp. 583–597, 2014. 24, 29, 30, 31
- [Aziz 13] I. AZIZ, S.-U. ISLAM, AND B. SARLER. **Wavelets collocation methods for the numerical solution of elliptic BV problems.** *Applied Mathematical Modelling*, Vol. 37, pp. 676–694, 2013. 33
- [Bala 04] B. BALACHANDRAN AND E.B. MAGRAB. *Vibrations*. Thomson Brooks/Cole, 2004. 45, 46, 48, 49, 50, 51
- [Bane 04] J.R. BANERJEE AND H. SU. **Development of a dynamic stiffness matrix for free vibration analysis of spinning beams.** *Computers and Structures*, Vol. 82, pp. 2189–2197, 2004. 110
- [Bara 13] K. BARAD, D. SHARMA, AND V. VYAS. **Crack detection in cantilever beam by frequency based method.** *Procedia Engineering*, Vol. 51, pp. 770–775, 2013. 84
- [Baro 15] A. BAROUDI AND F. RAZAFIMAHERY. **Transverse vibration analysis of Euler-Bernoulli beam carrying point masse submerged in fluid media.** *International Journal of Engineering and Technology*, Vol. 4, No. 2, pp. 369–380, 2015. 125
- [Bavi 11] P.R. BAVISKAR, S. GURU, AND G. SINGHJI. *Analysis of crack in shaft of blower using finite element analysis and experimental technique*. ApraPress, 2011. 84
- [Beal 16] M.H. BEALE, M.T. HAGAN, AND H.B. DEMUTH. *Neural Network Toolbox™ User's Guide*. The MathWorks, Inc., 16b Ed., 2016. 37, 38, 39, 91, 92, 94
- [Brah 15] K. BRAHMA. **Structural Repair of Aircraft**. 2015. 22
- [Brei 01] L. BREIMAN. **Random forests.** *Machine Learning*, Vol. 45, No. 1, pp. 5–32, 2001. 40, 41



- [Cadd 08] S. CADDEMI AND I. CALIO. **Exact solution of the multi-cracked Euler-Bernoulli column.** *International Journal of Solids and Structures*, Vol. 45, No. 5, pp. 1332–1351, 2008. 83
- [Cadd 09] S. CADDEMI AND I. CALIO. **Exact closed-form solution for the vibration modes of the Euler-Bernoulli beam with multiple open cracks.** *Journal of Sound and Vibration*, Vol. 327, No. 35, pp. 473–489, 2009. 83
- [Cadd 13] S. CADDEMI AND A. MORASSI. **Multi-cracked Euler-Bernoulli beams: Mathematical modeling and exact solutions.** *International Journal of Solids and Structures*, Vol. 50, No. 6, pp. 944–956, 2013. 83
- [Cald 15] L. CALDERONI, M. FERRARA, A. FRANCO, ET AL. **Indoor localization in a hospital environment using Random Forest classifiers.** *Expert Systems with Applications*, Vol. 42, pp. 125–134, 2015. 41
- [Cao 11] M. CAO, L. YE, L. ZHOU, ET AL. **Sensitivity of fundamental mode shape and static deflection for damage identification in cantilever beams.** *Mechanical Systems and Signal Processing*, Vol. 25, pp. 630–643, 2011. 32, 138
- [Card 04] E. CARDEN. **Vibration based condition monitoring: a review.** *Structural Health Monitoring*, Vol. 3, pp. 355–377, 2004. 135
- [Caru 09] D.I. CARUNTU. **Dynamic modal characteristics of transverse vibrations of cantilevers of parabolic thickness.** *Mechanics Research Communications*, Vol. 36, No. 3, pp. 391–404, 2009. 61, 74, 75
- [Caud 88] M. CAUDILL. **Neural network primer, Part III.** *AI Expert*, pp. 53–59, 1988. 36
- [Cele 11] Z. CELEP, K. GULER, AND F. DEMIR. **Response of a completely free beam on a tensionless Pasternak foundation subjected to dynamic load.** *Structural Engineering and Mechanics*, Vol. 37, No. 1, pp. 61–77, 2011. 54

- [Chak 05] D. CHAKRABORTY. **Artificial neural network based delamination prediction in laminated composites.** *Materials and Design*, Vol. 26, pp. 1–7, 2005. 136
- [Chan 94] J. CHANCE, G. TOMLINSON, AND K. WORDEN. **A simplified approach to the numerical and experimental modelling of the dynamics of a cracked beam.** *Proceedings of the 12th International Modal Analysis Conference*, Vol. 2251, p. 778, 1994. 31
- [Chau 00] T.D. CHAUDHARI AND S.K. MAITI. **A study of vibration of geometrically segmented beams with and without crack.** *International Journal of Solids and Structures*, Vol. 37, No. 5, pp. 761–779, 2000. 84
- [Chel 89] K.R. CHELLAPILLA. **Frequency analysis of clamped-clamped uniform beams with intermediate elastic support.** *Journal of Sound and Vibration*, Vol. 133, pp. 502–509, 1989. 110
- [Chen 18] H.-P. CHEN AND Y.-P. NI. *Vibrationbased damage identification methods*, pp. 155–193. John Wiley & Sons Lmd., 2018. 29
- [Chen 63] Y. CHEN. **On the vibration of beams or rods carrying a concentrated mass.** *Journal of Applied Mechanics*, Vol. 30, pp. 310–311, 1963. 124
- [Chen 97] C.K. CHEN AND C.H. HSIAO. **Haar wavelet method for solving lumped and distributed-parameter systems.** *IEE Proceedings - Control Theory and Applications*, Vol. 144, No. 1, pp. 87–94, 1997. 32, 63, 137
- [Chon 98] T.G. CHONDROS, A.D. DIMAROGONAS, AND J. YAO. **A continuous cracked beam vibration theory.** *Journal of Sound and Vibration*, Vol. 215, pp. 17–34, 1998. 82
- [Chri 84] S. CHRISTIDES AND A. BARR. **One-dimensional theory of cracked Bernoulli-Euler beams.** *International Journal of Mechanical Sciences*, Vol. 26, pp. 639–648, 1984. 82
- [Chui 97] C. CHUI. *Wavelets: a mathematical tool for signal analysis*. Society for Industrial and Applied Mathematics, 1997. 137

- [Chun 07] Z. CHUN AND Z. ZHENG. **Three-dimensional analysis of functionally graded plate based on the Haar wavelet method.** *Acta Mechanica Solida Sinica*, Vol. 20, No. 2, pp. 95 – 102, 2007. 63
- [Chun 72] K. CHUN. **Free vibration of a beam with one end spring-hinged and the other free.** *Journal of Applied Mechanics*, Vol. 39, pp. 1154–1155, 1972. 110
- [Cocs 11] S.B. COŞKUN, B. ÖZTÜRK, AND M.T. ATAY. *Transverse vibration analysis of Euler-Bernoulli beams using analytical approximate techniques.* INTECH Open Access Publisher, 2011. 48
- [Comb 02] C. COMBASTEL, S. LESECQ, S. PETROPOL, AND S. GENTIL. **Model-based and wavelet approaches to induction motor on-line fault detection.** *Control Engineering Practice*, Vol. 10, No. 5, pp. 493–509, 2002. 61
- [Conw 65] H. CONWAY AND J. DUBIL. **Vibration frequencies of truncated-cone and wedge beams.** *Journal of Applied Mechanics*, Vol. 32, pp. 932–934, 1965. 61
- [Cour 66] R. COURANT AND D. HILBERT. *Methods of mathematical physics.* Wiley, 1966. 109
- [Das 11] M.M. DAS, B.M. DAS, AND M.D. SAIKIA. *Structural Analysis.* PHI Learning, 2011. 20
- [Dera 08] A. DERAEMAEKER, E. REYNDERS, G. DE ROECK, ET AL. **Vibration-based structural health monitoring using output-only measurements under changing environment.** *Mechanical Systems and Signal Processing*, Vol. 22, No. 1, pp. 34–56, 2008. 137
- [Diet 00] T.G. DIETTERICH. **An experimental comparison of three methods for constructing ensembles of decision trees: bagging, boosting, and randomization.** *Machine Learning*, Vol. 40, No. 2, pp. 139–157, 2000. 40
- [Dima 13] A.D. DIMAROGONAS, S.A. PAIPETIS, AND T.G. CHONDROS. *Analytical methods in rotor dynamics.* Springer, 2013. 53
- [Doeb 98] S. DOEBLING, C. FARRAR, AND M. PRIME. **A summary review of vibration-based damage Identification Methods.** *The Shock and Vibration Digest*, Vol. 30, pp. 91–105, 1998. 29, 30, 31

- [Douk 03] E. DOUKA, S. LOUSTRIDIS, AND A. TROCHIDIS. **Crack identification in beams using wavelet analysis.** *International Journal of Solids and Structures*, Vol. 40, pp. 3557–3569, 2003. 32
- [Elis 01a] I. ELISHAKOFF. **Some unexpected results in vibration of non-homogeneous beams on elastic foundation.** *Chaos, Solitons and Fractals*, Vol. 12, No. 12, pp. 2177–2218, 2001. 54
- [Elis 01b] I. ELISHAKOFF AND S. CANDAN. **Apparently first closed-form solution for vibrating: inhomogeneous beams.** *International Journal of Solids and Structures*, Vol. 38, No. 19, pp. 3411–3441, 2001. 61
- [Elsh 18] M. ELSHAMY, W.A. CROSBY, AND M. ELHADARY. **Crack detection of cantilever beam by natural frequency tracking using experimental and finite element analysis.** *Alexandria Engineering Journal*, Vol. 57, pp. 3755–3766, 2018. 81
- [Erog 16] U. EROGLU AND E. TUFEKCI. **Exact solution based finite element formulation of cracked beams for crack detection.** *International Journal of Solids and Structures*, Vol. 96, pp. 240–253, 2016. 88
- [Erog 17] U. EROGLU AND E. TUFEKCI. **Crack modelling and identification in curved beams using differential evolution.** *International Journal of Mechanical Sciences*, Vol. 131, p. 131, 2017. 81, 82
- [Fan 11] W. FAN AND P. QIAO. **Vibration-based damage identification methods: a review and comparative study.** *Structural Health Monitoring*, Vol. 10, No. 1, pp. 83–111, 2011. 23, 24, 29, 30, 82
- [Farr 01] C.R. FARRAR AND H.Y. SOHN. **Condition/damage monitoring methodologies.** In: *Invited Workshop on Strong-Motion Instrumentation of Buildings, convened by the Consortium of Organizations for Strong-Motion Observation Systems (COSMOS)*, 2001. 30
- [Farr 17] F.A. FARRET, M. SIMOES, AND D. BRANDAO. *Electronic instrumentation for distributed generation and power processes.* CRC Press, 2017. 32
- [Fekl 09] L. FEKLISTOVA. *Back propagation neural network as a predicting tool for vibrating systems.* Master’s thesis, University of Tartu, 2009. 128

- [Fekl 10] L. FEKLISTOVA. **Free vibrations of beams with non-uniform cross-sections and elastic end constraints using Haar wavelet method.** *Proceedings of NSCM-23*, pp. 185–188, 2010. 55
- [Fekl 12] L. FEKLISTOVA AND H. HEIN. **Delamination identification using machine learning methods and Haar wavelets.** *Computer Assisted Methods in Engineering and Science*, Vol. 19, No. 4, pp. 351–360, 2012. 134, 139
- [Fekl 13a] L. FEKLISTOVA AND H. HEIN. **Crack localization in Euler-Bernoulli beams.** *Proceedings of the 2nd International Conference Optimization and Analysis of Structures*, pp. 35–38, 2013. 52
- [Fekl 13b] L. FEKLISTOVA, H. HEIN, AND M. VIKAT. **Parameter identification of vibrating beams with elastic boundary conditions.** In: K.-A. MARDAL, A. LOGG, AND A. MASSING, editors, *Proceedings of the 26th Nordic Seminar on Computational Mechanics*, pp. 54–57, Center for Biomedical Computing Simula Research Laboratory, Oslo, 2013. 109, 113, 114, 118
- [Fekl 14] L. FEKLISTOVA AND H. HEIN. **Parameter identification for supports and cracks in beams with non-classical boundary conditions.** In: S. O. EKOLU ET AL., editors, *International Conference on Construction Materials and Structures*, pp. 1295–1302, IOS Press, Johannesburg, 2014. 109, 114, 118
- [Fekl 15] L. FEKLISTOVA AND H. HEIN. **Stability determination in vibrating non-homogeneous functionally graded Timoshenko beams.** *International Conference on Mechanics and Control Engineering*, pp. 618–623, 2015. 24
- [Fern 99] J. FERNANDEZ-SAEZ, L. RUBIO, AND C. NAVARRO. **Approximate calculation of the fundamental frequency for bending vibrations of cracked beams.** *Journal of Sound and Vibration*, Vol. 225, pp. 345–352, 1999. 82
- [Frit 05] C.P. FRITZEN. **Vibration-Based Structural Health Monitoring Concepts and Applications.** In: *Damage Assessment of Structures VI*, pp. 3–20, Trans Tech Publications Ltd, 2005. 135

- [Gent 03] A. GENTILE AND A. MESSINA. **On the continuous wavelet transforms applied to discrete vibrational data for detecting open cracks in damaged beams.** *International Journal of Solids and Structures*, Vol. 40, pp. 295–315, 2003. 32
- [Glab 99] W. GLABISZ. **Vibration and stability of a beam with elastic supports and concentrated masses under conservative and nonconservative forces.** *Computers and Structures*, Vol. 70, No. 3, pp. 305–313, 1999. 110
- [Gome 19] G.F. GOMES, Y.A.D. MENDEZ, L.A.P. DA SILVA, ET AL. **A review of vibration based inverse methods for damage detection and identification in mechanical structures using optimization algorithms and ANN.** *Archives of Computational Methods in Engineering*, Vol. 26, No. 4, pp. 883–897, 2019. 29
- [Goun 88] G.D GOUNARIS AND A.D. DIMAROGONAS. **A finite element of a cracked prismatic beam for structural analysis.** *Computers and Structures*, Vol. 28, pp. 309–313, 1988. 82
- [Gowd 17] C. GOWDA, N. RAJANNA, AND N.G.S. UDUPA. **Investigating the effects of delamination location and size on the vibration behaviour of laminated composite beams.** *Materials Today: Proceedings*, Vol. 4, pp. 10944–10951, 2017. 135
- [Gros 96] R. GROSSI AND B. ARENAS. **A variational approach to the vibration of tapered beams with elastically restrained ends.** *Journal of Sound and Vibration*, Vol. 195, pp. 507–511, 1996. 62
- [Guem 20] A. GÜEMES, A. FERNANDEZ-LOPEZ, A.R. POZO, AND J. SIERRA-PEREZ. **Structural health monitoring for advanced composite structures: A Review.** *Journal of Composites Science*, Vol. 4, p. 13, 01 2020. 22, 28
- [Hadj 05a] L.J. HADJILEONTIADIS, E. DOUKA, AND A. TROCHIDIS. **Crack detection in beams using kurtosis.** *Computers and Structures*, Vol. 83, No. 1213, pp. 909–919, 2005. 83
- [Hadj 05b] L.J. HADJILEONTIADIS, E. DOUKA, AND A. TROCHIDIS. **Fractal dimension analysis for crack identification in beam structures.** *Mechanical Systems and Signal Processing*, Vol. 19, No. 3, pp. 659–674, 2005. 21

- [Haig 02] S. HAIGH, B. TEYMUR, G. MADABHUSHI, AND D. NEWLAND. **Applications of wavelet analysis to the investigation of the dynamic behavior of geotechnical structures.** *Soil Dynamics and Earthquake Engineering*, Vol. 22, pp. 995–1005, 2002. 62
- [Hais 88] B. S. HAISTY AND W. T. SPRINGER. **A general beam element for use in damage assesement of complex structures.** *Journal of Vibration, Acoustics, Stress and Reliability in Design*, Vol. 110, pp. 389–394, 1988. 82
- [Haki 14] S.J.S. HAKIM, H.A. RAZAK, S. A. RAVANFAR, ET AL. *Structural damage detection using soft computing method*, pp. 143–151. Springer, 2014. 21
- [Haki 15] S.J.S. HAKIM, H.A. RAZAK, AND S.A. RAVANFAR. **Fault diagnosis on beam-like structures from modal parameters using artificial neural networks.** *Measurement: Journal of the International Measurement Confederation*, Vol. 76, pp. 45–61, 2015. 28, 84, 86, 94
- [Hamd 94] M.N. HAMDAN AND L.A. LATIF. **On the numerical convergence of discretization methods for the free vibrations of beams with attached inertia elements.** *Journal of Sound and Vibration*, Vol. 169, pp. 527–545, 1994. 124
- [Han 05a] J.-G. HAN, W.-X. REN, AND Z.-S. SUN. **Wavelet packet based damage identification of beam structures.** *International Journal of Solids and Structures*, Vol. 42, No. 26, pp. 6610–6627, 2005. 32, 137
- [Han 05b] Y. HAN, A. MISRA, AND D. MATEESCU. **A method for crack detection in structures using piezoelectric sensors and actuators.** In: *Proceedings of 2005 International Conference on MEMS, NANO and Smart Systems*, pp. 353–354, 2005. 84
- [Han 07] J.-G. HAN, W.-X. REN, AND Y. HUANG. **A wavelet-based stochastic finite element method of thin plate bending.** *Applied Mathematical Modelling*, Vol. 31, pp. 181–193, 2007. 62
- [Hayk 99] S. HAYKIN. *Neural Networks: A Comprehensive Foundation*. Prentice Hall., 1 Ed., 1999. 38, 39

- [He 01] Y. HE, D. GUO, AND F. CHU. **Using genetic algorithms and finite element methods to detect shaft crack for rotor-bearing system.** *Mathematics and Computers in Simulation*, Vol. 57, No. 12, pp. 95–108, 2001. 86
- [Hein 07] H. HEIN. **Determination of foundation characteristics of vibrating beams using wavelet transform and neural network.** *Proceedings of Society for Optical Engineering*, Vol. 6763, pp. 1–9, 2007. 32, 63, 125
- [Hein 09] H. HEIN AND L. FEKLISTOVA. **Identification of mass location on vibrating beams using Haar wavelets and neural networks.** *Proceedings of 22nd Nordic Seminar of Computational Mechanics*, pp. 105–108, 2009. 51, 123
- [Hein 11a] H. HEIN AND L. TOVA. **Free vibrations of non-uniform and axially functionally graded beams using Haar wavelets.** *Engineering Structures*, Vol. 33, No. 12, pp. 3696–3701, 2011. 59, 63
- [Hein 11b] H. HEIN AND L. FEKLISTOVA. **Computationally efficient delamination detection in composite beams using Haar wavelets.** *Mechanical Systems and Signal Processing*, Vol. 25, No. 6, pp. 2257–2270, 2011. 56, 134, 138, 139, 146
- [Hein 11c] H. HEIN AND L. FEKLISTOVA. **System Modeling for Delamination Detection using Support Vector Machines and Neural Networks.** In: *Proceedings of the 24th Nordic Seminar on Computational Mechanics*, pp. 73–76, 2011. 24
- [Hein 12a] H. HEIN AND L. FEKLISTOVA. **Free vibration and buckling of functionally graded Euler-Bernoulli and Timoshenko beams using Haar wavelets.** In: *Days on Diffraction 2012: Abstracts*, p. 55, 2012. 22, 24, 149
- [Hein 12b] H. HEIN AND L. FEKLISTOVA. **Free vibration and stability analysis of functionally graded Timoshenko beams.** In: *Abstracts of 10th World Congress on Computational Mechanics*, p. 287, 2012. 24, 149
- [Hein 19a] H. HEIN AND L. JAANUSKA. **Comparison of machine learning methods for crack localization.** *Acta et Commentationes Univer-*



- sitatis Tartuensis de Mathematica*, Vol. 23, pp. 125–142, 2019. 81, 82
- [Hein 19b] H. HEIN AND L. JAANUSKA. **Modal-based parameter identification in vibrating nano-beams using machine learning.** In: *AIP Conference Proceedings*, p. 330005, 07 2019. 24, 149
- [Ho 95] T.K. HO. **Random decision forests.** In: *Proceedings of the Third International Conference on Document Analysis and Recognition, Vol. 1*, pp. 278–282, IEEE Computer Society, Washington, DC, USA, 1995. 40
- [Ho 98] S.H. HO AND C.K. CHEN. **Analysis of general elastically end restrained non-uniform beams using differential transform.** *Applied Mathematical Modelling*, Vol. 22, No. 45, pp. 219–234, 1998. 62
- [Hong 02] J.-C. HONG, Y.Y. KIM, H.C. LEE, ET AL. **Damage detection using the Lipschitz exponent estimated by the wavelet transform: applications to vibration modes of a beam.** *International Journal of Solids and Structures*, Vol. 39, No. 7, pp. 1803–1816, 2002. 32
- [Hoss 12] M. HOSSEINI AND H. ABBAS. **Neural network approach for prediction of deflection of clamped beams struck by a mass.** *Thin-Walled Structures*, Vol. 60, pp. 222–228, 2012. 125
- [Hoss 17] M.S. HOSSAIN, Z.C. ONG, Z. ISMAIL, ET AL. **Artificial neural networks for vibration based inverse parametric identifications: A review.** *Applied Soft Computing*, Vol. 52, pp. 203–219, 2017. 29, 37
- [Hsia 99] C.-H. HSIAO AND W.-J. WANG. **State analysis of time-varying singular nonlinear systems via Haar wavelets.** *Mathematics and Computers in Simulation*, Vol. 51, No. 12, pp. 91–100, 1999. 32, 35, 63, 137
- [Hsu 08] J.-C. HSU, H.-Y. LAI, AND C.K. CHEN. **Free vibration of non-uniform Euler-Bernoulli beams with general elastically end constraints using Adomian modified decomposition method.** *Journal of Sound and Vibration*, Vol. 318, No. 45, pp. 965–981, 2008. 56, 62, 71, 72, 73, 110

- [Hu 06] C. HU AND M.T. AFZAL. **A statistical algorithm for comparing mode shapes of vibration testing before and after damage in timbers.** *Journal of Wood Science*, Vol. 52, No. 4, pp. 348–352, 2006. 30, 83
- [Huan 10] Y. HUANG AND X.-F. LI. **A new approach for free vibration of axially functionally graded beams with non-uniform cross-section.** *Journal of Sound and Vibration*, Vol. 329, No. 11, pp. 2291–2303, 2010. 61, 76, 77
- [Jaan 16] L. JAANUSKA AND H. HEIN. **Crack identification in beams using Haar wavelets and machine learning methods.** *International Journal of Mechanics*, Vol. 10, pp. 281–287, 2016. 39, 53, 81
- [Jafa 13] R.A. JAFARI-TALOOKOLAEI, M. KARGARNOVIN, AND M. AHMADIAN. **Dynamic response of a delaminated composite beam with general lay-ups based on the first-order shear deformation theory.** *Composites Part B Engineering*, Vol. 55, pp. 65–78, 2013. 134, 135
- [Jane 17] R. JANELIUKSTIS, S. RUCEVSKIS, M. WESOLOWSKI, ET AL. **Multiple damage identification in beam structure based on wavelet transform.** *Procedia Engineering*, Vol. 172, pp. 426–432, 2017. 62
- [Jaya 15] M. JAYAWARDHANA, X. ZHU, R. LIYANAPATHIRANA, ET AL. **Statistical damage sensitive feature for structural damage detection using AR model Coefficients.** *Advances in Structural Engineering*, Vol. 18, No. 10, p. 15511562, 2015. 21
- [Kahy 17] V. KAHYA AND M. TURAN. **Finite element model for vibration and buckling of functionally graded beams based on the first-order shear deformation theory.** *Composites Part B: Engineering*, Vol. 109, pp. 108–115, 2017. 62
- [Kalp 07] R. KALPANA AND S. RAJA BALACHANDAR. **Haar wavelet method for the analysis of transistor circuits.** *AEU - International Journal of Electronics and Communications*, Vol. 61, No. 9, pp. 589 – 594, 2007. 64
- [Kapu 08] S. KAPURIA, M. BHATTACHARYYA, AND A.N. KUMAR. **Bending and free vibration response of layered functionally graded**

- beams: A theoretical model and its experimental validation.** *Composite Structures*, Vol. 82, No. 3, pp. 390–402, 2008. 62
- [Karb 09] V.M. KARBHARI. *Structural health monitoring of civil infrastructure systems*. Woodhead Publishing, United Kingdom, 2009. 30
- [Karb 14] A. KARBASSI, B. MOHEBI, S. REZAEI, ET AL. **Damage prediction for regular reinforced concrete buildings using the decision tree algorithm.** *Computers and Structures*, Vol. 130, pp. 46–56, 2014. 42
- [Karn 01] I.A. KARNOVSKII AND I.O. LEBED. *Formulas for structural dynamics*. McGraw-Hill, 2001. 47, 52, 70
- [Kim 01] H.K. KIM AND M.S. KIM. **Vibration of beams with generally restrained boundary conditions using Fourier series.** *Journal of Sound and Vibration*, Vol. 245, pp. 771–784, 2001. 111
- [Kim 03] J.-T. KIM, Y.-S. RYU, H.-M. CHO, ET AL. **Damage identification in beam-type structures: frequency-based method vs mode-shape-based method.** *Engineering Structures*, Vol. 25, No. 1, pp. 57–67, 2003. 30, 136, 137
- [Kirs 18] M. KIRS. *Evaluation of Haar wavelet method for analysis of functionally graded and nanostructures*. PhD thesis, Tallinn University of Technology, 2018. 148
- [Klei 75] L. KLEIN. **Transverse vibrations of non-uniform beams.** *Journal of Sound and Vibration*, Vol. 37, pp. 491–505, 1975. 62
- [Kona 11] P. KONAR AND P. CHATTOPADHYAY. **Bearing fault detection of induction motor using wavelet and Support Vector Machines (SVMs).** *Applied Soft Computing*, Vol. 11, No. 6, pp. 4203–4211, 2011. 21
- [Kono 18] O. KONONENKO AND I. KONONENKO. **Machine learning and finite element method for physical systems modeling.** *ArXiv*, pp. 1–5, 2018. 62, 136
- [Kova 10] V.K. KOVALEV. **Lecture notes.** 2010. [<https://www.turbiniist.ru/1004-metodicheskoe-posobie-po-opredeleniyu-chastot-sobstvennyx-kolebanij-uzlov-i-detalej.html>].

- [Kraw 02] M. KRAWCZUK AND W. OSTACHOWICZ. **Identification of delamination in composite beams by genetic algorithm.** *Science and Engineering of Composite Materials*, Vol. 10, pp. 147–155, 2002. 136
- [Kuma 13] S.K. KUMAR, R. GANGULI, AND D. HARURSAMPATH. **Partial delamination modeling in composite beams using a finite element method.** *Finite Elements in Analysis and Design*, Vol. 76, pp. 1–12, 2013. 135
- [Lahi 09] S.K. LAHIRI AND K.C. GHANTA. **Artificial neural network model with the parameter tuning assisted by a differential evolution technique: The study of the hold up of the slurry flow in a pipeline.** *Chemical Industry and Chemical Engineering Quarterly*, Vol. 15, No. 2, pp. 103–117, 2009. 39
- [Lard 02] J. LARDIES AND S. GOUTTEBROZE. **Identification of modal parameters using the Wavelet transform.** *International Journal of Mechanical Sciences*, Vol. 44, pp. 2263–2283, 2002. 62
- [Lau 84] J. LAU. **Vibration frequencies and mode shapes for a constrained cantilever.** *Journal of Applied Mechanics*, Vol. 51, pp. 182–187, 1984. 110
- [Laur 83] P.A.A. LAURA, P. VERNIEREDEIRASSAR, AND G.M. FICCADENTI. **A note on transverse vibrations of continuous beams subject to an axial force and carrying concentrated masses.** *Journal of Sound and Vibration*, Vol. 86, pp. 279–284, 1983. 124
- [Le 17] T.-P. LE. **Use of the Morlet mother wavelet in the frequency-scale domain decomposition technique for the modal identification of ambient vibration responses.** *Mechanical Systems and Signal Processing*, Vol. 95, pp. 488–505, 2017. 62
- [Lee 09] J. LEE. **Identification of multiple cracks using natural frequencies.** *Journal of Sound and Vibration*, Vol. 320, pp. 482–490, 2009. 84
- [Lepi 05] Ü. LEPIK. **Numerical solution of differential equations using Haar wavelets.** *Mathematics and Computers in Simulation*, Vol. 68, No. 2, pp. 127–143, 2005. 33, 63, 73, 137

- [Lepi 14] Ü. LEPIK AND H. HEIN. *Haar wavelets*. Springer, 2014. 32, 33, 34, 35, 62, 63
- [Li 00] W.L. LI. **Free vibrations of beams with general boundary conditions**. *Journal of Sound and Vibration*, Vol. 237, No. 4, pp. 709–725, 2000. 110
- [Lian 92] R.Y. LIANG, J. HU, AND F. CHOY. **Theoretical study of crack-induced eigenfrequency changes on beam structures**. *Journal of Engineering Mechanics*, Vol. 118, No. 2, pp. 384–396, 1992. 82, 84
- [Liaw 02] A. LIAW AND M. WIENER. **Classification and regression by random forest**. *R News*, Vol. 2, No. 3, pp. 18–22, 2002. 41
- [Liew 98] K. LIEW AND Q. WANG. **Application of wavelet theory for crack identification in structures**. *Journal of Engineering Mechanics-ASCE*, Vol. 124, pp. 152–157, 1998. 32
- [Liu 05] W. LIU, W.C. GAO, AND Y. SUN. **Research on damage detection of reticulated shell**. In: J. OU, H. LI, AND Z. DUAN, editors, *Structural Health Monitoring and Intelligent Infrastructure, Two Volume Set: Proceedings of the 2nd International Conference on Structural Health Monitoring of Intelligent Infrastructure*, pp. 807–812, 2005. 30
- [Liu 13] Y. LIU, M.-Y. WANG, AND C.-M. SONG. **Analysis of elastic support beam on dynamic load**. In: *Geotechnical Special Publication*, pp. 422–429, 2013. 110
- [Liu 88] W. LIU, J.-R. WU, AND C.-C. HUANG. **Free vibration of beams with elastically restrained edges and intermediate concentrated masses**. *Journal of Sound and Vibration*, Vol. 122, pp. 193–207, 1988. 124
- [Lore 18] S. LORENZO, C. ADAM, A. BURLON, ET AL. **Flexural vibrations of discontinuous layered elastically bonded beams**. *Composites Part B Engineering*, Vol. 135, pp. 175–188, 2018. 110
- [Low 00] K. LOW. **Modified Dunkerley formula for eigenfrequencies of beams carrying concentrated masses**. *International Journal of Mechanical Sciences*, Vol. 42, pp. 1287–1305, 2000. 124

- [Low 01] K. LOW. **Improved model for the frequency estimate of mass-loaded plates by a combined use of equivalent center mass and stiffness factors.** *International Journal of Mechanical Sciences*, Vol. 43, pp. 581–594, 2001. 124
- [Low 03] K.H. LOW. **Natural frequencies of a beam–mass system in transverse vibration: Rayleigh estimation versus eigenanalysis solutions.** *International Journal of Mechanical Sciences*, Vol. 45, No. 6, pp. 981–993, 2003. 124
- [Low 93] K.H. LOW, T. LIM, AND G. CHAI. **Experimental and analytical investigations of vibration frequencies for centre-loaded beams.** *Computers and Structures*, Vol. 48, pp. 1157–1162, 1993. 124
- [Low 94] K.H. LOW. **An equivalent-center method for quick frequency analysis of beams carrying a concentrated mass.** *Computers and Structures*, Vol. 50, pp. 409–419, 1994. 124, 126
- [Low 97a] K. LOW, G. CHAI, AND G. TAN. **A comparative study of vibrating loaded plates between the Rayleigh-Ritz and experimental methods.** *Journal of Sound and Vibration*, Vol. 199, pp. 285–297, 1997. 124
- [Low 97b] K. LOW, R. DUBEY, AND G. CHAI. **Experimental investigations and shape functions for lateral vibration of axially constrained beams with a concentrated mass at the centre.** *Journal of Sound and Vibration*, Vol. 202, pp. 446–451, 1997. 124
- [Low 97c] K.H. LOW. **An analytical-experimental comparative study of vibration analysis for loaded beams with variable boundary conditions.** *Computers and Structures*, Vol. 65, No. 1, pp. 97–107, 1997. 124
- [Low 98] K. LOW, G. CHAI, T. LIM, ET AL. **Comparisons of experimental and theoretical frequencies for rectangular plates with various boundary conditions and added masses.** *International Journal of Mechanical Sciences*, Vol. 40, pp. 1119–1131, 1998. 124
- [Loya 09] J. LOYA, J. PUENTE, R. ZAERA, ET AL. **Free transverse vibrations of cracked nanobeams using a nonlocal elasticity model.** *Journal of Applied Physics*, Vol. 105, pp. 1–9, 2009. 82

- [Luo 00] H. LUO AND S. HANAGUD. **Dynamics of delaminated beams.** *International Journal of Solids and Structures*, Vol. 37, pp. 1501–1519, 2000. 135
- [Mahd 13] S. MAHDAVI AND A.H. RAZAK. **A wavelet-based approach for vibration analysis of framed structures.** *Applied Mathematics and Computation*, pp. 414–428, 2013. 62
- [Mahm 99] M.A. MAHMOUD AND M.A.A. KIEFA. **Neural network solution of the inverse vibration problem.** *NDT&E International*, Vol. 32, No. 2, pp. 91–99, 1999. 84, 85, 88, 89, 108
- [Maja 15] J. MAJAK, B. SHVARTSMAN, M. KIRS, ET AL. **Convergence theorem for the Haar wavelet based discretization method.** *Composite Structures*, Vol. 126, pp. 227–232, 2015. 35
- [Maja 18] J. MAJAK, M. POHLAK, K. KARJUST, ET AL. **New higher order Haar wavelet method: application to fgm structures.** *Composite Structures*, Vol. 201, pp. 72–78, 2018. 35, 89, 148
- [Marw 00] T. MARWALA. *Fault identification using neural networks and vibration data.* PhD thesis, St. John’s College, 2000. 23
- [Marw 99] T. MARWALA AND H.E.M. HUNT. **Fault identification using finite element models and neural networks.** *Mechanical Systems and Signal Processing*, Vol. 13, No. 3, pp. 475–490, 1999. 94
- [Mesh 15] N.A. MESHARAM AND V.S. PAWAR. **Analysis of crack detection of a cantilever beam using finite element analysis.** *International Journal of Engineering Research and*, Vol. 4, No. 4, 2015. 84
- [Mess 98] A. MESSINA, E. WILLIAMS, AND T. CONTURSI. **Structural damage detection by a sensitivity and statistical-based method.** *Journal of Sound and Vibration*, Vol. 216, pp. 791–808, 1998. 84
- [Misi 13] M. MISITI, Y. MISITI, G. OPPENHEIM, ET AL. *Wavelets and their applications.* Wiley, 2013. 22
- [Misi 96] M. MISITI, Y. MISITI, G. OPPENHEIM, ET AL. *Wavelet Toolbox Users Guide.* The MathWorks, Inc., 1996. 22

- [Muju 88] P. MUJUMDAR AND S. SURYANARAYAN. **Flexural vibration of beams with delaminations.** *Journal of Sound and Vibration*, Vol. 125, pp. 441–461, 1988. 135
- [Nag 02] A. NAG, D. MAHAPATRA, AND S. GOPALAKRISHNAN. **Identification of delamination in composite beams using spectral estimation and a genetic algorithm.** *Smart Materials and Structures*, Vol. 11, p. 899, 2002. 136
- [Naga 10] T. NAGASHIMA AND H. SUEMASU. **X-FEM analyses of a thin-walled composite shell structure with a delamination.** *Computers and Structures*, Vol. 88, pp. 549–557, 2010. 135
- [Nagu 02] S. NAGULESWARAN. **Transverse vibrations of an Euler–Bernoulli uniform beam carrying several particles.** *International Journal of Mechanical Sciences*, Vol. 44, pp. 2463–2478, 2002. 110, 125
- [Nagu 94] S. NAGULESWARAN. **A direct solution for the transverse vibration of Euler-Bernoulli wedge and cone beams.** *Journal of Sound and Vibration*, Vol. 172, No. 3, pp. 289–304, 1994. 61, 71
- [Nand 97a] B. NANDWANA AND S. MAITI. **Detection of the location and size of a crack in stepped cantilever beams based on measurements of natural frequencies.** *Journal of Sound and Vibration*, Vol. 203, pp. 435–446, 1997. 84
- [Nand 97b] B.P. NANDWANA AND S.K. MAITI. **Modelling of vibration of beam in presence of inclined edge or internal crack for its possible detection based on frequency measurements.** *Engineering Fracture Mechanics*, Vol. 58, No. 3, pp. 193–205, 1997. 84
- [Ndam 02] J.-M. NDAMBI, J. VANTOMME, AND K. HARRI. **Damage assessment in reinforced concrete beams using eigenfrequencies and mode shape derivatives.** *Engineering Structures*, Vol. 24, No. 4, pp. 501–515, 2002. 21, 87, 108, 149
- [Neil 03] S. NEILD, P.D. MCFADDEN, AND M.S. WILLIAMS. **A review of time-frequency methods for structural vibration analysis.** *Engineering Structures*, Vol. 25, pp. 713–728, 2003. 62



- [Niel 15] M.A. NIELSEN. *Neural networks and deep learning*. Determination Press, 2015. 38, 39
- [Niga 20] R. NIGAM AND S. SINGH. **Crack detection in a beam using wavelet transform and photographic measurements**. *Structures*, Vol. 25, pp. 436–447, 2020. 20, 81
- [Niko 18] M. NIKOO, M. HADZIMA-NYARKO, AND K. NYARKO. **Determining the natural frequency of cantilever beams using ann and heuristic search**. *Applied Artificial Intelligence*, pp. 1–26, 2018. 125
- [Okaf 99] A. OKAFOR, K. CHANDRASHEKHARA, AND Y.P. JIANG. **Delamination prediction in composite beams with built-in piezoelectric devices using modal analysis and neural network**. *Smart Materials and Structures*, Vol. 5, p. 338, 1999. 136
- [Ooij 14] T. OOIJEVAAR. *Vibration based structural health monitoring of composite skin-stiffener structures*. PhD thesis, University of Twente, 2014. 21, 28, 29
- [Orha 07] S. ORHAN. **Analysis of free and forced vibration of a cracked cantilever beam**. *NDT&E International*, Vol. 40, pp. 443–450, 2007. 20
- [Osta 13] W. M. OSTACHOWICZ AND A. GÜEMES. *New trends in structural health monitoring*. Springer, 2013. 21
- [Owol 03] G. OWOLABI AND R. SESHADRI. **Crack detection in beams using changes in frequencies and amplitudes of frequency response functions**. *Journal of Sound and Vibration*, Vol. 265, pp. 1–22, 2003. 83
- [Ozka 99] E. ÖZKAYA AND M. PAKDEMIRLI. **Non-linear vibrations of a beam-mass system with both ends clamped**. *Journal of Sound and Vibration*, Vol. 221, pp. 491–503, 1999. 124
- [Pand 91] A.K. PANDEY, M. BISWAS, AND M.M. SAMMAN. **Damage detection from changes in curvature mode shapes**. *Journal of Sound and Vibration*, Vol. 145, pp. 321–332, 1991. 31
- [Papa 89] N. PAPAECONOMOU AND A. DIMAROGONAS. **Vibration of cracked beams**. *Computational Mechanics*, Vol. 5, No. 2, pp. 88–94, 1989. 82

- [Pati 17] R.A. PATIL AND M.V. KAVADE. **Delamination detection in composite sandwich beam: experimental study.** *Journal of Advances in Science and Technology*, Vol. 13, No. 1, pp. 199–204, 2017. 134, 135
- [Petr 81] H. PETROSKI. **Simple static and dynamic models for the cracked elastic beam.** *International Journal of Fracture*, Vol. 17, pp. 71–76, 1981. 82
- [Pras 11] B.B. PRASAD. *Advanced soil dynamics and earthquake engineering.* PHI Learning Private Ltd, 2011. 47
- [Quek 01] S.-T. QUEK, Q. WANG, L. ZHANG, ET AL. **Sensitivity analysis of crack detection in beams by wavelet technique.** *International Journal of Mechanical Sciences*, Vol. 43, No. 12, pp. 2899–2910, 2001. 31, 32
- [Ramk 79] R.L. RAMKUMAR, S.V. KULKARNI, AND B. PIPES. **Free vibration frequencies of a delaminated beam.** *34th Annual Technical Conference Proceedings*, pp. 1–5, 1979. 135
- [Rao 05] S.S. RAO. *Mechanical vibrations.* Prentice Hall, 2005. 44
- [Raza 06] H.A. RAZAK AND Z. ISMAIL. **Flexural stiffness determination using mode shape derivative.** *Asian Journal of Civil Engineering (Building and Housing)*, Vol. 3, 01 2006. 31
- [Redd 97] J.N. REDDY. *Mechanics of laminated composite plates.* CRC Press, 1997. 57
- [Reza 11] M. REZAEI AND R. HASSANNEJAD. **A new approach to free vibration analysis of a beam with a breathing crack based on mechanical energy balance method.** *Acta Mechanica Solida Sinica*, Vol. 24, No. 2, pp. 185–194, 2011. 83
- [Rio 14] S. DEL RÍO, V. LÓPEZ, J. BENÍTEZ, ET AL. **On the use of mapreduce for imbalanced big data using random forest.** *Inf. Sci.*, Vol. 285, No. C, pp. 112–137, 2014. 40
- [Rizo 90] P.F. RIZOS, N. ASPRAGATHOS, AND A.D. DIMAROGONAS. **Identification of crack location and magnitude in a cantilever**

- beam from the vibration modes. *Journal of Sound and Vibration*, Vol. 138, No. 3, pp. 381–388, 1990. 52, 54, 83
- [Ronu 19] S.G. RONČEVIĆ, B. RONČEVIĆ, A. SKOBLAR, ET AL. **Closed form solutions for frequency equation and mode shapes of elastically supported Euler-Bernoulli beams.** *Journal of Sound and Vibration*, Vol. 457, pp. 118–138, 2019. 110
- [Rosa 03] M. ROSA, N. AUCIELLO, AND M. MAURIZI. **The use of Mathematica in the dynamic analysis of a beam with a concentrated mass and dashpot.** *Journal of Sound and Vibration*, Vol. 263, pp. 219–226, 2003. 125
- [Rosa 09] M.B. ROSALES, C.P. FILIPICH, AND F.S. BUEZAS. **Crack detection in beam-like structures.** *Engineering Structures*, Vol. 31, No. 10, pp. 2257–2264, 2009. 21, 88
- [Rosa 96] M. ROSA, C. FRANCIOSI, AND M. MAURIZI. **On the dynamic behaviour of slender beams with elastic ends carrying a concentrated mass.** *Computers and Structures*, Vol. 58, pp. 1145–1159, 1996. 51, 124
- [Rosa 99] M.A. ROSA AND M.J. MAURIZI. **Dynamic analysis of multistep piles on Pasternak soil subjected to axial tip forces.** *Journal of Sound and Vibration*, Vol. 219, No. 5, pp. 771–783, 1999. 55
- [Rous 01] C.-E. ROUSSEAU AND H.V. TIPPUR. **Influence of elastic gradient profiles on dynamically loaded functionally graded materials: cracks along the gradient.** *International Journal of Solids and Structures*, Vol. 38, No. 4445, pp. 7839–7856, 2001. 62
- [Ruck 06a] M. RUCKA AND K. WILDE. **Application of continuous wavelet transform in vibration based damage detection method for beams and plates.** *Journal of Sound and Vibration*, Vol. 297, No. 35, pp. 536–550, 2006. 31, 32, 137
- [Ruck 06b] M. RUCKA AND K. WILDE. **Crack identification using wavelets on experimental static deflection profiles.** *Engineering Structures*, Vol. 28, No. 2, pp. 279–288, 2006. 28, 31
- [Sain 10] M. SAINLEZ AND G. HEYEN. **Performance monitoring of an industrial boiler: classification of relevant variables with**

- Random Forests.** In: S. PIERUCCI AND G.B. FERRARIS, editors, *20th European Symposium on Computer Aided Process Engineering*, pp. 403–408, Elsevier, 2010. 42
- [Sait 79] H. SAITO AND K. MORI. **Vibrations of a beam with non-linear elastic constraints.** *Journal of Sound and Vibration*, Vol. 66, pp. 1–8, 1979. 110
- [Sala 97] O. SALAWU. **Detection of structural damage through changes in frequency: a review.** *Engineering Structures*, Vol. 19, pp. 718–723, 1997. 84
- [Samu 05] P.D. SAMUEL AND D.J. PINES. **A review of vibration-based techniques for helicopter transmission diagnostics.** *Journal of Sound and Vibration*, Vol. 282, No. 12, pp. 475–508, 2005. 29
- [SAS ] SAS INSTITUTE. **Machine Learning: What it is and why it matters.** 35
- [Sato 08] M. SATO, S. KANIE, AND T. MIKAMI. **Mathematical analogy of a beam on elastic supports as a beam on elastic foundation.** *Applied Mathematical Modelling*, Vol. 32, pp. 688–699, 2008. 110
- [Shar 13] A. SHARMA AND A. CHOPRA. **Artificial neural networks: applications in management.** *IOSR Journal of Business and Management*, Vol. 12, No. 5, pp. 32–40, 2013. 37
- [Shen 90] M.-H.H. SHEN AND C. PIERRE. **Natural modes of Bernoulli-Euler beams with symmetric cracks.** *Journal of Sound and Vibration*, Vol. 138, No. 1, pp. 115–134, 1990. 82, 138
- [Shif 99] E.I. SHIFRIN AND R. RUOTOLO. **Natural frequencies of a beam with arbitrary number of cracks.** *Journal of Sound and Vibration*, Vol. 222, No. 3, pp. 409–423, 1999. 54
- [Shu 04a] D. SHU AND C.N. DELLA. **Free vibration analysis of composite beams with two non-overlapping delaminations.** *International Journal of Mechanical Sciences*, Vol. 46, No. 4, pp. 509–526, 2004. 56, 59, 138
- [Shu 04b] D. SHU AND C.N. DELLA. **Vibrations of multiple delaminated beams.** *Composite Structures*, Vol. 64, No. 34, pp. 467–477, 2004. 56, 58

- [Shva 16] B. SHVARTSMAN AND J. MAJAK. **Numerical method for stability analysis of functionally graded beams on elastic foundation.** *Applied Mathematical Modelling*, Vol. 40, No. 5, pp. 3713–3719, 2016. 63
- [Silv 09] T. SILVA, N. MAIA, A. ROQUE, ET AL. **Identification of elastic support properties on a Bernoulli-Euler beam.** In: *Conference Proceedings of the Society for Experimental Mechanics Series*, pp. 6–13, 2009. 110
- [Sing 03] K.N. SINGH, A. KUMAR, AND H. CHANDRA. *Forecasting techniques in agriculture.* ICAR, 2003. 37, 38
- [Srin 10] D. SRINIVASARAO, K. MALLIKARJUNA, AND G.V. RAJU. **Crack identification on a beam by vibration measurement and wavelet analysis.** *International Journal of Engineering Science and Technology*, Vol. 2, pp. 907–912, 2010. 32
- [Su 05] H. SU AND J.R. BANERJEE. **Exact natural frequencies of structures consisting of two-part beam-mass systems.** *Structural Engineering and Mechanics*, Vol. 19, pp. 551–566, 2005. 125
- [Sun 07] W. SUN, J. CHEN, AND J. LI. **Decision tree and PCA-based fault diagnosis of rotating machinery.** *Mechanical Systems and Signal Processing*, Vol. 21, pp. 1300–1317, 2007. 42
- [Suta 15] M.K. SUTAR, S. PATTNAIK, AND J. RANA. **Neural based controller for smart detection of crack in cracked cantilever beam.** *Materials Today: Proceedings*, Vol. 2, No. 45, pp. 2648–2653, 2015. 86
- [Tan 17] Z. TAN, D. THAMBIRATNAM, T. CHAN, ET AL. **Detecting damage in steel beams using modal strain energy based damage index and Artificial Neural Network.** *Engineering Failure Analysis*, Vol. 79, 2017. 31
- [Timo 83] S. TIMOSHENKO. *History of Strength of Materials.* Dover Publications, 1983. 20
- [Took 14] T. TOOKE, N. COOPS, AND J. WEBSTER. **Predicting building ages from LiDAR data with random forests for building en-**

- ergy modeling.** *Energy and Buildings*, Vol. 68, pp. 603–610, 2014. 42
- [Tuck 11] A. TUCK AND V. KEKOC. **KC–30A structural health monitoring system verification and validation; MRH 90 HUMS.** *AIAC14 Fourteenth Australian International Aerospace Congress*, pp. 3–18, 2011. 135
- [Tuse 15] H. TÜSELMANN, R. SINKOVICS, AND G. PISHCHULOV. **Towards a consolidation of worldwide journal rankings - A classification using random forests and aggregate rating via data envelopment analysis.** *Omega*, Vol. 51, pp. 11–23, 2015. 41
- [Twom 95] J.M. TWOMEY AND A.E. SMITH. **Performance measures, consistency, and power for artificial neural network models.** *Mathematical and Computer Modelling*, Vol. 21, No. 1, pp. 243–258, 1995. 91
- [Uber 16] F. UBERTINI, G. COMANDUCCI, AND N. CAVALAGLI. **Vibration-based structural health monitoring of a historic bell-tower using output-only measurements and multivariate statistical analysis.** *Structural Health Monitoring: An International Journal*, Vol. 15, No. 4, p. 438457, 2016. 21
- [Umes 09] P. UMESHA, R. RAVICHANDRAN, AND K. SIVASUBRAMANIAN. **Crack detection and quantification in beams using wavelets.** *Computer-Aided Civil and Infrastructure Engineering*, Vol. 24, pp. 593–607, 2009. 32
- [Vika 12] M. VIKAT. *Identification of non-classical boundary conditions with the aid of artificial neural networks.* Master’s thesis, University of Tartu, 2012. 113
- [Waha 99] M.M.A. WAHAB AND G. DE ROECK. **Damage detection in bridges using modal curvatures: Application to a real damage scenario.** *Journal of Sound and Vibration*, Vol. 226, pp. 217–235, 1999. 31
- [Wang 06] D. WANG, M. FRISWELL, AND Y. LEI. **Maximizing the natural frequency of a beam with an intermediate elastic support.** *Journal of Sound and Vibration*, Vol. 291, pp. 1229–1238, 2006. 110

- [Wang 13] L. WANG, J. MA, J. PENG, ET AL. **Large amplitude vibration and parametric instability of inextensional beams on the elastic foundation.** *International Journal of Mechanical Sciences*, Vol. 67, pp. 1–9, 2013. 110
- [Wang 18] Y. WANG. *Damage assessment in asymmetric buildings using vibration techniques.* PhD thesis, Queensland University of Technology, 2018. 21, 24, 26, 30, 31
- [Wang 67] H.-C. WANG. **Generalized Hypergeometric Function Solutions on the Transverse Vibration of a Class of Nonuniform Beams.** *Journal of Applied Mechanics*, Vol. 34, No. 3, p. 702, 1967. 61
- [Wang 82] J.T.S. WANG, Y. LIU, AND J.A. GIBBY. **Vibration of split beams.** *Journal of Sound and Vibration*, Vol. 84, pp. 491–502, 1982. 135
- [Wang 99a] Q. WANG AND X. DENG. **Damage detection with spatial wavelets.** *International Journal of Solids and Structures*, Vol. 36, pp. 3443–3468, 1999. 32
- [Wang 99b] Q. WANG AND X. DENG. **Damage detection with spatial wavelets.** *International Journal of Solids and Structures*, Vol. 36, pp. 3443–3468, 1999. 63
- [Watk 02] S.E. WATKINS, G. W. SANDERS, F. AKHAVAN, ET AL. **Modal analysis using fiber optic sensors and neural networks for prediction of composite beam delamination.** *Smart Materials and Structures*, Vol. 11, No. 4, pp. 489–495, 2002. 136
- [Wei 04] Z. WEI, L.H. YAM, AND L. CHENG. **Detection of internal delamination in multi-layer composites using wavelet packets combined with modal parameter analysis.** *Composite Structures*, Vol. 64, No. 34, pp. 377–387, 2004. 30
- [Will 87] G.J. WILLIAMS. **Combining decision trees: initial results from the MIL algorithm.** In: J.S. GERO AND R.B. STANTON, editors, *Artificial Intelligence Developments and Applications: Selected papers from the first Australian Joint Artificial Intelligence Conference*, pp. 273–289, Elsevier Science Publishers, North-Holland, 1987. 40

- [Word 08] K. WORDEN, C.R. FARRAR, J. HAYWOOD, ET AL. **A review of nonlinear dynamics applications to structural health monitoring.** *Structural Control and Health Monitoring*, Vol. 15, No. 4, pp. 540–567, 2008. 29
- [Word 09] K. WORDEN AND M. FRISWELL. *Modalvibrationbased damage identification*, Chap. 11, pp. 1–37. John Wiley & Sons, Ltd., 2009. 29, 36
- [Word 11] K. WORDEN, W.J. STASZEWSKI, AND J.J. HENSMAN. **Natural computing for mechanical systems research: A tutorial overview.** *Mechanical Systems and Signal Processing*, Vol. 25, No. 1, pp. 4–111, 2011. 36, 37, 38, 87
- [Wu 06] J.-S. WU AND S.-H. HSU. **A unified approach for the free vibration analysis of an elastically supported immersed uniform beam carrying an eccentric tip mass with rotary inertia.** *Journal of Sound and Vibration*, Vol. 291, No. 3, pp. 1122–1147, 2006. 110
- [Wu 09] Z. S. WU AND A. P. ADEWUYI. **Vibration-based structural health monitoring technique using statistical features for data stability assessment and damage localization.** *Sensors and Smart Structures Technologies for Civil, Mechanical, and Aerospace Systems 2009*, 2009. 21
- [Wu 14] Q. WU, Y. YE, H. ZHANG, ET AL. **ForesTexter: An efficient random forest algorithm for imbalanced text categorization.** *Knowledge-Based Systems*, Vol. 67, pp. 105–116, 2014. 41
- [Xant 07] P. XANTHAKOS. *Theory and Design of Bridges*, pp. i–xix. John Wiley & Sons, Ltd., 2007. 110
- [Xu 16] C. XU, N. ZHOU, J. XIE, ET AL. **Investigation on eddy current pulsed thermography to detect hidden cracks on corroded metal surface.** *{NDT} and E International*, Vol. 84, pp. 27–35, 2016. 28
- [Xuan 14] A. XUAN. **Lecture notes in Structure Mechanics I Ib Labs.** 2014. 20



- [Yam 03] L.H. YAM, Y.J. YAN, AND J.S. JIANG. **Vibration-based damage detection for composite structures using wavelet transform and neural network identification.** *Composite Structures*, Vol. 60, No. 4, pp. 403–412, 2003. 32, 135, 136, 137
- [Yan 04] Y.J. YAN AND L.H. YAM. **Detection of delamination damage in composite plates using energy spectrum of structural dynamic responses decomposed by wavelet analysis.** *Computers and Structures*, Vol. 82, No. 45, pp. 347–358, 2004. 32, 137
- [Yan 07] Y.J. YAN, L. CHENG, Z.Y. WU, ET AL. **Development in vibration-based structural damage detection technique.** *Mechanical Systems and Signal Processing*, Vol. 21, No. 5, pp. 2198–2211, 2007. 30, 32, 87
- [Yang 05] B.-S. YANG, D.-S. LIM, AND A.C.C. TAN. **VIBEX: an expert system for vibration fault diagnosis of rotating machinery using decision tree and decision table.** *Expert Systems with Applications*, Vol. 28, No. 4, pp. 735–742, 2005. 42
- [Yang 09] Z. YANG, L. WANG, H. WANG, ET AL. **Damage detection in composite structures using vibration response under stochastic excitation.** *Journal of Sound and Vibration*, Vol. 325, No. 45, pp. 755–768, 2009. 135, 136
- [Yang 14] Z. YANG, X. CHEN, X. LI, ET AL. **Wave motion analysis in arch structures via wavelet finite element method.** *Journal of Sound and Vibration*, Vol. 333, No. 2, pp. 446–469, 2014. 62
- [Zhan 11] X. ZHANG, X. CHEN, Z. HE, ET AL. **The analysis of shallow shells based on multivariable wavelet finite element method.** *Acta Mechanica Solida Sinica*, Vol. 24, No. 5, pp. 450–460, 2011. 62
- [Zhen 09] S. ZHENG, Z. LI, AND H. WANG. **Research on delamination monitoring for composite structures based on HHGAWNN.** *Applied Soft Computing*, Vol. 9, No. 3, pp. 918–923, 2009. 32, 137
- [Zhou 00] D. ZHOU AND Y.K. CHEUNG. **The free vibration of a type of tapered beams.** *Computer Methods in Applied Mechanics and Engineering*, Vol. 188, No. 13, pp. 203–216, 2000. 74

- [Zhou 14] Q. ZHOU, H. ZHOU, Q. ZHOU, ET AL. **Structure damage detection based on random forest recursive feature elimination.** *Mechanical Systems and Signal Processing*, Vol. 46, pp. 82–90, 2014. 42
- [Zhu 06] X.Q. ZHU AND S.S. LAW. **Wavelet-based crack identification of bridge beam from operational deflection time history.** *International Journal of Solids and Structures*, Vol. 43, No. 78, pp. 2299–2317, 2006. 32, 137
- [Zou 00] Y. ZOU, L. TONG, AND G.P. STEVEN. **Vibration-based model-dependent damage (delamination) identification and health monitoring for composite structures - a review.** *Journal of Sound and Vibration*, Vol. 230, No. 2, pp. 357–378, 2000. 29, 30, 137

# Appendix A

**Table A1:** First 25 patterns used for predicting the depth and location of the crack in the free vibrating Euler-Bernoulli cantilever ( $k_n$  is a frequency parameter).

location	depth	$k_1$	$k_2$	$k_3$	$k_4$	$k_5$	$k_6$	$k_7$	$k_8$
0.001	0.44	1.4367	4.1245	7.2044	10.3140	13.4386	16.5703	19.7059	22.8439
0.005	0.39	1.5102	4.1869	7.2685	10.3826	13.5146	16.6551	19.8006	22.9490
0.005	0.39	1.5102	4.1869	7.2685	10.3826	13.5146	16.6551	19.8006	22.9490
0.008	0.35	1.5666	4.2411	7.3241	10.4405	13.5768	16.7231	19.8750	23.0304
0.01	0.43	1.4573	4.1662	7.2725	10.4091	13.5610	16.7201	19.8830	23.0482
0.012	0.17	1.7805	4.5090	7.6033	10.7075	13.8305	16.9655	20.1087	23.2578
0.012	0.27	1.6710	4.3565	7.4408	10.5548	13.6915	16.8404	19.9966	23.1574
0.016	0.5	1.3591	4.1332	7.2740	10.4393	13.6158	16.7969	19.9802	23.1643
0.017	0.07	1.8562	4.6535	7.7961	10.9252	14.0601	17.1992	20.3415	23.4865
0.019	0.34	1.5862	4.2887	7.4036	10.5518	13.7195	16.8963	20.0777	23.2613
0.02	0.22	1.7317	4.4485	7.5538	10.6823	13.8326	16.9950	20.1644	23.3377
0.021	0.47	1.4073	4.1739	7.3238	10.5002	13.6887	16.8819	20.0766	23.2712
0.022	0.28	1.6635	4.3708	7.4846	10.6294	13.7956	16.9722	20.1541	23.3382
0.025	0.22	1.7334	4.4596	7.5772	10.7182	13.8804	17.0535	20.2321	23.4127
0.025	0.43	1.4676	4.2207	7.3738	10.5558	13.7513	16.9515	20.1527	23.3525
0.026	0.23	1.7229	4.4480	7.5682	10.7135	13.8800	17.0569	20.2387	23.4217
0.03	0.27	1.6790	4.4053	7.5395	10.7030	13.8863	17.0776	20.2707	23.4616
0.031	0.38	1.5405	4.2868	7.4460	10.6358	13.8400	17.0480	20.2546	23.4560
0.032	0.31	1.6317	4.3631	7.5096	10.6872	13.8823	17.0832	20.2835	23.4788
0.033	0.29	1.6566	4.3892	7.5345	10.7099	13.9034	17.1026	20.3010	23.4937
0.038	0.45	1.4484	4.2520	7.4487	10.6693	13.8971	17.1217	20.3362	23.5333
0.042	0.49	1.3933	4.2388	7.4566	10.6935	13.9326	17.1630	20.3756	23.5581
0.043	0.04	1.8690	4.6833	7.8423	10.9845	14.1292	17.2743	20.4188	23.5619
0.043	0.09	1.8470	4.6463	7.8010	10.9488	14.1038	17.2603	20.4141	23.5617

All MatLab pieces of code and datasets can be found at <https://owncloud.ut.ee/owncloud/index.php/s/pycY9epDTLyZ4tR>

# Appendix B

**Table B1:** A summary table of parameter quantifications.

			NFP		HWTC		NFP+HWTC	
			ANN	RF	ANN	RF	ANN	RF
1 crack	L	MSE	1.6e-3*	2.0e-3	7e-6*	8e-6	2e-7 <sup>H</sup>	8e-6 <sup>H</sup>
		R	9.908e-1*	9.896e-1	9.996e-1*	9.999e-1	1.00	9.999e-1
	D	MSE	9e-4*	8e-4	4.6e-3*	6.1e-3	5e-4 <sup>F</sup>	8e-4 <sup>F</sup>
		R	9.772e-1*	9.841e-1	8.871e-1*	8.491e-1	9.868e-1	9.841e-1
		Ref.	Fig. 5.10a, 5.11, 5.12	Tab. 5.5	Fig. 5.10b, 5.11, 5.12	Tab. 5.6	Fig. 5.13	Fig. 5.14
2 cracks	L1	MSE					2.1e-3 <sup>H</sup>	2e-5 <sup>H</sup>
		R					9.553e-1	9.997e-1
	L2	MSE					1.9e-3 <sup>H</sup>	2e-5 <sup>H</sup>
		R					9.677e-1	9.997e-1
	D1	MSE					1.1e-3 <sup>F</sup>	6e-6 <sup>F</sup>
R						9.515e-1	9.998e-1	
D2	MSE					1.0e-3 <sup>F</sup>	5e-6 <sup>F</sup>	
	R					9.586e-1	9.998e-1	
		Ref.				Fig. 5.17	Fig. 5.18	
elastic supports	$k_t$	MSE	5e-8	5e-6	1e-4	2e-4	5e-7**	1e-5**
		R	1.00	9.999e-1	9.990e-1	9.984e-1	1.00	9.999e-1
	$k_r$	MSE	1.1e-3	1.5e-3	8.24e-2	1.54e-2	8.4e-3**	3.2e-3**
		R	9.934e-1	9.912e-1	4.00e-2	9.123e-1	9.482e-1	9.817e-1
		Ref.	Tab. 6.2, 6.3	Tab. 6.4	Tab. 6.2, 6.3	Tab. 6.2, 6.3	Tab. 6.4	
point mass	L	MSE	2e-5	2e-4	3e-7	6e-6	2e-7 <sup>H</sup>	6e-6 <sup>H</sup>
		R	9.997e-1	9.982e-1	1.00	9.999e-1	1.00	9.998e-1
	M	MSE	2.1e-3	3.9e-3	6.56e-2	8.76e-2	1.6e-3 <sup>F</sup>	3.7e-3 <sup>F</sup>
		R	9.581e-1	9.797e-1	4.902e-1	3.888e-1	9.617e-1	9.781e-1
		Ref.	Tab. 7.5, 7.4	Tab. 7.6	Tab. 7.5, 7.4	Tab. 7.6	Fig. 7.4	Fig. 7.5
delamination	L1	MSE	5.9e-3	9e-4	3.4e-3	7e-4	9e-4**	4e-4**
		R	9.685e-1	9.948e-1	9.808e-1	9.959e-1	9.945e-1	9.974e-1
	L2	MSE	3.2e-3	1.9e-3	6.8e-3	3.4e-3	2.4e-3**	1.2e-3**
		R	9.729e-1	9.848e-1	9.440e-1	9.715e-1	9.816e-1	9.903e-1
H	MSE	8.02e-2	7.35e-2	1.131e-1	9.45e-2	7.83e-2 <sup>F</sup>	7.34e-2 <sup>F</sup>	
	R	6.889e-1	7.183e-1	5.191e-1	6.145e-1	6.917e-1	7.198e-1	
		Ref.	Tab. 8.2	Tab. 8.3	Tab. 8.2	Tab. 8.3	Fig. 8.3	Fig. 8.4

\* the result is obtained by the ANN with two output neurons

\*\* the result is obtained combining NFPs and HWTCs

<sup>F</sup> the result is obtained using NFP based dataset

<sup>H</sup> the result is obtained using HWTC based dataset

# Acknowledgements

I wish to express my deepest gratitude to Associate Professor Helle Hein for supervising me throughout my postgraduate and doctoral studies. Her wide knowledge in structural dynamics, detailed and constructive comments are valuable to me. Within the last decade, Helle Hein has always been providing me with guidance, inspiration, emotional encouragement, and support both in the academic and everyday life. Without her enormous patience and valuable pieces of advice, this thesis would not have been completed. Working under Helle's supervision has been a rewarding experience, which I will carry with me throughout my life.

Finally, I wish to sincerely thank my family, colleagues and friends for their support and understanding throughout my long-standing studies.

The degree study has been regularly financially funded by Tiigri Ülikool and the Estonian Science Foundation under Grant ETF 8830 and IUT34-4. They provided a number of opportunities to attend international conferences, which benefit me both in the research and communication with worldwide colleagues.

## Kokkuvõte (Summary in Estonian)

### Haari lainikute meetod omavõnkumiste analüüsiks ja parameetrite määramiseks

Tala on konstruktsioonelement, mille ülesandeks on vastu pidada erinevatele koormustele. Projekteerimisel alahinnatud koormused, ebatäpsused tootmisel, söövitav keskkond, konstruktsiooni vananemine eksploatatsiooni käigus võivad talasid kahjustada ning põhjustada kogu konstruktsiooni purunemist. Seetõttu talade dünaamilise käitumise modelleerimine ja eksploatatsiooni jälgimine on jätkuvalt aktuaalne teema konstruktsioonide mehaanikas.

Konstruktsioonelementides toimunud muutuste (näiteks pragude või delaminatsiooni) kindlakstegemisel kasutatavad eksperimentaalsed meetodid (röntgen, ultraheli, magnetväli, termoväli, akustika ja teised meetodid) võimaldavad fikseerida toimunud muutused, kuid need meetodid on kallid ja ressursimahukad. Viimasel ajal on pälvunud teadlaste tähelepanu modaalsed meetodid. Sellised meetodid põhinevad asjaolul, et konstruktsiooni mistahes purunemine muudab füüsikalisi omadusi (massi, jäikust, võnkeenergia hajumist), mis omakorda muudavad modaalseid omadusi, näiteks vabavõnkumise sagedusi (*natural frequencies*) ja moode (*mode shapes*).

Käesolevas väitekirjas käsitletakse Euler-Bernoulli tüüpi talasid, kuna see on enim kasutatav teooria õhukeste talade kohta. Töö annab uue vaatenurga vabavõnkumise sageduste ja purunemise parameetrite määramise kohta. Töös pakutakse välja Haari lainikute meetod sageduste arvutamiseks ja andmete töötlemiseks. Haari lainikud on matemaatiliselt lihtsaimad lainikud. Haari lainikuid on võimalik kasutada funktsioonide approksimeerimisel.

Haari lainikuid on edukalt kasutatud diferentsiaalvõrrandite lahendamiseks. Käesolevas töös Peatükis 4 on Haari lainikuid ja nende integreerimist rakendatud vabavõnkumise ülesannete korral, kus lahendatavaks võrrandiks on muutuvate koordinaatidega diferentsiaalvõrrand, millel puudub analüütiline lahend (näiteks ebaühtlase ristlõikega tala, materjali funktsionaalse gradientjaotusega tala). Mitmed arvutused on kinnitanud, et pakutud lähenemisviis on kiire ja täpne tala vabavõnkumiste sageduste arvutamisel.

Väitekirja Peatükid 5-8 käsitlevad vabavõnkumisega seotud pöördülesandeid: pragude, delaminatsioonide, massipunktide, elastsete tugede jäikuse parameetrite määramist modaalsete omaduste kaudu. Kuna purunemise asukoha ja ulatuse arvutamine võnkumise diferentsiaalvõrrandist ei ole analüütiliselt võimalik, peab lahendusi otsima arvutuslike meetodite abil, näiteks masinõppe abil. Antud töös

kasutatakse tehisnärvivõrke (*Artificial Neural Networks*) ja juhumetsi (*Random Forest*). Tehisnärvivõrgud on laialt levinud masinõppe meetod, mille peamiseks eeliseks teiste meetodite ees on võime olemasolevate näidete põhjal õppida. Vabavõnkumisega seotud ülesannete lahendamiseks pole tarvis enam ise kõiki parameetreid arvutada, vaid piisab, kui on olemas teatud hulk näiteid oodatavate parameetrite kohta, ning nende näidete abil treenitud tehisnärvivõrk on suuteline ülejäänud tulemusi ise identifitseerima. Tehisnärvivõrkude suureks puuduseks on suur hulk võrgu ja treenimisalgoritmi parameetreid. Alternatiivina tehisnärvivõrkudele vaadeldakse juhumetsi, mis on samuti tuntud masinõppe meetod, kuid parameetreid on vähem.

Andmekogumite genereerimiseks lahendati võnkumisevõrrand, ning tulemusi töödeldud Haari lainikute abil. Eesmärgiks on olnud vaatluse all olevate tala mudelite korral hinnata ning võrrelda tehisnärvivõrkude ja juhumetsade abil identifitseeritud purunemise parameetreid. Arvutuslikud mudelid näitasid, et:

- Haari lainikute abil genereeritud andmekogumite arvutamiseks kuluv aeg oli üle kümne korra väiksem kui vabavõnkumiste sagedustele põhinevate andmekogumite arvutusaeg;
- Haari lainikute koefitsiendid olid tundlikumad purunemise asukoha parameetrite suhtes, samas vabavõnkumiste sageduste parameetrid olid tundlikumad purunemise ulatuse suhtes (Lisa B Tabel B1);
- enamikel juhtudel andis tehisnärvivõrk sama täpseid ennustusi kui juhumetsad; erandiks oli jääkuse parameetrite määramine elastsetes tuges: tehisnärvivõrgud tegid oluliselt täpsemaid ennustusi kui juhumetsad (Lisa B Tabel B1).

Käesolevas väitekirjas pakutud meetodeid saab kasutada teistes teoreetilistes ülesannetes vabavõnkumiste ja purunemiste uurimiseks või rakendada talade purunemise diagnostikas. Näiteks arhitektid ja praktikud saavad kirjeldatud lähenemisviisi kasutada projekteeritavate struktuurielementide käitumise simulatsioonides. Pakutud ennustusmudeleid on võimalik tulevikus integreerida konstruktsioonide diagnostika riistvarasse, mis põhineb vabavõnkumiste sagedustele või moodidele.

# Curriculum vitae

## General

Name: Ljubov Jaanuska  
(till 8.01.2016 Ljubov Feklistova)  
Date of Birth: 25.06.1985  
Citizenship: Estonian

## Education

2020 University of Tartu, Faculty of Mathematics and Computer Science,  
doctoral studies, speciality: computer science (external)  
2009 – 2015 University of Tartu, Faculty of Mathematics and Computer Science,  
doctoral studies, speciality: computer science  
2006 – 2009 University of Tartu, Faculty of Science and Technology, master stud-  
ies, speciality: information technology  
2006 – 2009 University of Tartu, Faculty of Mathematics and Computer Science,  
master studies, speciality: teacher of computer studies  
2006 – 2009 Coventry University, Faculty of Engineering, Environment and  
Computing, bachelor studies, speciality: information technology  
and management  
2003 – 2006 University of Tartu, Faculty of Science and Technology, bachelor  
studies, speciality: information technology  
1991 – 2003 Tartu Annelinna secondary school

## Work experience

2011 – ... University of Tartu, Faculty of Mathematics and Computer Science,  
assistant  
2009 – 2012 Tartu Annelinna secondary school, teacher



# Elulookirjeldus

## Üldandmed

Nimi:	Ljubov Jaanuska (kuni 8.01.2016 Ljubov Feklistova)
Sünniaeg:	25.06.1985
Kodakondsus:	Eesti

## Haridus

2020	Tartu Ülikool, matemaatika-informaatikateaduskond, doktoriõpe, eriala: informaatika (ekstern)
2009 – 2015	Tartu Ülikool, matemaatika-informaatikateaduskond, doktoriõpe, eriala: informaatika
2006 – 2009	Tartu Ülikool, loodus- ja tehnoloogiateaduskond, magistriõpe, eriala: infotehnoloogia
2006 – 2009	Tartu Ülikool, matemaatika-informaatikateaduskond, magistriõpe, eriala: informaatika õpetaja
2007 – 2008	Coventry Ülikool, bakalaureuseõpe, eriala: infotehnoloogia ja juhtimine
2003 – 2006	Tartu Ülikool, bakalaureuseõpe, eriala: infotehnoloogia
1991 – 2003	Tartu Annelinna gümnaasium

## Teenistuskäik

2011 – ...	Tartu Ülikool, matemaatika-informaatikateaduskond, informaatika assistent
2009 – 2012	Tartu Annelinna gümnaasium, õpetaja

# List of original publications

The publications included in the thesis describe author's contribution to the free vibration analysis of beams with the aid of the Haar wavelets and machine learning.

- 1 H. Hein and L. Feklistova. **Identification of mass location on vibrating beams using Haar wavelets and neural networks.** In: *Proceedings of 22nd Nordic Seminar of Computational Mechanics*, pp. 105-108, 2009.
- 2 L. Feklistova. **Free vibrations of beams with non-uniform cross-sections and elastic end constraints using Haar wavelet method.** In: *Proceedings of NSCM-23*, pp. 185-188, 2010.
- 3 H. Hein and L. Feklistova. **Computationally efficient delamination in composite beams using Haar wavelets.** *Mechanical Systems and Signal Processing*, 25(6), pp. 2257–2270, 2011.
- 4 H. Hein and L. Feklistova. **Free vibrations of non-uniform and axially functionally graded beams using Haar wavelets.** *Engineering structures*, 33(12), pp. 3696–3701, 2011.
- 5 L. Feklistova and H. Hein. **Delamination identification using machine learning methods and Haar wavelets.** *Computer Assisted Methods in Engineering and Science*, 19(4), pp. 351–360, 2012.
- 6 L. Feklistova and H. Hein. **Crack localization in Euler–Bernoulli beams.** In: *Proceedings of the 2nd International Conference Optimization and Analysis of Structures*, pp. 35–38, 2013.
- 7 L. Feklistova and H. Hein. **Parameter identification of vibrating beams with elastic boundary conditions.** In: *Proceedings of the 26th Nordic Seminar on Computational Mechanics*, pp. 54–57, 2013.

- 8 L. Feklistova and H. Hein. **Parameter identification for supports and cracks in beams with non-classical boundary conditions.** In: *Construction Materials and Structures: International Conference on Construction Materials and Structures*, pp. 1295–1302, 2014.
- 9 L. Jaanuska and H. Hein. **Crack identification in beams using Haar wavelets and machine learning methods.** *International Journal of Mechanics*, 10, pp. 281-287, 2016.
- 10 H. Hein and L. Jaanuska. **Comparison of machine learning methods for crack localization.** *Acta et Commentationes Universitatis Tartuensis de Mathematica*, 23, pp. 125–142, 2019.

**DISSERTATIONES INFORMATICAЕ  
PREVIOUSLY PUBLISHED IN  
DISSERTATIONES MATHEMATICAE  
UNIVERSITATIS TARTUENSIS**

19. **Helger Lipmaa.** Secure and efficient time-stamping systems. Tartu, 1999, 56 p.
22. **Kaili Müürisep.** Eesti keele arvutigrammatika: süntaks. Tartu, 2000, 107 lk.
23. **Varmo Vene.** Categorical programming with inductive and coinductive types. Tartu, 2000, 116 p.
24. **Olga Sokratova.**  $\Omega$ -rings, their flat and projective acts with some applications. Tartu, 2000, 120 p.
27. **Tiina Puolakainen.** Eesti keele arvutigrammatika: morfoloogiline ühestamine. Tartu, 2001, 138 lk.
29. **Jan Villemson.** Size-efficient interval time stamps. Tartu, 2002, 82 p.
45. **Kristo Heero.** Path planning and learning strategies for mobile robots in dynamic partially unknown environments. Tartu 2006, 123 p.
49. **Härmel Nestra.** Iteratively defined transfinite trace semantics and program slicing with respect to them. Tartu 2006, 116 p.
53. **Marina Issakova.** Solving of linear equations, linear inequalities and systems of linear equations in interactive learning environment. Tartu 2007, 170 p.
55. **Kaarel Kaljurand.** Attempto controlled English as a Semantic Web language. Tartu 2007, 162 p.
56. **Mart Anton.** Mechanical modeling of IPMC actuators at large deformations. Tartu 2008, 123 p.
59. **Reimo Palm.** Numerical Comparison of Regularization Algorithms for Solving Ill-Posed Problems. Tartu 2010, 105 p.
61. **Jüri Reimand.** Functional analysis of gene lists, networks and regulatory systems. Tartu 2010, 153 p.
62. **Ahti Peder.** Superpositional Graphs and Finding the Description of Structure by Counting Method. Tartu 2010, 87 p.
64. **Vesal Vojdani.** Static Data Race Analysis of Heap-Manipulating C Programs. Tartu 2010, 137 p.
66. **Mark Fišel.** Optimizing Statistical Machine Translation via Input Modification. Tartu 2011, 104 p.
67. **Margus Nii-soo.** Black-box Oracle Separation Techniques with Applications in Time-stamping. Tartu 2011, 174 p.
71. **Siim Karus.** Maintainability of XML Transformations. Tartu 2011, 142 p.
72. **Margus Treumuth.** A Framework for Asynchronous Dialogue Systems: Concepts, Issues and Design Aspects. Tartu 2011, 95 p.
73. **Dmitri Lepp.** Solving simplification problems in the domain of exponents, monomials and polynomials in interactive learning environment T-algebra. Tartu 2011, 202 p.

74. **Meelis Kull.** Statistical enrichment analysis in algorithms for studying gene regulation. Tartu 2011, 151 p.
77. **Bingsheng Zhang.** Efficient cryptographic protocols for secure and private remote databases. Tartu 2011, 206 p.
78. **Reina Uba.** Merging business process models. Tartu 2011, 166 p.
79. **Uuno Puus.** Structural performance as a success factor in software development projects – Estonian experience. Tartu 2012, 106 p.
81. **Georg Singer.** Web search engines and complex information needs. Tartu 2012, 218 p.
83. **Dan Bogdanov.** Sharemind: programmable secure computations with practical applications. Tartu 2013, 191 p.
84. **Jevgeni Kabanov.** Towards a more productive Java EE ecosystem. Tartu 2013, 151 p.
87. **Margus Freudenthal.** Simpl: A toolkit for Domain-Specific Language development in enterprise information systems. Tartu, 2013, 151 p.
90. **Raivo Kolde.** Methods for re-using public gene expression data. Tartu, 2014, 121 p.
91. **Vladimir Sor.** Statistical Approach for Memory Leak Detection in Java Applications. Tartu, 2014, 155 p.
92. **Naved Ahmed.** Deriving Security Requirements from Business Process Models. Tartu, 2014, 171 p.
94. **Liina Kamm.** Privacy-preserving statistical analysis using secure multi-party computation. Tartu, 2015, 201 p.
100. **Abel Armas Cervantes.** Diagnosing Behavioral Differences between Business Process Models. Tartu, 2015, 193 p.
101. **Fredrik Milani.** On Sub-Processes, Process Variation and their Interplay: An Integrated Divide-and-Conquer Method for Modeling Business Processes with Variation. Tartu, 2015, 164 p.
102. **Huber Raul Flores Macario.** Service-Oriented and Evidence-aware Mobile Cloud Computing. Tartu, 2015, 163 p.
103. **Tauno Metsalu.** Statistical analysis of multivariate data in bioinformatics. Tartu, 2016, 197 p.
104. **Riivo Talviste.** Applying Secure Multi-party Computation in Practice. Tartu, 2016, 144 p.
108. **Siim Orasmaa.** Explorations of the Problem of Broad-coverage and General Domain Event Analysis: The Estonian Experience. Tartu, 2016, 186 p.
109. **Prastudy Mungkas Fauzi.** Efficient Non-interactive Zero-knowledge Protocols in the CRS Model. Tartu, 2017, 193 p.
110. **Pelle Jakovits.** Adapting Scientific Computing Algorithms to Distributed Computing Frameworks. Tartu, 2017, 168 p.
111. **Anna Leontjeva.** Using Generative Models to Combine Static and Sequential Features for Classification. Tartu, 2017, 167 p.
112. **Mozhgan Pourmoradnasseri.** Some Problems Related to Extensions of Polytopes. Tartu, 2017, 168 p.

113. **Jaak Randmets.** Programming Languages for Secure Multi-party Computation Application Development. Tartu, 2017, 172 p.
114. **Alisa Pankova.** Efficient Multiparty Computation Secure against Covert and Active Adversaries. Tartu, 2017, 316 p.
116. **Toomas Saarsen.** On the Structure and Use of Process Models and Their Interplay. Tartu, 2017, 123 p.
121. **Kristjan Korjus.** Analyzing EEG Data and Improving Data Partitioning for Machine Learning Algorithms. Tartu, 2017, 106 p.
122. **Eno Tõnisson.** Differences between Expected Answers and the Answers Offered by Computer Algebra Systems to School Mathematics Equations. Tartu, 2017, 195 p.

## DISSERTATIONES INFORMATICAЕ UNIVERSITATIS TARTUENSIS

1. **Abdullah Makkeh.** Applications of Optimization in Some Complex Systems. Tartu 2018, 179 p.
2. **Riivo Kikas.** Analysis of Issue and Dependency Management in Open-Source Software Projects. Tartu 2018, 115 p.
3. **Ehsan Ebrahimi.** Post-Quantum Security in the Presence of Superposition Queries. Tartu 2018, 200 p.
4. **Ilya Verenich.** Explainable Predictive Monitoring of Temporal Measures of Business Processes. Tartu 2019, 151 p.
5. **Yauhen Yakimenka.** Failure Structures of Message-Passing Algorithms in Erasure Decoding and Compressed Sensing. Tartu 2019, 134 p.
6. **Irene Teinmaa.** Predictive and Prescriptive Monitoring of Business Process Outcomes. Tartu 2019, 196 p.
7. **Mohan Liyanage.** A Framework for Mobile Web of Things. Tartu 2019, 131 p.
8. **Toomas Krips.** Improving performance of secure real-number operations. Tartu 2019, 146 p.
9. **Vijayachitra Modhukur.** Profiling of DNA methylation patterns as biomarkers of human disease. Tartu 2019, 134 p.
10. **Elena Sügis.** Integration Methods for Heterogeneous Biological Data. Tartu 2019, 250 p.
11. **Tõnis Tasa.** Bioinformatics Approaches in Personalised Pharmacotherapy. Tartu 2019, 150 p.
12. **Sulev Reisberg.** Developing Computational Solutions for Personalized Medicine. Tartu 2019, 126 p.
13. **Huishi Yin.** Using a Kano-like Model to Facilitate Open Innovation in Requirements Engineering. Tartu 2019, 129 p.
14. **Faiz Ali Shah.** Extracting Information from App Reviews to Facilitate Software Development Activities. Tartu 2020, 149 p.
15. **Adriano Augusto.** Accurate and Efficient Discovery of Process Models from Event Logs. Tartu 2020, 194 p.
16. **Karim Baghery.** Reducing Trust and Improving Security in zk-SNARKs and Commitments. Tartu 2020, 245 p.
17. **Behzad Abdolmaleki.** On Succinct Non-Interactive Zero-Knowledge Protocols Under Weaker Trust Assumptions. Tartu 2020, 209 p.
18. **Janno Siim.** Non-Interactive Shuffle Arguments. Tartu 2020, 154 p.
19. **Ilya Kuzovkin.** Understanding Information Processing in Human Brain by Interpreting Machine Learning Models. Tartu 2020, 149 p.
20. **Orlenys López Pintado.** Collaborative Business Process Execution on the Blockchain: The Caterpillar System. Tartu 2020, 170 p.
21. **Ardi Tampuu.** Neural Networks for Analyzing Biological Data. Tartu 2020, 152 p.

22. **Madis Vasser.** Testing a Computational Theory of Brain Functioning with Virtual Reality. Tartu 2020, 106 p.